# 16QAM FOR NEXT-GENERATION OPTICAL TRANSPORT NETWORKS

A Dissertation
Presented to
The Academic Faculty

by

Andrew Joseph Stark

In Partial Fulfillment
of the Requirements for the Degree
Doctor of Philosophy in the
School of Electrical and Computer Engineering

Georgia Institute of Technology
May 2013

# 16QAM FOR NEXT-GENERATION OPTICAL TRANSPORT NETWORKS

Approved by:


Dr. Stephen E. Ralph, Advisor
School of Electrical and Computer Engineering
*Georgia Institute of Technology*

Dr. Sorin Tibuleac
School of Electrical and Computer Engineering
*Georgia Institute of Technology*

Dr. Gee-Kung Chang
School of Electrical and Computer Engineering
*Georgia Institute of Technology*

Dr. Michael Chapman
School of Physics
*Georgia Institute of Technology*

Dr. Robert Lingle, Jr.
School of Electrical and Computer Engineering
*Georgia Institute of Technology*


Date Approved: 13 Dec. 2012

For my wife, first and always.

# ACKNOWLEDGEMENTS

Many thanks go out to a great number of people, without whom this work would not have been possible. The first thanks go to my wife Rachel – she makes what I do both possible and worth the sweat.

A most emphatic thanks go to Dr. Thomas Detwiler in whom I have begun a life-long friendship during our PhD work together. He has taught, guided, and kept me focused on what I was here to do.

Next, I wish to thank all of my fellow graduate students: Yu-Ting Hsueh, Cheng Liu, Jie Pan, Yoni Gabby, Steven Searcy, Patrick Caputo, Patrick Decker, Pierre Isautier, Kevin Anzalone, Clark Kerr, Sriharsha Kota, Kedar Mehta, and Ben Clarke. A PhD degree is awarded to a single person, but I would never have accomplished so much without their collaboration.

Thanks to Sorin Tibuleac, Bert Basch, Mark Filer, Robert Lingle, Alan McCurdy, Janis Valdmanis and all the members of the Georgia Tech Terabit Optical Consortium for their support while I worked as a graduate research assistant – their suggestions and expertise supplied the framework and direction for my work.

I also thank Professors Gee-Kung Chang, Robert Lingle Jr. for serving on my reading committee and Professors Sorin Tibuleac and Michael Chapman for hearing my defense to ensure the quality of this Doctoral Dissertation.

Finally I wish to thank Professor Stephen Ralph for his patience, guidance, and willingness to work with me over the last four-and-a-half years.

# TABLE OF CONTENTS

# LIST OF TABLES

# LIST OF FIGURES

Page

# LIST OF ABBREVIATIONS

| | |
|---|---|
| DSP | Digital Signal Processing |
| SE | Spectral Efficiency |
| OSNR | Optical Signal-to-Noise Ratio |
| EDFA | Erbium-Doped Fiber Amplifier |
| WDM | Wavelength-Division Multiplexing |
| CD | Chromatic Dispersion |
| LO | Local Oscillator |
| OFDM | Orthogonal Frequency-Division Multiplexing |
| SSMF | Standard Single-Mode Fiber |
| SDM | Space-Division Multiplexing |
| MIMO | Multiple-In, Multiple-Out |
| NLS | Nonlinear Schrodinger Equation |
| SVA | Slowly-Varying Envelope Approximation |
| FWM | Four-Wave Mixing |
| SPM | Self-Phase Modulation |
| XPM | Cross-Phase Modulation |
| DFB | Distributed Feedback |
| EC | External Cavity |
| MZI | Mach-Zehnder Inferometer |
| MZM | Mach-Zehnder Modulator |
| ROADM | Reconfigurable Optical Add/Drop Multiplexor |
| LCOS | Liquid-Crystal on Silicon |

| | |
|---|---|
| DLP | Digital Light Processor |
| AWG | Arrayed Waveguide |
| ASE | Amplified Spontaneous Emission |
| SNR | Signal-to-Noise Ratio |
| OOK | On-Off Keying |
| DPSK | Differential Phase-Shift Keying |
| DQPSK | Differential Quadrature Phase-Shift Keying |
| TIA | Transimpedance Amplifier |
| WAN | Wide-Area Network |
| PDM | Polarization-Division Multiplexing |
| FEC | Forward Error Correction |
| BER | Bit-Error Rate |
| QPSK | Quadrature Phase Shift Keying |
| RZ | Return-to-Zero |
| BPSK | Binary Phase Shift Keying |
| OIF | Optical Internetworking Forum |
| NRZ | Non Return-to-Zero |
| QAM | Quadrature Amplitude Modulation |
| LMS | Least-Mean Square |
| IFFT | Inverse Fast Fourier Transform |
| CMA | Constant Modulus Algorithm |
| ISI | Inter-Symbol Interference |
| NDA | Non Data-Aided |
| MMSE | Minimum Mean-Square Error |
| ICA | Independent Component Analysis |

| | |
|---|---|
| PMD | Polarization Mode Dispersion |
| BPF | Bandpass Filter |
| OLD | Optical Line Driver |
| DCM | Dispersion Compensating Module |
| RDPS | Residual Dispersion Per Span |
| VOA | Variable Optical Attenuators |
| TFBG | Tunable Fiber Bragg Gratings |
| OQPSK | Offset Quadrature Phase Shift Keying |
| NZDSF | Non-Zero Dispersion-Shifted Fiber |
| NLT | Nonlinear Threshold |
| DCF | Dispersion-Compensating Fiber |
| XPolM | Cross-Polarization Modulation |
| WSS | Wavelength-Selective Switch |
| DMD | Digital Micromirror Device |
| PG | Parametric Gain |
| NLPN | Nonlinear Phase Noise |
| NLAN | Nonlinear Amplitude Noise |
| GEF | Gain Equalizing Filter |
| GN | Gaussian Noise |
| LAF | Large Area Fiber |
| ICI | Inter-Channel Interference |
| OSA | Optical Spectrum Analyzer |
| NLI | Nonlinear Interference |

# SUMMARY

Fiber-optic networks are continually evolving to accommodate ever-increasing data transport rates demanded by modern applications, devices, and services. Network operators are now beginning to deploy systems with 100 Gb/s per-wavelength data rates while maintaining the 50 GHz dense wavelength division multiplexing (DWDM) grid that is (generally) standard for 10 Gb/s systems. Advanced modulation formats incorporating both amplitude- and phase-based data symbols (QAM, etc) are necessary to meet the spectral efficiency (SE) requirements of fiber-optic data transport. These modulation formats require coherent detection, which are in turn enabling future networks to take advantage of advances in silicon CMOS via digital signal processing (DSP) algorithms and techniques.

The primary challenge for current and future networks is the fiber nonlinear response; changes in the intensity of the propagating optical signal induce changes in the optical fiber refractive index. Limiting the allowed propagation intensity will reduce these nonlinear effects and correspondingly limit the total available signal-to-noise ratio (SNR) within the channel. Predicting the nonlinear SNR limits of fiber-optic transport for data rates 100 Gb/s and beyond is a primary purpose of this research.

The first portion of this dissertation identifies, analyzes, and determines strategies for *avoiding* these nonlinear effects with 100 Gb/s and faster per-wavelength data rates over a range of system deployment situations. The experiments reported herein optimize dispersion maps (§4.1), explore alternatives to the de-facto standard of quadrature phase-shift keying (QPSK) (§4.2), craft engineering rules for “hybrid” 100 Gb/s deployments

based on the Nonlinear Threshold (§5), determine and then predict crosstalk-enhanced nonlinear penalties (§6), and identify some optimum filtering and spacing strategies for nonlinear 100 Gb/s transport (§7).

Next, this dissertation expressly matches several novel expressions for nonlinear interference accumulation to experimental data and demonstrates robust theoretical prediction of nonlinear transmission penalties. The experiments were performed to isolate the transmission performance of the fiber medium in the highly dispersive regime – no dispersion compensation or Raman amplification was employed and all other hardware was kept static. These results, detailed in §8, are the first experimental validation of the nonlinear interference expressions on a fiber-type basis.

Lastly, in §9 this dissertation moves to data transport beyond per-wavelength rates of 100 Gb/s by employing 16QAM at baud rates as high as 32 GHz. This section thoroughly examines signal processing strategies for 16QAM transport and extends the nonlinear interference prediction results of §8 to 16QAM. The results reveal that the SNR requirements of 16QAM as limited by nonlinear interference will likely limit deployments to high-density regional and metro networks.

# CHAPTER 1

# INTRODUCTION

Fiber-optic communication systems have begun evolving to incorporate digital signal processing (DSP), coherent detection, and phase-based modulation formats to enable higher spectral efficiency (SE) transmission than intensity modulation (IM) and direct detection (DD) allows. This movement to coherent reception in the network has incorporated other research advancements throughout the ‘90s and ‘00s: signal processing at the transmitter and receiver, refined fiber manufacturing processes, narrow linewidth lasers, tight optical filtering, and forward error correction (FEC). Network operators hope to employ these techniques to meet the ever-increasing data transport demands by scaling existing networks operating at 10 Gb/s and 40 Gb/s to 100 Gb/s and 400 Gb/s and then to 1 Tb/s in the next decade.

Numerous challenges exist to achieve these data rates. Fiber-topic transmission is fundamentally limited by nonlinear refraction, a phenomena whereby the phase of the propagating signal is modulated proportionally to its intensity. This effect limits the total available optical signal-to-noise ratio (OSNR); the launch power (which is the primary method of controlling the OSNR) can only be increased to a certain point, after which the performance of the signal begins to degrade. Prediction of nonlinear refraction effects and their related signal impairments in a variety of network environments is a primary focus of this dissertation.

The Georgia Tech Terabit Consortium – formerly the 100G Consortium – was founded in 2008 by ADVA Optical Networking, OFS, Verizon, and Ciena and hosted at Georgia Tech to investigate solutions and challenges for 100 Gb/s transport. Over the past four-and-a-half years

the consortium has evolved beyond 100G and has begun to addresses the challenges for 400 Gb/s and 1 Tb/s data rates in signal processing, hardware, and simulations. This dissertation encompasses the vast majority of the work with 100 Gb/s systems and the first set of experimental work moving toward 400G transport.

This document is arranged in eight subsequent chapters. Chapter 2 provides a brief historical summary of fiber communication systems and details the fundamental equations that describe electromagnetic propagation in the fiber channel. It also describes optical communication systems in general, highlighting key components of fiber-optic networks.

In Chapter 3 the digital optical coherent receiver is presented and described in detail. This chapter includes both a physical description of the hardware and a thorough explanation of the DSP techniques required to digitally demodulate polarization-division multiplexed (PDM) quadrature phase-shift keying (QPSK) and quadrature amplitude modulation (QAM). Particular attention is given to the choice of the algorithms used for each of the processing steps: (1) chromatic dispersion equalization, (2) polarization demultiplexing, (3) symbol timing recovery, (4) frequency offset estimation, (5) carrier phase recovery, and (6) linear equalization.

Chapter 4 contains the first topic of the experimental work that makes up the vast majority of this dissertation. It comprises two sets of experiments designed to directly address the nonlinear transmission effects (described in Chapter 2) that arise to impair signal performance. The first set of experiments identifies optimum network dispersion map characteristics quadrature phase-shift keying transmission (DQPSK). The second set of experiments examines offset quadrature phase-shift keying (OQPSK) as an alternative modulation format for 100 Gb/s transport.

Chapter 5 addresses the "hybrid" network deployment strategy whereby 100 Gb/s channels replace currently-operating 10 Gb/s channels on a one-by-one basis. In these experiments a large range of potential network environments are examined – from complete inline dispersion compensation to none. The transmission performance of the 100 Gb/s signal is quantified via the Nonlinear Threshold metric to craft engineering rules for future network design.

Chapter 6 contains an experimental investigation and subsequent analysis of in-band crosstalk in ROADM-enabled 100 Gb/s networks. Crosstalk transmission penalties are reported and then scaled with specifically-chosen weighting parameter that enables their accurate prediction over any range of powers and spectral shapes.

Chapter 7 continues the investigation of 100 Gb/s networks with an in-depth experimental exploration of two topics related to grid-agnostic wavelength-division multiplexing (WDM) networks. In the first section the filtering and grid spacing tolerances of QPSK are reported. The second section of Chapter 7 demonstrates the performance of a prototype coherent receiver designed to handle the high photocurrents generated by "colorless" detection.

Chapter 8 is the capstone of the 100 Gb/s network experiments. The 1600 km transmission performance of PDM-QPSK is reported for three distinct fiber types – two commonly used today and one prototype not yet available yet to the wider market. The experiments isolate the fiber performance so that the nonlinear transmission capability of PDM-QPSK can be quantified against a set of theoretical computations of nonlinear interference. The results reveal robust matching between theoretical calculations and the experimentally-determined system margins, enabling system designers to effectively calculate expected transmission margins of potential system deployments. These experiments also establish the new

"Gaussian Noise" (GN) model of uncompensated optical transmission systems whereby the nonlinear interference (NLI) accrues independently from other noise sources (ASE, etc) and is Gaussuan-distributed.

Chapter 9 extends the analysis of Chapter 8 to include PDM-16QAM transmission for the same three fiber types. It also provides a detailed analysis of processing and equalization strategies for PDM-16QAM. Finally, Chapter 9 provides the results of an investigation of the tolerance of 16QAM to filtering effects and the nonlinear effects arising from adjacent channels with different modulation formats.

This dissertation concludes with a summary of all findings and points to new areas of interest prompted by these results. Appendices containing the GaTech-developed demodulation suite are available, but not included with the publication of this document per the request of the GaTech Terabit Consortium. Over the last four years the codebase has become rather extensive and a major intellectual property asset – please contact Prof. Stephen Ralph with further inquiries.

# CHAPTER 2

# FIBER-OPTIC COMMUNICATION SYSTEMS

## 2.1 History of Development

In the last two decades optical fiber has become the primary transport medium for metro, regional, and global telecommunications. As of this writing, commercial fiber-based communications companies have moved beyond the 10 Gb/s and 40 Gb/s per-wavelength data rates that comprised the core of the late '90s and much of the '00s network deployments. Network equipment manufacturers and operators Ciena Corp [1], Verizon [2], Opnext [3], and Ericsson [4] all have field-demonstrated and are actively deploying systems with per-channel transport rates of 100 Gb/s. And the most advanced laboratory systems have demonstrated total capacities beyond hundreds of terabits per second [5-6]. The Internet as the global source of information transfer owes its success to fiber optics. Yet the continued growth of the Internet (and its corresponding growth in bandwidth demand) has driven the push for ever faster fiber optic transport networks.

The success of optical fiber as a high-speed data communication medium can be attributed to a few fundamental reasons. Fiber is principally made of glass. While both abundant and inexpensive, silica enables low-loss propagation of optical frequencies which is not possible in metallic (coaxial) waveguides or wire transmission lines. Optical carrier frequencies (around $10^{14}$ Hz) intrinsically establish the possibility of carrying data bandwidths on that order. Despite

this possibility, data communication via optical fiber originated out of just a few small experiments in 1960s. Early fibers were extremely lossy (~1000 dB/km), but manufacturing process refinements in the early 1970s reduced the loss to 20 dB/km and then to 0.2 dB/km by 1979 [7] in the 1.55 μm wavelength window. By the early eighties, fiber manufacturers had achieved a useful low-loss bandwidth in fiber that spanned from 1300 nm to nearly 1700 nm (~54 THz) [8], which was limited only by fundamental physical mechanisms (e.g. Rayleigh scattering) in the silica material.

The fiber-optic waveguide presents a smaller cross-sectional area (on the order of square microns) to the transverse plane along the direction of propagation compared to traditional coaxial cable. It has therefore been readily practical to upgrade previously-existing communication networks with optical fiber simply by replacing the cables while still using the in-place physical infrastructure (conduits, poles, etc.).

Despite its physical and potential information-carrying advantages, optical fiber did not achieve widespread commercial success until the development of practical amplification techniques. In the eighties, transport links typically carried a few hundred megabits per second and required regenerators at intervals of 40 km or so. The distance between regenerators was largely limited by fiber loss and motivated companies to move to the low-loss 1.55 μm band and therefore achieve larger distances between regenerator huts. However, fiber chromatic dispersion (see §2.2) effects began to limit the increase in transport rates. Dispersion causes the information pulse to "smear" in time with a magnitude proportional to the square of the pulse bandwidth; shorter pulses have more bandwidth and therefore less tolerance to dispersion. Consequently, fiber manufacturers developed dispersion-shifted fibers to eliminate chromatic dispersion at the 1.55 μm band. These dispersion-shifted fibers made their way into the networks of the

telecommunication companies of the time (particularly NTT in Japan and MCI in the United States) and remain in the field today [7].

The paradigm shift for fiber transport occurred in the late eighties and early nineties with the development of the erbium-doped fiber amplifier (EDFA). The EDFA is described in more detail in §2.3, but basically consists of a short length (a few meters) of fiber doped with Erbium atoms. When pumped with a high-power laser of a specific wavelength, the Erbium atoms are excited from their ground state to an energy level that corresponds with the loss-low 1.5 μm band. Thus incoming photons experience gain as they stimulate the excited Erbium atoms [9].

EDFAs enabled fiber network operators to realize the potential of wavelength-division multiplexing (WDM) systems, albeit without coherent detection [10]. WDM is the technique whereby data channels carried by lasers at neighboring wavelengths are multiplexed onto a single optical fiber. The optimum spacing between carriers differs based on the fiber type, transport route, and other factors, but typically ranges from 50 to 200 GHz. A single EDFA is capable of amplifying nearly 100 data channels simultaneously (with 50 GHz spacing). Therefore the combination of EDFA and WDM lengthened the allowable distance between huts while eliminating the need for per-channel regenerators at each hut, which forced down the cost of data transport and increased system capacity. The nineties telecom boom was the deployment of EDFA/WDM data transport technology that facilitated the simultaneous proliferation of Internet-connected computers. System deployments in the mid-to-late nineties achieved capacities above 1 Tb/s over a single fiber [8-9].

Chromatic dispersion (CD) management became a large challenge as a myriad of systems were deployed that operated in the EDFA-amplified 1.5 μm band. Over trans-continental and trans-oceanic distances, a data pulse accumulates tens of thousands of picoseconds of time

spread, rendering the received signal unrecognizable. Network operators began to complement their WDM systems with fiber that exhibited dispersion *opposite* that of the transport fiber so that the pulses would arrive at the receiver with time characteristics more optimal for data recovery. At the same time, second- and third-order fiber effects began to arise as a result of the WDM architecture. These effects arose because of nonlinear refraction, the non-flat gain spectrum of EDFAs, and some polarization-related phenomena. Network architecture design requirements therefore increased dramatically in complexity because of the need to both manage dispersion while controlling the higher-order transmission phenomena [8, 9, 11-12].

Furthermore, IP traffic has grown exponentially with the explosion of advanced internet video applications, requiring fiber-optic network transport capacities to correspondingly grow. This need to grow transport data rates spurred the development and introduction of the coherent optical receiver [13-15] into fiber-optic networks. The coherent optical receiver is analogous to a wireless radio; it provides a local oscillator (LO) at the receiver to downconvert the received waveform to a complex (near) baseband signal for digitization and demodulation. The coherent receiver detects the full phase and amplitude information of the received signal, breaking the paradigm of intensity-modulation and direct-detection that dominated fiber communication since the introduction of the EDFA. With the phase state of the transmitted signal available at the receiver advanced (phase-based) modulation formats could then be introduced into fiber-optic communication systems.

In conjunction with the adoption of the coherent receiver, digital signal processing (DSP) was introduced for optical communication. DSP was (and remains) both a requirement for the success of the coherent receiver and its "killer app." DSP can leverage recent and ongoing advancements in silicon semiconductor technology to digitally correct for chromatic dispersion,

separate co-propagating polarization modes, mitigate nonlinear effects, and equalize the received signal [16]. In addition, techniques for processing could be adapted from wireless (and other) domains, promising quick advancement. The introduction of DSP as enabled by the optical coherent receiver is the single most important technology change in fiber-optic communication since the introduction of the EDFA.

Following past standardization paradigms, the next logical step from 100 Gb/s line rates is to either 400 Gb/s or 1 Tb/s rates. Coherent orthogonal frequency-division multiplexing (OFDM) [17-19] and coherent WDM [20] have been proposed to meet the spectral efficiency requirements of Tb/s channels. Each technique utilizes coherent, phase-locked subcarriers produced via an optical comb generator [21]. This enables baud-rate channel spacing for maximizing spectral efficiency, and is a possible method to meet the Tb/s challenges.

Fiber manufacturing technology has also advanced in order to improve available system margin. An OFS study [22] summarized the major new fiber products of recent years, and estimated their potential performance gains as a function of effective area ($A_{eff}$) increase and attenuation decrease. This study concludes that optimized fiber production techniques have the potential to provide approximately 4 dB advantage over standard single mode fiber (ITU-T G.652 specification [23]) (SSMF) *at most* by doubling the effective area and reducing loss to 90% of its current value. These advances are seen at the limit of process technologies (e.g. micro-bending sensitivity) and silica purification techniques.

The most recent research has identified space-dimension multiplexing (SDM) as a promising method for achieving the next order of magnitude increase in spectral efficiency in the network. Space is the last of four orthogonal dimensions for signal transport to be exploited in fiber systems (the other three are frequency, polarization, and time). SDM for fiber systems has

been proposed as multi-core fibers [5], few-mode fibers [24-26], and a combination of both [27]. Challenges for SDM techniques include efficient amplification, channel multiplexing, and multiple-in, multiple-out (MIMO) signal processing [28]. Despite laboratory success with coherent carriers, SDM, and cutting-edge fibers the paths forward with these technologies are less clear than the move from direct detection to coherent receivers with DSP. The step in network transmitter and receiver complexity is vastly higher. Nevertheless, Huawei [29], ZTE [30], and Ciena [31] have both "announced" Tb/s-class prototype products based on superchannel systems created with an optical comb generator. It remains to be seen whether any of these technologies will be adopted in the future.

### 2.2 The Fiber Channel

Data communication in fiber optics is accomplished by modulating the phase, amplitude, or polarization of a continuous wave laser and then propagating the modulation pulses down an optical fiber. Accordingly, pulse propagation in fiber is governed by the wave equation. Optical fiber is uniquely characterized by three primary physical phenomena – attenuation, dispersion, and nonlinear refraction – which can be included into the wave equation to fully describe pulse propagation. When the wave equation is so elaborated it is called the Nonlinear Schrodinger (NLS) equation [7, 12]. Begin with the electric field of a data pulse

$$E(z,t) = \frac{1}{2}E_0(z,t)\exp\{j\omega_0 t - j\beta(\omega)z\} + c.c. \tag{2.1}$$

where $E_0$ is the complex envelope of the pulse. In a linear medium the phase constant $\beta(\omega) = n_0 k_0$ is a scalar quantity ($n_0$ is the index of refraction and $k_0$ the wave number) and the pulse evolution can be described precisely by inserting (2.1) directly into the wave equation. However, the group velocity dispersion (GVD) of the fiber medium means that each spectral component of

the pulse propagates at a different frequency, so $\beta(\omega) = n(\omega)k_0$. The phase constant can then be expanded in a Taylor series about $\omega_0$:

$$\beta(\omega) = \beta_0 + \beta_1(\omega - \omega_0) + \frac{1}{2}\beta_2(\omega - \omega_0)^2 + \frac{1}{6}\beta_3(\omega - \omega_0)^3 + \cdots \tag{2.2}$$

The coefficients $\beta_n = \partial^n\beta(\omega)/\partial\omega^n$ are calculated per the definition of a Taylor expansion. Generally, we keep only the first three orders of the Taylor expansion. Since the phase constant varies as a function of frequency it is convenient to express the pulse in terms of the Fourier transform. Including (2.2) in (2.1) and taking the Fourier transform we can write

$$E_0(z,t) = \int_{-\infty}^{\infty} A(\omega - \omega_0)\exp\{j(\omega - \omega_0)t\}\exp\{-j(\omega - \omega_0)\beta_1 z\}$$

$$\cdot \exp\left\{-j\frac{1}{2}(\omega - \omega_0)^2\beta_2 z\right\}\exp\left\{-j\frac{1}{6}(\omega - \omega_0)^3\beta_3 z\right\}d(\omega - \omega_0). \tag{2.3}$$

Ordinarily, the procedure from here is to substitute (2.3) into the wave equation, apply the slowly varying envelope approximation (SVA, [7, 12]), and then solve. However, the objective in this case is to identify the constituent terms for propagation velocity and dispersion. So instead the next step is to take the derivative with respect to $t$ and then insert the result into derivative with respect to $z$. The time derivative is

$$\frac{\partial E_0(z,t)}{\partial t} = \int_{-\infty}^{\infty} j\,(\omega - \omega_0)A(\omega - \omega_0)\exp\{j(\omega - \omega_0)t\}\exp\{-j(\omega - \omega_0)\beta_1 z\}$$

$$\cdot \exp\left\{-j\frac{1}{2}(\omega - \omega_0)^2\beta_2 z\right\}\exp\left\{-j\frac{1}{6}(\omega - \omega_0)^3\beta_3 z\right\}d(\omega - \omega_0), \tag{2.4}$$

and the space derivative is

$$\frac{\partial E_0(z,t)}{\partial z} = \int_{-\infty}^{\infty} -j\,(\omega - \omega_0)\beta_1 A(\omega - \omega_0)\exp\{j(\omega - \omega_0)t\}\exp\{-j(\omega - \omega_0)\beta_1 z\}$$

$$\cdot \exp\left\{-j\frac{1}{2}(\omega - \omega_0)^2\beta_2 z\right\}\exp\left\{-j\frac{1}{6}(\omega - \omega_0)^3\beta_3 z\right\}d(\omega - \omega_0)$$

$$+\int_{-\infty}^{\infty} -j\,(\omega-\omega_0)^2\frac{\beta_2}{2}A(\omega-\omega_0)\exp\{j(\omega-\omega_0)t\}\exp\{-j(\omega-\omega_0)\beta_1 z\}$$

$$\cdot\exp\left\{-j\tfrac{1}{2}(\omega-\omega_0)^2\beta_2 z\right\}\exp\left\{-j\tfrac{1}{6}(\omega-\omega_0)^3\beta_3 z\right\}d(\omega-\omega_0)$$

$$+\int_{-\infty}^{\infty} -j\,(\omega-\omega_0)^3\frac{\beta_3}{6}A(\omega-\omega_0)\exp\{j(\omega-\omega_0)t\}\exp\{-j(\omega-\omega_0)\beta_1 z\}$$

$$\cdot\exp\left\{-j\tfrac{1}{2}(\omega-\omega_0)^2\beta_2 z\right\}\exp\left\{-j\tfrac{1}{6}(\omega-\omega_0)^3\beta_3 z\right\}d(\omega-\omega_0). \quad (2.5)$$

By inserting (2.4) into (2.5) the following equation can be assembled:

$$\frac{\partial E_0(z,t)}{\partial z} = -\beta_1\frac{\partial E_0(z,t)}{\partial t} + j\frac{\beta_2}{2}\frac{\partial^2 E_0(z,t)}{\partial t^2} + \frac{\beta_3}{6}\frac{\partial^3 E_0(z,t)}{\partial t^3}. \quad (2.6)$$

The first term on the right hand side of (2.6) is the reciprocal of the group velocity $v_g = \beta_1^{-1}$ at $\omega_0$. The second two terms are the quadratic and cubic dispersion effects on the pulse envelope. Generally, $\beta_2$ is re-cast in terms to define the fiber dispersion parameter $D = -2\pi c\beta_2/\lambda^2$, which relates the group delay variation to changes in wavelength and is often expressed in picoseconds of pulse spread per kilometer traveled per nanometer of pulse bandwidth.

Let us now proceed forward from the dispersion analysis to include a general, time-varying index of refraction in our pulse propagation model. In the absence of dispersion, the wave equation may be written to include a time-varying index in this way:

$$\frac{\partial^2 E(\mathrm{z,t})}{\partial z^2} - \frac{\partial^2}{\partial t^2}[\mu_0\epsilon_0 n^2 E_0(z,t)] = 0. \quad (2.7)$$

In optical fiber the index of refraction is proportional to the intensity of the electric field being carried. Therefore changes in the electric field (a necessity for data communication) induce perturbations in the index of refraction which in turn causes variations in the speed the signal travels. Importantly, no transfer of energy takes place. The origin of this phenomena is the third-order susceptibility ($\chi^{(3)}$) which describes the nonlinear Polarizability of the silica medium and

gives rise to third-harmonic generation and four-wave mixing (FWM) [11]. Third-harmonic generation and some four-wave processes require phase-matching to achieve efficiency which is generally not attained in WDM fiber communication systems. Consequently, most nonlinear effects in fiber arise from degenerate FWM. These degenerate nonlinear effects can be conveniently described the Kerr coefficient $n_2'$ which relates the refractive index $n$ to the intensity of the optical field [32]

$$n = n_0 + n_2'|E_0(z,t)|^2. \tag{2.8}$$

The Kerr coefficient (also called the nonlinear index) is given by [7]

$$n_2' = \frac{3}{8n_0}\chi_{xxxx}^{(3)}. \tag{2.9}$$

In pure silica, $n_2' = 2.3\text{x}10^{-22}\ m^2V^{-2}$ [7, 32].

Because the fiber index changes as a function of electric field intensity a traveling pulse necessarily experiences a change in speed of propagation proportional to a change in field intensity. This speed of propagation change can be interpreted as a phase shift with magnitude $\phi = nk_0L$, where $L$ is the length of fiber traversed. Self-phase modulation (SPM) is the self-induced phase shift experienced by the pulse. That is, the phase shift induced the change in intensity of the electric field of the pulse itself. Since phase modulation is analogous with frequency generation, SPM can cause pulse broadening, induce chirp, or interact with dispersion to appear as noise in the received signal [11] or to generate solitons [7, 11, 32].

Cross-phase modulation (XPM) is the other main phenomenon that arises because of the nonlinear refractive index. WDM systems inherently propagate independent channels at multiple wavelengths and two polarizations; these neighboring channels interact via nonlinear refraction to modulate the phase of adjacent channels. The strength of XPM effects are both polarization- and wavelength-dependent. XPM effects are a degenerate subset of the phenomena of four-wave

mixing (FWM). FWM is a third-order Kerr-nonlinearity in silica fibers; it generates a fourth signal based upon the mixing products of three others, $f_g = f_i + f_j - f_k$, where the magnitude of the generated signal is proportional to $\gamma^2 P_i P_j P_k$ [33]. The frequency-generation terms of FWM require phase-matching between co-propagating pulses and polarizations and any slight reduction in phase-matching weakens the effect. Since optical fiber exhibits a frequency-dependent group velocity profile, co-propagating pulses and different wavelengths can "walk-off" from each other. If pulses exceed their walk-off length $L_W = T_0/|\beta_1(\lambda_1) - \beta_1(\lambda_2)|$ then they cease to interact efficiently in the FWM manner. Analogously, if pulses of different polarization exceed their beat length $L_B = 2\pi/|\beta_x - \beta_y|$ then they too cease to interact efficiently via the FWM effect [7]. Because of this dispersion-induced walk-off between wavelengths and polarizations, the XPM effects of FWM are often the most dominant for coherent systems. Non-degenerate FWM dominates for extremely dense "superchannel" WDM systems [33]. Let us first analyze the polarization-dependent nature of XPM.

We can re-write (2.1) to include an arbitrary polarization state

$$\boldsymbol{E}(\boldsymbol{r}, t) = \frac{1}{2}\left(E_x \hat{x} + E_y \hat{y}\right) \exp\{j\omega_0 t\} + c.c., \tag{2.10}$$

where $E_x$ and $E_y$ are the complex envelopes of the polarization components of the electric field at a single frequency $\omega_0$. If we treat fiber as an isotropic medium (a good approximation [7]), the nonlinear polarization vector can then be written

$$P_{NL}(r, t) = \frac{1}{2}\left(P_x \hat{x} + P_y \hat{y}\right) \exp\{j\omega_0 t\} + c.c. \tag{2.11}$$

In (2.11), $P_x$ and $P_y$ are given by

$$P_i = \frac{3}{2}\epsilon_0 \sum_j \left(\chi^{(3)}_{xxyy} E_i E_j E_j^* + \chi^{(3)}_{xyxy} E_j E_i E_j^* + \chi^{(3)}_{xyyx} E_j E_j E_i^*\right), \tag{2.12}$$

where $i, j = x$ or $y$. The components of the third-order susceptibility $\chi^{(3)}$ are nearly the same magnitude for silica fiber and can be related by

$$\chi^{(3)}_{xxxx} = \chi^{(3)}_{xxyy} + \chi^{(3)}_{xyxy} + \chi^{(3)}_{xyyx} \approx 3\chi^{(3)}_{xxyy} \approx 3\chi^{(3)}_{xyxy} \approx 3\chi^{(3)}_{xyyx}. \tag{2.13}$$

Using the simplification that the components of $\chi^{(3)}$ truly are identical (our isotropic assumption) (2.13), the polarization components $P_x$ and $P_y$ can be written as

$$P_x = \frac{3}{4}\chi^{(3)}_{xxxx}\left[\left(|E_x|^2 + \frac{2}{3}\left|E_y\right|^2\right)E_x + \frac{1}{3}\left(E_y E_x^*\right)E_y\right], \tag{2.14}$$

$$P_y = \frac{3}{4}\chi^{(3)}_{xxxx}\left[\left(\left|E_y\right|^2 + \frac{2}{3}|E_x|^2\right)E_y + \frac{1}{3}\left(E_x E_y^*\right)E_x\right]. \tag{2.15}$$

The last term in (2.14) and (2.15) depends on the phase matching between orthogonal states of polarization which is determined by the beat length $L_B$ of the fiber medium. If the fiber length is much longer than its beat length, then this last term contributes negligibly [7].

The nonlinear contribution of XPM can be computed as

$$\Delta n_x = n_2'\left(|E_x|^2 + \frac{2}{3}\left|E_y\right|^2\right), \tag{2.16}$$

$$\Delta n_y = n_2'\left(\left|E_y\right|^2 + \frac{2}{3}|E_x|^2\right). \tag{2.17}$$

An analysis for XPM can now be conducted (for each polarization) that follows the steps for SPM in (2.7) to include XPM for two polarizations in the NLS. This analysis yields a pair of coupled equations that govern the evolution of the two polarization components. Note that for the case of an electric field propagating on a single polarization (either $E_x$ or $E_y = 0$), this analysis reduces to the purely SPM result of (2.8).

XPM also causes interactions between waves of different frequencies. Again, we can re-write the electric field equation (2.1) to include two frequencies on the same polarization

$$\boldsymbol{E}(\boldsymbol{r}, t) = \frac{1}{2}\hat{x}(E_1 \exp\{j\omega_1 t\} + E_2 \exp\{j\omega_2 t\}) + c.c. \tag{2.18}$$

Substituting (2.18) into the nonlinear polarization equation it can be demonstrated that the strengths of the nonlinear polarization at $\omega_1$ and $\omega_2$ are

$$P_{NL}(\omega_1) = \chi_{\text{eff}}(|E_1|^2 + 2|E_2|^2)E_1, \tag{2.19}$$

$$P_{NL}(\omega_2) = \chi_{\text{eff}}(|E_2|^2 + 2|E_1|^2)E_2, \tag{2.20}$$

where $\chi_{\text{eff}} = 3\epsilon_0\chi^{(3)}_{xxxx}/4$ [7, 11]. Note the dependence of the nonlinear polarization (and implicitly the change in nonlinear index) equal to twice the intensity of the adjacent (in wavelength) electric field. Quickly, the change in index due to this nonlinear polarization dependence is

$$\Delta n_j = n_2' \left(\left|E_j\right|^2 + 2\left|E_{3-j}\right|^2\right), \tag{2.21}$$

where $j = 1$ or 2.

Now we will construct the final form of the NLS which includes loss, dispersion, SPM, and XPM for one polarization on one wavelength. This analysis is identically repeatable for each polarization and each wavelength, yielding a set of coupled equations that describe all of the SPM and XPM interactions.

Let us use a pulse shape that combines (2.10) and (2.18) to include explicitly two polarizations and two frequencies

$$\boldsymbol{E}(\boldsymbol{r}, t) =$$

$$\frac{1}{2}\hat{x}(E_{1x}\exp\{j\omega_1 t\} + E_{2x}\exp\{j\omega_2 t\}) + \frac{1}{2}\hat{y}\left(E_{1y}\exp\{j\omega_1 t\} + E_{2y}\exp\{j\omega_2 t\}\right) + c.c. \tag{2.22}$$

From (2.22) we can apply the analysis of SPM and XPM above to craft an expression for nonlinear refractive index change on the x-polarization [7, 11, 35]

$$\Delta n_x = n_2' \frac{8}{9}\left(|E_{1x}|^2 + \left|E_{1y}\right|^2 + 2|E_{2x}|^2 + \left|E_{2y}\right|^2\right). \tag{2.23}$$

Note that this expression neglects the crossterm $E_{2x}E_{2y}^{*}E_{1y}$ which requires phase matching between the constituent field components (more on this shortly). For a large number of co-propagating frequencies and polarizations XPM becomes based on the ensemble average of the total intensity of the electric field. Thus it is insufficient to have constant intensity in each channel to avoid nonlinear refraction due to XPM. However, the peak ensemble intensity (which is usually determined by the peak intensity of each carrier) largely determines the maximum XPM effect, so reducing the peak-to-average power can provide some benefit to avoiding nonlinear noise. And because XPM interactions are determined by this ensemble intensity average they cannot be deterministically calculated unless all WDM channel could be received and processed simultaneously. Therefore XPM is usually modeled and a random phase noise process that restricts the total launch power. Indeed, it can be shown [8, 36] that XPM is the main capacity-limiting effect in fiber communication.

To insert (2.23) into the wave equation we make the approximation

$$n_x^2 \sim n_0^2 + 2n_0\Delta n_x \tag{2.24}$$

for small $n_2'$. Using the slowly-varying envelope approximation and inserting the pulse shape (2.22) along with the nonlinear index (2.23) into the wave equation for $E_{1x}$ without dispersion (2.7), we can generate the following solution

$$\frac{\partial E_{1x}}{\partial z} = -\beta_{1x}\frac{\partial E_{1x}}{\partial t} - j\gamma\frac{8}{9}\left(|E_{1x}|^2 + \left|E_{1y}\right|^2 + 2|E_{2x}|^2 + \left|E_{2y}\right|^2\right)E_{1x}. \tag{2.25}$$

Here we have also substituted the definition of the nonlinear coefficient $\gamma = n_2'\omega/cA_{\text{eff}}$, where $A_{\text{eff}}$ is the effective area of the fiber in $\text{um}^2$. And in the case of zero group dispersion, $\beta_1 = \beta_0/n_0$.

In general, both $n_2'$ and $\beta_2$ are small. Therefore the effects of quadratic (and cubic) dispersion and the nonlinear refractive index can be included a single equation by the simple

addition of their propagation terms from (2.6). The loss of the optical fiber and saturable gain of any amplifiers can also be included with a similar addition. The final form of the basic Nonlinear Schrodinger equation for electromagnetic propagation in optical fiber can then be written as

$$\frac{\partial E_{1x}}{\partial z} = \frac{g(z)-\alpha}{2}E_{1x} - \beta_{1x}\frac{\partial E_{1x}}{\partial t} + j\frac{\beta_{2x}}{2}\frac{\partial^2 E_{1x}}{\partial t^2} + \frac{\beta_{3x}}{6}\frac{\partial^3 E_{1x}}{\partial t^3}$$
$$-j\gamma\frac{8}{9}\left(|E_{1x}|^2 + \left|E_{1y}\right|^2 + 2|E_{2x}|^2 + \left|E_{2y}\right|^2\right)E_{1x}. \quad (2.26)$$

From here we must then generate the propagation equations for $E_{2x}$, $E_{1y}$, and $E_{2y}$ using the steps outlined in the preceding paragraphs. These four coupled equations together describe the loss, dispersion, and nonlinear refraction of pulses propagating at two different frequencies with two polarization components. It is clear that an analytical approach for demonstrating wave propagation in fiber in unwieldy for any reasonable number of wavelengths and instead requires numerical simulations. Examples of commercial tools for these computational needs are RSoft OptSim [37] and VPI TransmissionMaker [38].

## 2.3 System Components

The basic component building blocks for fiber-optic networks are the transmitter laser, external modulator, WDM channel filter, amplifier, and receiver. These components impose the practical bandwidth and performance limitations in a fiber-optic network.

Current fiber-optic transmitters employ a tunable (wavelength and power) laser source with an external modulator. Some systems utilize directly-modulated lasers, although these are less common. Distributed feedback (DFB) and external cavity (EC) are the most commonly used types of lasers in telecommunications. DFBs meet the power, tunability, and linewidth (a measure of oscillator phase noise) requirements for 10 Gb/s and 40 Gb/s systems. ECLs can offer

an order of magnitude advantage in linewidth compared to DFBs and are the leading choice for deployment in coherent systems (especially for the LO).

External modulators for telecommunications are manufactured in Lithium Niobate ($LiNbO_3$). An electric field can induce index of refraction changes in $LiNbO_3$ structures, proportional to the strength of the field. To make a modulator, $LiNbO_3$ is shaped into a waveguide structure with an electrode attached along the length of the waveguide. A single waveguide and electrode thus yields phase-only modulation.

The immediate (and first) application of this technology is as a constituent part of an inferometer. Following the diagram of Fig. 2.1, one can split a single $LiNbO_3$ waveguide into two equivalent paths and then apply electrodes to the two parallel waveguides. With careful manufacturing controls and processes, photons traveling in both waveguides will remain in phase with each other (coherent). Then, by adjusting the DC and RF components of the applied electric fields across the waveguides, the two paths can be tuned to a desired relative phase. Thus, constructive or destructive interference can be achieved by recombining the photons in parallel waveguides. This complete structure is called the Mach-Zehnder Inferometer (MZI) or Modulator (MZM).

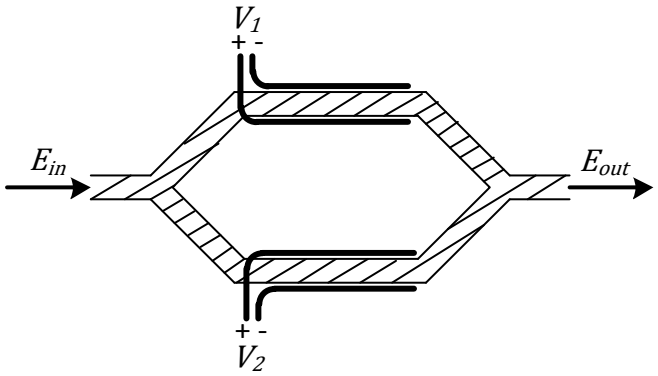


Figure 2.1. Waveguide structure of a Mach-Zehnder Inferometer. The diagonal lines are the $LiNbO_3$ waveguide structures and the thick black lines along the waveguides are the RF electrodes.

The electric field transfer function of a MZI is

$$\frac{E_{out}}{E_{in}} = \frac{1}{2}\left[\exp\left\{\frac{j\pi V_1}{V_\pi}\right\} + \exp\left\{\frac{j\pi V_2}{V_\pi}\right\}\right]. \tag{2.27}$$

In (2.27), $V_1$ and $V_2$ are the voltages applied to the parallel electrodes and $V_\pi$ is the voltage that induces a $\pi$ phase shift in the photons traveling through the waveguide. $V_\pi$ is very much a design optimization variable; it is determined by the qualities of manufacture (and lower is usually better) and is different for nearly all modulators. Another way of writing the transfer function is

$$\frac{E_{out}}{E_{in}} = \cos\left(\frac{\pi V_D}{2V_\pi}\right)\left[\cos\left(\frac{\pi V_C}{V_\pi}\right) + j\sin\left(\frac{\pi V_C}{V_\pi}\right)\right], \tag{2.28}$$

where we have made the substitution $V_C = (V_1 + V_2)/2$ and $V_D = (V_1 - V_2)$ for the common-mode and differential voltages. One common method of driving the modulator is by setting $V_1 = -V_2$. In this configuration, the electric field output is either in-phase or 180 degrees out of phase with respect to the input, $E_{out} = E_{in}\cos(\pi V_D/V_\pi)$. Note that the relationship between $E_{out}$ and $E_{in}$ is nonlinear (cosine).

Quadrature modulation can be achieved by inserting two independent MZIs into the paths of an outer third MZI, Fig. 2.2. The outer MZI is controlled to have a 90 degree relative phase difference between its two arms. This structure must be implemented as an integrated device to ensure coherence of all of the optical waveguides and electrode path matching.

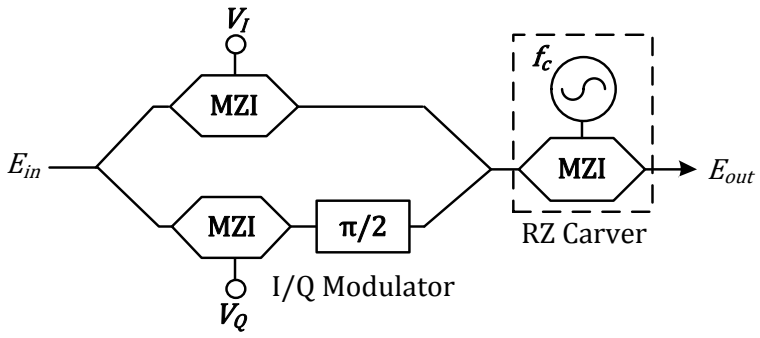


Figure 2.2. I/Q modulator constructed from three nested MZIs (2.1). To achieve the required carrier coherence along the waveguide paths this structure is general integrated in a single package. Return-to-zero carving (dashed box) can be optionally achieved with an external (or integrated) MZI driven by the symbol clock signal.

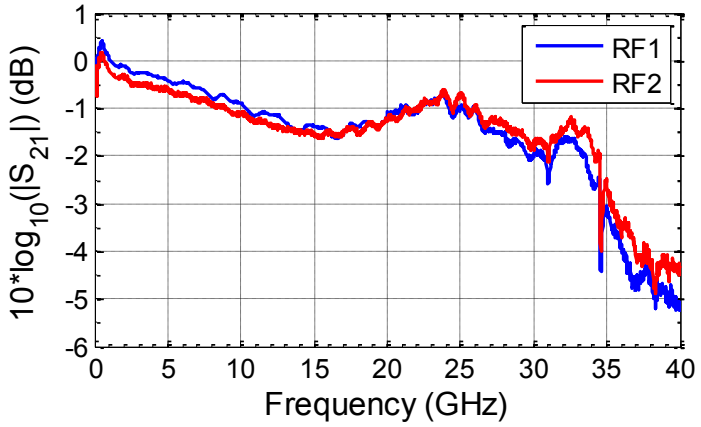


Figure 2.3. $S_{21}$ measurement of the Oclaro I/Q modulator used in the experiments in this dissertation. The frequency response diagram here is typical of modulators that can support the ~30 GHz baud rates required in modern coherent lightwave systems.

Channels in WDM networks are typically routed using reconfigurable add/drop multiplexors (ROADMs). ROADMs are comprised of optical filters that individually select WDM channels to drop or add. ROADM filters are typically deployed to service channels arranged on the 50 GHz ITU-T grid [39]. These shapes of these filters are determined by the technology used to implement them. Often, however, the optical channel filters closely resemble a super-Gaussian transfer function which can we modeled as

$$H_{SG}(f) = \exp\left\{-\ln 2\left[\frac{|f|}{B}\right]^{2N}\right\}, \tag{2.29}$$

where $N$ is the order of the filter and $B$ is the bandwidth. Typically commercial filters have order $N$ between four and six. Optical networks are typically deployed in "mesh" configurations, so WDM channels are usually subjected to a cascade of ROADM filters to reach their destination. This concatenation of filters will result in a net narrowing of the total bandpass experienced by the WDM channel (compared to a single filter). Figure 2.4 compares three commercial channel filters used in WDM networks against a super-Gaussian filter of order 4. Filters 1, 2, and 3 of Fig. 2.4 are based on liquid-crystal on silicon (LCOS) [40], digital light processor (DLP) [41], and arrayed waveguide (AWG) technologies [42], respectively.

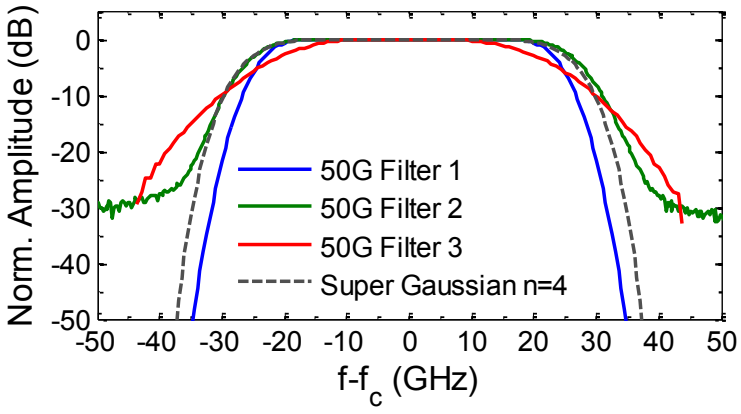


Figure 2.4. Comparison of three, 50-GHz channel filter technologies against a super-Gaussian filter of order 4. The filters 1, 2, and 3 are based on LCOS [40], DLP [41], and AWG [42] technologies, respectively.

There are two primary amplifier technologies for optical telecommunications: the EDFA and the Raman amplifier. The EDFA is comprised of a short length of fiber doped with Erbium and pumped by either (and sometimes with both) a 980 nm or 1480 nm high-power laser. The pump laser induces population inversion in the Erbium atoms. Incoming photons (the telecommunications signal) stimulate the Er+ Ions to decay ($\tau_D \sim 10$ ms) by emitting extra photons at the same phase and frequency (1520 – 1570 nm). However, EDFAs also generate spontaneous emission photons that are incoherent with the incoming signal and amplify spontaneous emissions from previous inline EDFAs. This characteristic is called amplified spontaneous emission (ASE) and is one of the performance-limiting noise components in optical communications systems. ASE arises because of quantum-mechanical field fluctuations in photons and their corresponding spontaneous (random) decay from the excited (inverted) state. Remarkably, and despite its origin, ASE can be modeled [7-11] as a random *classical* field with an additive Gaussian distribution that is circularly symmetric in phase and amplitude.

Fiber Raman amplifiers exploit the Stimulated Raman scattering effect in fiber by pumping the transmission fiber about 13 THz above the desired gain frequency. Raman amplifiers therefore utilize the transmission fiber itself as the gain medium, distributing the total

gain along the length of the fiber. If the pump power is chosen carefully the gain induced by the pump laser can exactly equal the loss induced by the fiber medium, forcing the signal to maintain a constant average power along the fiber. This ideal distributed-gain configuration enables higher delivered signal-to-noise ratios (SNRs) than EDFAs [8].

EDFAs are generally limited to C-band (1520-1570 nm) and Raman amplifiers can provide gain at C-band wavelengths by pumping the fiber around 1460-1480 nm. Unlike EDFAs, Raman amplifiers can provide gain at any wavelength, opening the possibility to transport data at other low-loss wavelength bands such as the 1310 nm window and the S-band (< 1528 nm). While these transport bands offer unique challenges compared to C-band, Raman amplification enables the possibility of a network that deploys data communication channels across the entire low-loss region of the optical fiber. Furthermore, tight control of Raman pump wavelengths and powers can tailor the gain spectrum to match any need [8, 9].

After a transmitted signal passed through and optical link it can be selected by an optical filter at the receive side. The signal may then be detected directly, differentially, or coherently. A direct detection receiver is simply a photodiode and electrical amplitude and is capable of discern amplitude modulation. Current generation optical networks operating at 10 Gb/s and 40 Gb/s generally utilize direct detection schemes to receive on-off keying (OOK) signals. Differential (also called interferometric or self-coherent) receivers employ optical arrangements that enable direct detection schemes to receive phase-based formats like differential phase-shift keying (DPSK) and differential quadrature phase-shift keying (DQPSK), but cannot directly recovery phase information of the signal, preventing optical networks from employing other advanced modulation formats. Figure 2.5 is a schematic of two differential receiver rchitectures.

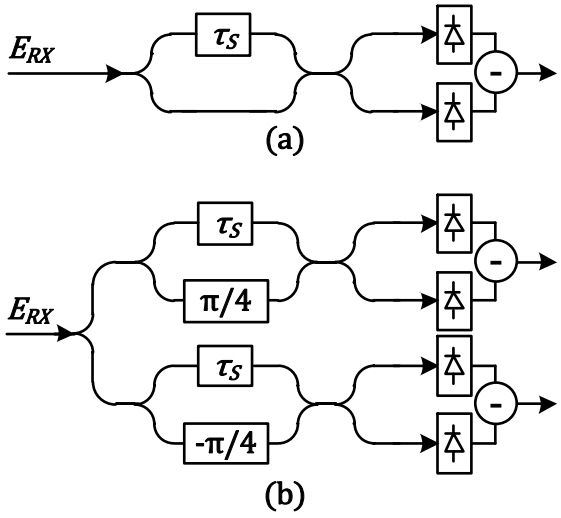


Figure 2.5. Differential receiver architectures for (a) BPSK/DPSK and (b) DQPSK.

Direct detection offers the advantage of simplicity. It requires no laser at the receiver, and needs only a slicer and clock recovery circuit at the output of the photodetector. However, the differential direct detection schemes limit post digital signal processing because the receiver optical signal has already undergone an irreversible nonlinear transformation through the interferometer and square-law photodiode pair. All signal processing (e.g., chromatic dispersion compensation, polarization demultiplexing, equalization) for direct-detection systems must consequently be performed before detection. Furthermore, direct detection does not benefit from any LO gain, limiting receiver sensitivity. Optical coherent receivers have therefore been adopted for next-generation optical data transmission.

Optical coherent receivers are directly analogous to wireless or wireline radios – they mix a local oscillator with the received signal to downconvert the waveform to (or near) baseband for demodulation. In the ideal homodyne case, a coherent receiver linearly translates the channel of interest into a complex electrical baseband waveform. The general structure of a single-polarization coherent optical receiver is depicted in Fig. 2.6.

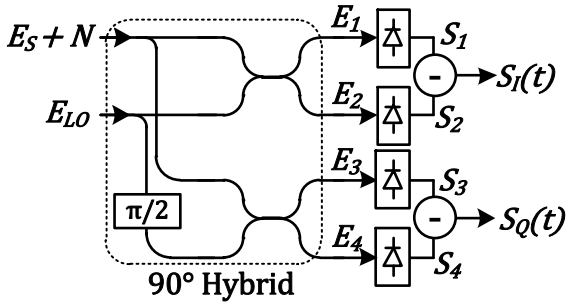


Figure 2.6. One polarization of an optical coherent receiver. A complete polarization-diverse coherent receiver will employ a pair of these structures, one for each polarization. Note that in optical communication systems coherent receivers are usually deployed in a dual-polarization configuration.

The complex envelope of the received optical signal field $E_s(t)$ plus noise $N(t)$ is first added to the co-polarized LO $E_{LO}$ via a 90° optical hybrid. Synonymous with an RF hybrid, the optical hybrid enforces a 90° phase shift on one side of the LO path thus allowing the subsequent mixing to extract the quadrature components of $E_s(t)$. The two-input, four-output 90° optical hybrid of Fig. 2.6 can be described by the matrix transfer function

$$\begin{bmatrix} E_1 \\ E_2 \\ E_3 \\ E_4 \end{bmatrix} = \begin{bmatrix} \sqrt{1-\epsilon} & \sqrt{\epsilon} \\ \sqrt{\epsilon} & \sqrt{1-\epsilon} \\ \sqrt{1-\epsilon} & j\sqrt{\epsilon} \\ \sqrt{\epsilon} & j\sqrt{1-\epsilon} \end{bmatrix} \begin{bmatrix} E_s + N \\ E_{LO} \end{bmatrix}, \tag{2.30}$$

where $\epsilon$ is the power transfer coefficient of the optical combiner (ideally $\epsilon = 0.5$). After the square-law photodetectors with responsivity $R$, the four electrical signals $S_k(t) = R_k|E_k(t)|^2$ are

$$S_1 = R_1\left[(1-\epsilon)(|E_s|^2 + |N|^2 + 2\mathrm{Re}\{E_s N^*\}) + \epsilon|E_{LO}|^2 + 2\sqrt{\epsilon(1-\epsilon)}\mathrm{Re}\{E_s E_{LO}^* + N E_{LO}^*\}\right], \tag{2.31a}$$

$$S_2 = R_2\left[\epsilon(|E_s|^2 + |N|^2 + 2\mathrm{Re}\{E_s N^*\}) + (1-\epsilon)|E_{LO}|^2 - 2\sqrt{\epsilon(1-\epsilon)}\mathrm{Re}\{E_s E_{LO}^* + N E_{LO}^*\}\right], \tag{2.31b}$$

$$S_3 = R_3\left[(1-\epsilon)(|E_s|^2 + |N|^2 + 2\mathrm{Re}\{E_s N^*\}) + \epsilon|E_{LO}|^2 + 2\sqrt{\epsilon(1-\epsilon)}\mathrm{Im}\{E_s E_{LO}^* + N E_{LO}^*\}\right], \tag{2.31c}$$

$$S_4 = R_4\left[\epsilon(|E_s|^2 + |N|^2 + 2\mathrm{Re}\{E_s N^*\}) + (1-\epsilon)|E_{LO}|^2 - 2\sqrt{\epsilon(1-\epsilon)}\mathrm{Im}\{E_s E_{LO}^* + N E_{LO}^*\}\right]. \tag{2.31d}$$

If the photodiodes are perfectly balanced ($R_k = R$) and the optical combiners perfectly matched ($\epsilon = 0.5$) the receiver rejects all common-mode direct-detection photocurrents, yielding

$$S_I(t) = 2R\ \mathrm{Re}\{E_s(t)E_{LO}^* + N(t)E_{LO}^*\}, \tag{2.32a}$$

$$S_Q(t) = 2R\ \mathrm{Im}\{E_s(t)E_{LO}^* + N(t)E_{LO}^*\}. \tag{2.32b}$$

In an ideal homodyne receiver, $E_{LO}$ is both temporally static and a perfect phase reference to the incoming optical field. That is, $E_{LO}$ is phase-locked to $E_s(t)$ and the term $E_{LO}^*$ is a constant scalar, enabling the photocurrents $S_I$ and $S_Q$ to vary proportionally to the real (I, in-phase) and imaginary (Q, quadrature) parts of the received signal. The coherent receiver is therefore capable of detecting the complex envelope of the in-phase and quadrature components of two linear polarization modes (albeit at an arbitrary orientation [43-44]).

In almost all practical systems transmission systems the requirement that the local oscillator be phase-locked to the signal carrier is too strict. Generally, the LO is allowed to be free-running; its phase drifts slowly (compared to the symbol period) and randomly in time relative to the carrier phase. This relative phase drift appears as phase distortion (or noise) in the received electrical signal and must be compensated. A full description of how carrier phase recovery is accomplished appears in §3.

The first term on the right-hand side of equations (2.32a-b) is the desired signal term. The second term is the LO-noise beat term (the only beat term of relevance – both the signal-noise and noise-noise beat terms are eliminated in ideal balanced detection). Because a coherent receiver operates as a linear transformation the statistics of the both the signal and noise optical fields are preserved in the conversion to an electrical waveform. In contrast, direct-detection receivers with one or more delay inferometers (see Fig. 2.5) usually yield non-Gaussian noise statistics.

The variance of the LO-noise beat term is *beat noise*, which requires that the optical fields be stochastic in nature. *Shot noise*, however, is a fundamental part of any optical coherent

receiver and is a direct consequence of the quantum nature of light. It manifests as random fluctuations in received photocurrent. In an ideal photodetector, shot noise tends to a Poisson distribution. And for time-varying optical power (which is necessarily the case for communications systems), shot noise becomes time-varying and therefore nonstationary. Shot noise is described in detail in [8, 10] and can be shown to be essentially negligible compared to the LO-noise beat term for almost any distance of transmission.

Finally, it is important to note that all electronic components exhibit other sources of noise (thermal noise, transistor shot noise, $1/f$ noise, etc.). These electronic sources of noise are often statistically independent, and can be lumped together and added to output of the photodetectors (2.32). However, the variance of LO-noise beat noise can be made arbitrarily large by increasing the power of the LO making the electronic noise additions largely negligible [8].

The advantages of coherent detection compared to direct detection can be summarized in three points.

1. The coherent receiver offers received signal gain proportional to the LO power, lowering receiver sensitivity.
2. The output electrical photocurrent is a linear transformation of the optical signal field (containing full phase and amplitude information).
3. The coherent receiver enables digital signal processing in the electronics domain.

In general, advantage (3) follows directly from (2). DSP techniques have advanced at a breathtaking pace in the past decade and have largely driven the exponential proliferation of wireless and mobile electronics. With the introduction of optical coherent receivers, DSP

algorithms can compensate and correct for nearly all of the myriad channel impairments of a fiber-optic system in the purely electronic domain.

# CHAPTER 3

# THE DIGITAL RECEIVER FOR FIBER OPTIC NETWORKS

The digital optical coherent receiver is the critical enabling technology for fiber optic networks with line rates beyond 10 Gb/s. The coherent optical receiver recovers the full phase and amplitude information of a received signal; the output currents of the balanced photodiodes ($S_k$ in Fig. 2.6) are proportional to the mixing product of the signal and LO electric fields which contains both the amplitude and phase information of the signal field. Typically the photocurrent is transformed to a voltage signal via a linear transimpedance amplifier (TIA) for digitization. A polarization-diverse optical coherent receiver employs two hybrids depicted in Fig. 2.6 (one for each polarization mode), thus providing four analog voltage waveforms (I and Q on two polarizations) to the digitizer. After digitization the samples must be fed into a signal processing engine to recover the original transmitted data. Recovery of electric field phase information and digitization simplifies reception of complex-valued modulation formats, provides a common receive front end, and allows for polarization and phase tracking. The coherent receiver also enables compensation of both linear [16] and nonlinear fiber channel impairments [48].

In wide area networks (WANs) the limited (albeit large) bandwidth of EDFA requires network operators to continually increase the spectral efficiency of their transport network over previous generation technology in order to meet traffic growth. This paradigm demands multilevel modulation formats and polarization division multiplexing (PDM). Furthermore, the

existing infrastructure for metro and regional networks is populated by multiple ROADMs to enable flexible data routing and dynamic channel configuration. ROADM channels filters are most often implemented on a 50 GHz or 100 GHz grid, with a complete transition to 50 GHz expected for 100 Gb/s payload rates. These ROADM channel filters are the de facto filtering limitations for each WDM channel.

To achieve adequate performance with 100 Gb/s nominal payload rates, lines rates of at least 112-128 Gb/s are need to accommodate forward error correction (FEC) [49-51]. FEC has radically altered the design constraints of optical links: a pre-FEC bit-error rate (BER) of $10^{-3}$ or $10^{-2}$ yields < $10^{-12}$ post-FEC error rates with "hard" [50] and "soft" [51] codes, respectively. Because the 3 dB bandwidth of cascaded ROADMs is often less than 40 GHz (the exact number being highly network, route, and technology dependent; see Fig. 6.3), a spectral efficiency (SE) of $112/40 = 2.8\, b/s/Hz$ is required for 100 Gb/s transmission on a single wavelength. The BER requirements of FEC are generally the target metric for optical transmission experiments in the laboratory as we will see in later chapters.

While there are several modulation formats capable of achieving SE ≥ 2.8 b/s/Hz, research over the past several years has concluded that 28-32 Gbaud PDM quadrature phase shift keying (QPSK) is a promising approach for 100G line rates. The single-polarization QPSK signal is mathematically described as follows:

$$s(t) = \sqrt{\frac{2E_s}{T_s}} \sum_{m=-\infty}^{+\infty} \left(a_{I,m} \cos(2\pi f_c t) - a_{Q,m} \sin(2\pi f_c t)\right) g(t - mT_s). \qquad (3.1)$$

The complex symbol $a_m = (a_{I,m} + j a_{Q,m})$ takes the values $(\pm 1 \pm j)$ and $g(t)$ is the pulse shape (which may span more than one symbol). In optical systems, the pulse shape is determined by the low-pass transfer function of the external modulator structure, Fig. 2.3, the drive electronics, and by the optional use of return-to-zero (RZ) pulse carving, Fig. 2.2. Additionally, optical

channel filters of DWDM configurations, Fig. 2.4, affect the pulse shape; the cascaded behavior of these components is an area of active research both in this dissertation (§6, 7, and 9) and elsewhere [52].

PDM-QPSK is the optimal 16-ary modulation format because it encodes its sixteen symbol values onto four dimensions with binary modulation in each dimension (in-phase and quadrature for each of X and Y polarizations). In theory the linear noise performance of QPSK is identical to binary phase shift keying (BPSK) at the same bit rate [53]. QPSK also offers tolerance to multiple ROADM passes, CD, and nonlinear effects, and is capable of transmission distances greater than 1600 km (see §8), making it viable for more than 80% of potential link distances. PDM-QPSK has subsequently been adopted as the de facto standard by the Optical Internetworking Forum (OIF) for 100G transponders [54, 55]. However, the OIF has selected neither non return-to-zero (NRZ) nor RZ signaling, leaving the decision to carriers.

The next logical step to maximize spectral efficiency while still retaining the 50 GHz ITU grid paradigm is to move from PDM-QPSK to PDM-16-ary quadrature amplitude modulation (QAM). Single-polarization 16QAM can be mathematically written identically to Eqn. 3.1 by simply allowing the message symbols to take the values $a_{I,m}$ or $a_{Q,m} = \pm 1$ or $\pm 3$. Adding two possible values to the message symbols increases spectral efficiency by 2 b/s/Hz over PDM-QPSK.

Per the characteristics of the fiber channel (described in detail in §2), there are four primary processing steps that the DSP engine must perform regardless of the signal modulation format: (1) CD compensation, (2) polarization demultiplexing, (3) symbol timing recovery, and (4) carrier phase recovery. These four steps account for pulse smear because of CD, arbitrary polarization rotation after propagation, asynchronous sampling of the digitizer, and carrier-LO

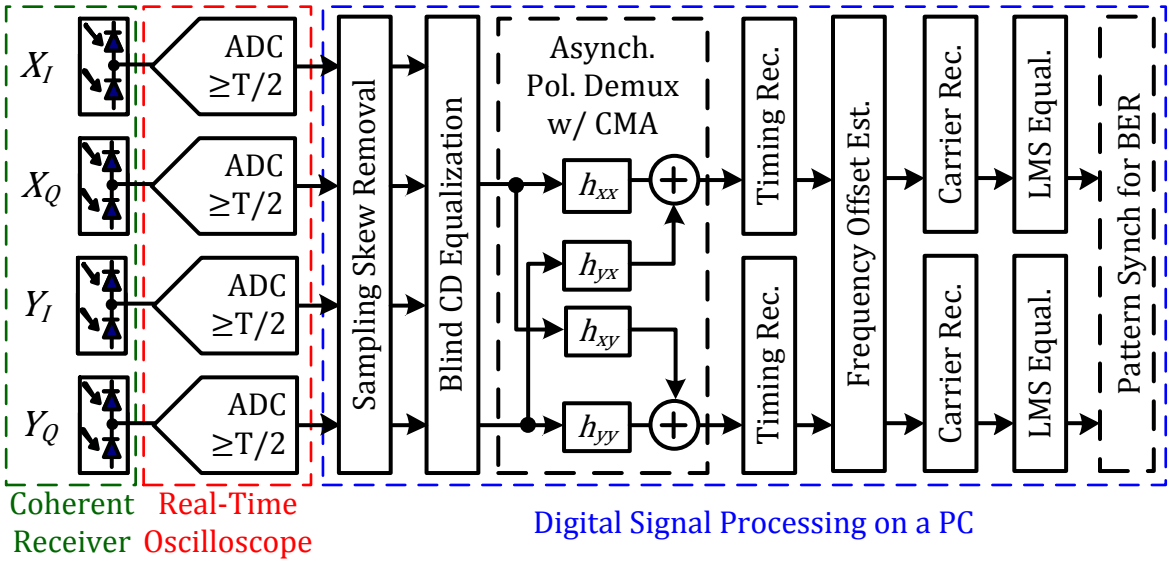


Figure 3.1. General signal processing flow for PDM-QPSK. Each processing step is implemented individually and independently. The cascade of steps is operated module-by-module.

frequency drift due to non-zero laser linewidths, respectively. This remainder of this section will focus on the specific DSP algorithms that recover PDM-QPSK and how they are modified to accommodate PDM-16QAM.

### 3.1. Digital Signal Processing for PDM-QPSK

The signal processing flow for PDM-QPSK after fiber transmission as implemented for practical laboratory experiments consists of six distinct steps, Fig. 3.1. In general order these steps are CD equalization, polarization demultiplexing, symbol timing recovery, carrier phase recovery, least-mean square (LMS) equalization, and symbol detection. We also perform sampling skew removal immediately after digitization and before CD equalization. This first step removes the sub-sample-rate digitization offset between the four sampled channels using a high-precision fractionally-spaced filter.

*3.1.1. Chromatic Dispersion Estimation and Equalization*

After digitization and sampling skew removal the DSP must first compensate for CD. The transfer function

$$H_{CD}(\omega) = \exp\{\pm j\lambda_0^2 DL\omega^2/4\pi c\} \tag{3.2}$$

is implemented which contains the precise quadratic phase dependence of second-order dispersion described in (2.26). The value $DL$ (s/m) is the total accumulated dispersion that the filter should compensate and the sign of the exponential should be chosen opposite the dispersion evolution of the channel (usually negative). The transfer function is first constructed in the frequency domain as shown in (3.2).

Figure 3.2 demonstrates the middle 10 GHz of phase of a typical CD filter for long-haul communication. The filter can be converted to a time-domain filter with an inverse fast Fourier Transform (IFFT). Accordingly, CD compensation can be performed either in the frequency or time domain (the frequency-domain implementation is usually more efficient). Notice the quadratic character of the phase for increasing frequency; the phase must be first unwrapped before being applied to the received signal. This filter, Fig. 3.2, compensates for ~32,000 ps/nm of dispersion across a typical 50 GHz channel.

CD estimation is a technique to determine the total residual dispersion in a blind fashion.

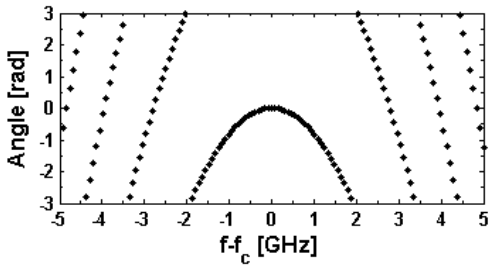


Figure 3.2. Center 10 GHz of the phase of a chromatic dispersion filter that compensates for >32k ps/nm of dispersion (~1600 km).

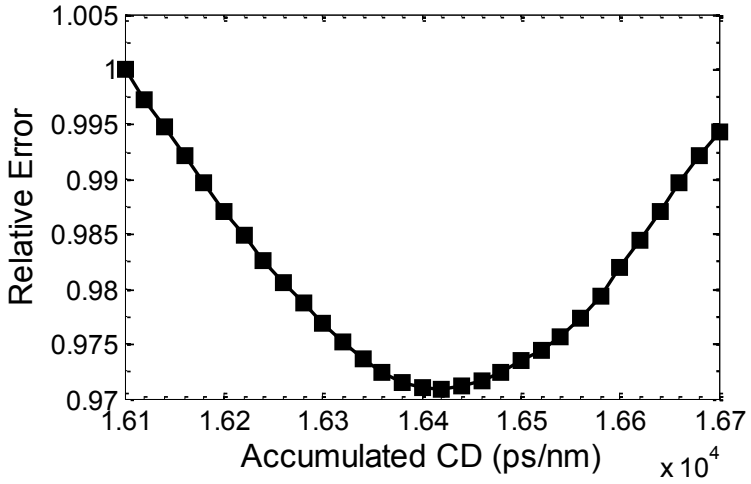


Figure 3.3. Minimization of error metric (3.3) after reduction in dispersion step size to determine the most appropriate $DL$ value for $H_{CD}$.

Typically, and as exampled in Fig. 3.2, the amount of dispersion is known and the CD equalization filter can be constructed accordingly. However, CD estimation provides a means to determine the best amount of CD to compensate, which may not be exactly the total amount accrued. We estimate CD by iteratively compensating for a varying amount of dispersion with a wide step size [56]. For each step of dispersion the error metric

$$\mathrm{e} = \sum_k (||u_k|^2 - \mathrm{E}\{|u_k|^2\}| + ||v_k|^2 - \mathrm{E}\{|v_k|^2\}|) \tag{3.3}$$

is calculated, where $u_k = h_{\mathrm{CD,est}} * x_k$ and $v_k = h_{\mathrm{CD,est}} * y_k$. The minimum error occurs when the square amplitude deviation from the mean is the least. That is, when the signal has the lowest peak-to-average power ratio. Once a rough estimate of the CD has been located, the algorithm reduces the CD step size and iteratively locates the local minimum using the same error metric (3.3), Fig. 3.3.

### *3.1.2. Polarization Demultiplexing*

Polarization demultiplexing in a single mode fiber application is a 2x2 MIMO process governed by the Jones matrix that describes the fiber and the alignments of the transmitter and

receiver E-fields. For dual-polarization fiber transmission, the MIMO equalizer is arranged in a "butterfly" structure, Fig. 3.1. The equalizer adapts four sets of complex coefficients, bridging each of the possible paths from X and Y input to X and Y output, to jointly minimize the resulting error in the output. Convergence is assured to avoid false recovery at both X and Y outputs when constrained by the relationship

$$\begin{bmatrix} \bar{h}_{xx} & \bar{h}_{xy} \\ \bar{h}_{yx} & \bar{h}_{yy} \end{bmatrix} = \begin{bmatrix} \bar{u} & \bar{v} \\ -\bar{v}^* & \bar{u}^* \end{bmatrix}, \tag{3.4}$$

where $u$ and $v$ are complex-valued vectors with one element per equalizer tap. The complex conjugate operation also implies a time reversal of the vectors.

Though derivation is omitted for brevity (available here [57, 58]), the constant modulus algorithm (CMA) will adapt a bank of equalizers to minimize inter-symbol interference (ISI) in a dispersive fiber environment given that

$$E\{a_n^2\} = 0 \tag{3.5}$$

is satisfied, that there exists at least as many independent receiver polarization modes as transmitter modes, and that there exists a matrix with non-zero determinant that describes the channel. The first two requirements are met by proper choice of modulation format (PDM-QPSK) and use of a dual-pol receiver. The latter is met by the fact that fiber transmission can be modeled by the Jones matrix [7], and the process of polarization demultiplexing may be expressed as the receiver's estimate of the inverse Jones matrix based on observation of the input signal.

The symmetry (3.4) is guaranteed for all complex-valued transmissions that have 90° phase ambiguity (i.e. the constellation is identical when rotated by 90°), to which we will refer as rotational symmetry. Other asymmetric constellations will also converge, provided they conform with (3.5). The CMA error criterion uses the complex-valued error calculation

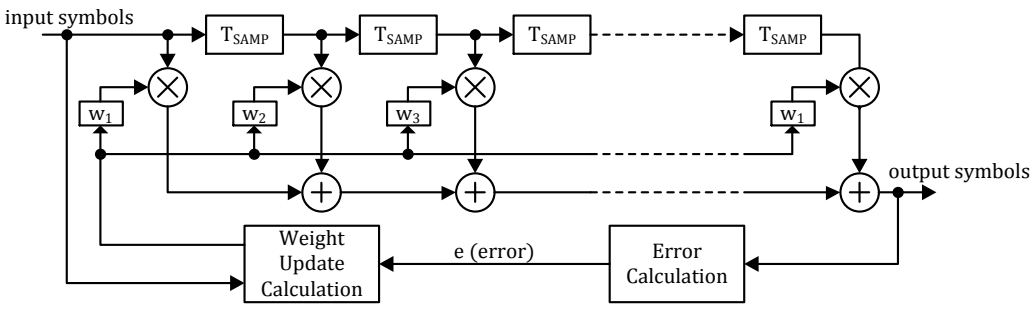


Figure 3.4. Block diagram of a general, sample-rate-spaced digital equalizer. One instance of this equalizer the CMA update rule is implemented for each of $h_{xx}$, $h_{xy}$, $h_{yx}$, and $h_{yy}$ to perform polarization demultiplexing.

$$e = y(R - |y|^2) \tag{3.6}$$

where $y$ is the output symbol and

$$R = \frac{E\{|a_n|^4\}}{E\{|a_n|^2\}}. \tag{3.7}$$

$R$ is a real, positive radial constant to which the equalizer attempts to constrain the output. Using the classical gradient descent approach, the error calculation vector assists the equalizer in finding and maintaining coefficients to achieve stable operation at an ISI minimum [57]. Specifically, the update rule for CMA is [59]

$$h_k = h_k + \mu e x_k^*, \tag{3.8}$$

where $h_k$ are the filter taps, $e$ is the error given in (3.6), $x_k$ are the input symbols, and $\mu$ is the step size. Equation (3.8) is calculated for each of $h_{xx}$, $h_{xy}$, $h_{yx}$, and $h_{yy}$ and the criteria (3.4) is subsequently enforced. A block diagram of a CMA equalizer is shown in Fig. 3.4.

In Fig. 3.1 we show the pol-demux operating asynchronously, that is, before timing recovery. Polarization demultiplexing can also be performed synchronously (after timing recovery) with no penalty [60]. However, the asynchronous mode allows the equalizer to accept different forms of modulation that do not conform to the model of recovering timing before separating the polarization modes. The CMA error signal is generated in attempt to reduce the modulated constellation to a unit circle on the I-Q plane. For this reason, the CMA algorithm is

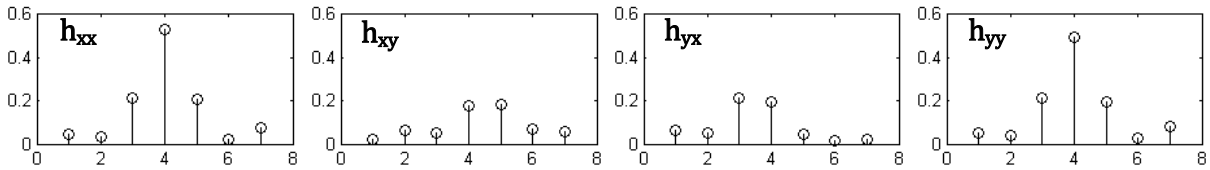

Figure 3.5. Magnitude of the pol demux filter weights after CMA convergence for example laboratory data. The tap labeled "four" is the center of seven taps. Note that $h_{xy}$ and $h_{yx}$ are mirror images about the center tap as constrained by the Jones matrix (3.4).

capable of equalizing any rotationally symmetric modulation format, including QPSK, OQPSK, CPM, and QAM [60]. When used for blind source separation in a MIMO channel, CMA is capable of separating a combination of these modulation formats, provided there are at least as many diversity receivers as there are transmitters [60]. In fact, the CMA algorithm in this context has no explicit requirement to operate at a multiple of the symbol rate or to be synchronized to the transmitter in any other way. We example the post-convergence weights of an asynchronously-operated, seven-tap, CMA-based pol-demux equalizer in Fig. 3.5 for PDM-QPSK.

### *3.1.3. Symbol Timing Recovery*

To recover the symbol timing phase we implement the non-data-aided (NDA) feedforward digital filter and square method [61]. This block of the processing flow estimates the symbol time on each polarization independently by first squaring the symbols and then centering on the maximum eye opening. That is, the timing estimate returns

$$\hat{\tau} = -\frac{1}{2\pi}\arg\left\{\sum_{m=0}^{LN-1}|x_{m+1}|^2 \exp\left(-\frac{j2\pi m}{N}\right)\right\}, \tag{3.9}$$

which is the normalized phase between $-1/2$ and ½. In (3.9), $x_m$ are the message symbols, $L$ is the number of symbol per frame, and $N$ is the number of samples per symbol. The magnitude square operation is proportional to the instantaneous power and maximum at the maximum eye opening since QPSK will, with high probability, pass through regions of low power. In general,

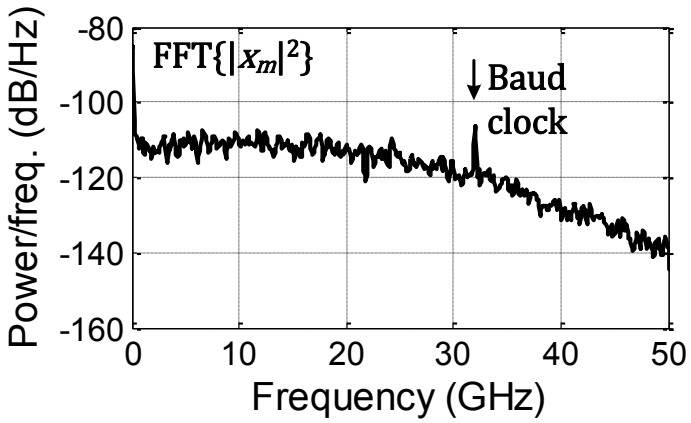


Figure 3.6. Frequency-domain representation of timing phase extraction of a 32 Gbaud PDM-QPSK signal. The black curve is the FFT of the $N = 20$ oversample of the message symbols $x_m$. The spectral peak at 32 GHz is the baud clock.

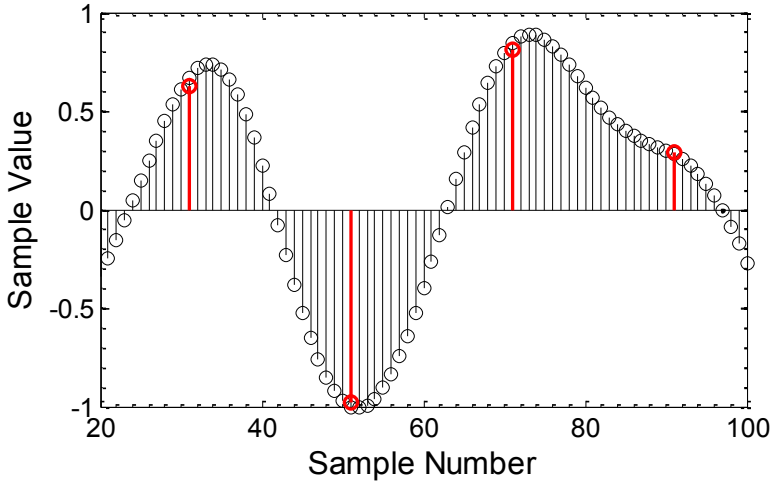


Figure 3.7. Time-domain representation of timing phase extraction of a 32 Gbaud PDM-QPSK signal. The black samples are the $N = 20$ oversample of the message symbols $x_m$. The red stems are the extracted timing phase as computed by (3.9).

we upsample to $N = 20$ samples per symbol and employ a timing recovery frame of $L = 1000$ symbols to ensure an accurate timing phase estimate.

### *3.1.4. Carrier Phase Estimation*

Carrier phase recovery is the process of estimating the phase distortion of the received signal induced by the time-varying, random frequency offset between the carrier and LO lasers

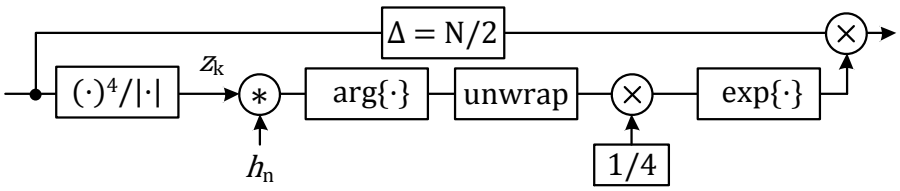


Figure 3.8. Non-data-aided, feedforward, power-of-four carrier recovery for QPSK. Often called the Viterbi-Viterbi algorithm [62].

or by the fiber nonlinearities. The essence of the problem can be mathematically described by the equation

$$y_k = x_k \exp\{j\theta_k\} + n_k, \tag{3.10}$$

where $x_k$ is the $k^{\text{th}}$ transmit symbol, $y_k$ is the $k^{\text{th}}$ receive symbol, $\theta_k$ is the phase distortion on the $k^{\text{th}}$ symbol, and $n_k$ is the additive noise.

We perform carrier recovery via the feedforward Viterbi-Viterbi algorithm [62], Fig. 3.8. The first step in the Viterbi-Viterbi carrier phase recovery algorithm for $m$-PSK is to raise the detected symbols to the power of $m$ to remove the modulation. For QPSK we have $m = 4$ and therefore

$$z_k = y_k^4 = \exp\{j4\phi_k\} + n_k'. \tag{3.11}$$

The digital filter $h_n$ should be chosen to best extract a phase estimate given the noise statistics of the channel. We implement the filter in one of three ways: (1) identical taps [62], (2) minimum mean-square error (MMSE) computed taps [63], or (3) Wiener filter taps [64]. The first filter extracts the phase estimate based on an average of $N$ consecutive symbols. That is, it applies an $N$-tap "sliding window" filter with equal weights (normalized to the number of taps) to the fourth-power symbols, whose phase is then unwrapped, divided by four, and applied to the original samples after a fixed delay of $N/2$.

The second method computes taps to attempt to strike a balance exploiting phase correlation and noise averaging. We utilize an MMSE approach to minimize the cost function of

the difference between the desired phase $\exp\{j4\phi_{k-\Delta}\}$ and phase after filtering $\exp\{j4\hat{\phi}_k\}$ (where $\Delta = N/2$ is some fixed delay determined by the length of the filter)

$$E\left[\left|\exp\{j4\hat{\phi}_k\} - \exp\{j4\phi_{k-\Delta}\}\right|^2\right] = E[|\boldsymbol{h}^H \boldsymbol{z}_k - \exp\{j4\phi_{k-\Delta}\}|^2]. \tag{3.12}$$

Minimizing this cost function we have

$$E[\boldsymbol{z}_k \boldsymbol{z}_k^H]\boldsymbol{h} = E[\boldsymbol{z}_k \exp\{j4\phi_{k-\Delta}\}]. \tag{3.13}$$

which requires estimation of the autocorrelation function of $z_k$ to solve. From equation (3.11), the autocorrelation at lag $l$ is $r_z(l) = r_\theta(l) + \sigma_m^2\delta(l)$, where $r_z(l) = E[z_k z_{k-l}^*]$ and $r_\phi(l) = E[\exp\{j4\phi_k\}\exp\{j4\phi_{k-l}\}]$. Since $r_\phi(0) = 1$ then $r_z(0) = 1 + \sigma_m^2$, and thus the desired autocorrelation function is

$$r_z(l) = (1 + \sigma_m^2)E[z_k z_{k-l}^*]. \tag{3.14}$$

From [8], the noise variance can be computed as

$$\sigma_m^2 = \sum_{p=1}^{4} \frac{p!}{\gamma^p}\binom{4}{p}^p, \tag{3.15}$$

where $\gamma$ is the SNR per symbol.

The Wiener filter implementation is the optimum filter for laser phase noise dominated systems [64]. In the time domain, Wiener filter taps can be computed as

$$w_n = \begin{cases} \frac{\alpha r}{1-\alpha^2}\alpha^n, & n \geq 0 \\ \frac{\alpha r}{1-\alpha^2}\alpha^{-n}, & n < 0 \end{cases}, \tag{3.16}$$

where $N$ is the filter length,

$$\alpha = \left(1 + \frac{r}{2}\right) - \sqrt{\left(1 + \frac{r}{2}\right)^2 - 1}, \tag{3.17}$$

and $r = \sigma_p^2/\sigma_n^2$ the ratio of phase noise variance to additive noise variance. However, most systems are not laser linewidth dominated and therefore the Wiener filter is nearly always

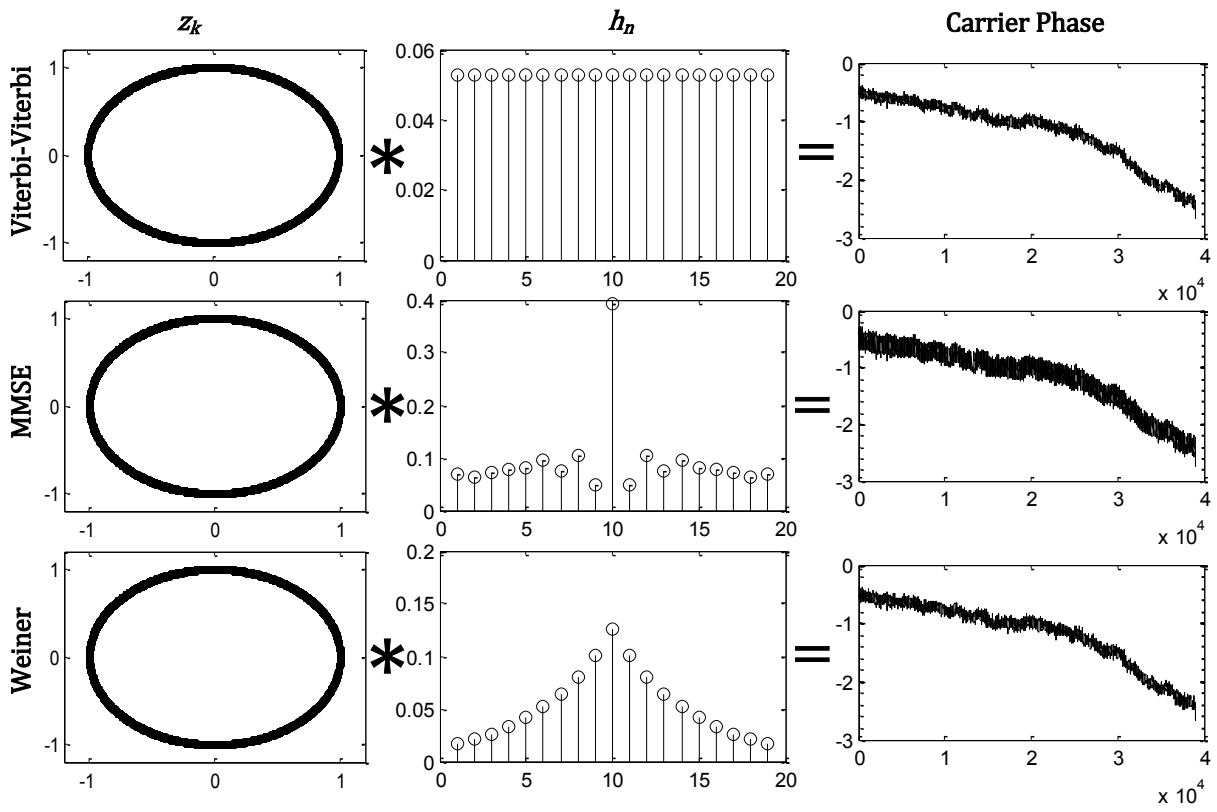


Figure 3.9. Cartoon exampling the extraction of carrier phase from the pour-of-four symbols using a sliding-window filter (top row), MMSE-computed filter (middle row), and a Weiner filter (bottom row).

suboptimum for practical systems. The filter was investigated and included here for completeness, but it is not used in any experimental work that follows in later sections.

### *3.1.5. LMS Equalization*

The LMS equalizer is a classical adaptive filter that can also be considered a stochastic gradient algorithm; its derivation is covered thoroughly in the literature [53, 63]. Here, each polarization is independently processed through a 15-tap, T-spaced LMS equalizer. No further cross-polarization interference cancellation is attempted (i.e. this filter is not arranged in a "butterfly" structure). The purpose of this filter is to remove any residual CD and ISI that the channel imposes, and to output a single sample per symbol for detection.

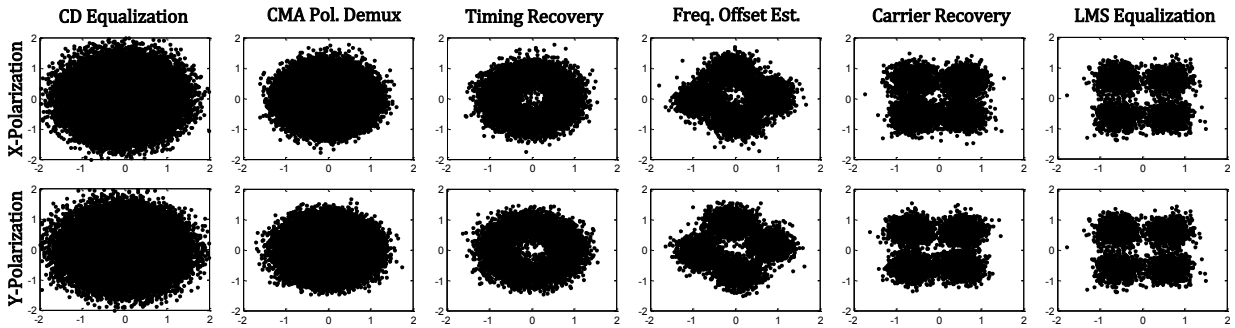

Figure 3.10. Constellation diagrams of a laboratory-captured PDM-QPSK signal at the output of each step of the DSP described in the preceding sections (3.1.1-3.1.5) and in Fig. 3.1.

*3.1.6. Summary of PDM-QPSK DSP*

We summarize the DSP described in §3.1.1-3.1.5 visually in Fig. 3.10. The output of each processing step is represented in a constellation diagram for each polarization. After CD equalization the samples appear as a "blob"; there is no immediately recognizable modulation scheme. The polarization demultiplexing step separates the X- and Y-polarizations by enforcing the constant-modulus and Jones matrix criteria. Next, the timing phase is extracted and the constellation takes on a doughnut shape (since phase has not been recovered). Frequency offset estimation is essentially a one-shot phase estimate that removes the linear component of the phase distortion of the message symbols. Once a phase estimate is made to extract the time-varying phase evolution of the data symbols the QPSK constellation appears upright. Finally, the LMS equalization tightens each quadrant of the constellation in preparation for slicing and BER evaluation.

The back-to-back BER vs. optical signal-to-noise ratio (OSNR) performance of both single- and dual-pol 28 Gbaud QPSK appears in Fig. 3.11 with either direct (interferometric) or coherent detection. The black dashed line labeled "v2", Fig. 3.11, demonstrates the improvements made to PDM-QPSK performance as the demodulation code was refined over several years (the DSP described contain in this dissertation reflect those refinements). Note that PDM-QPSK achieves a back-to-back BER of $10^{-3}$ at an OSNR of 14 dB (with a 3 dB advantage

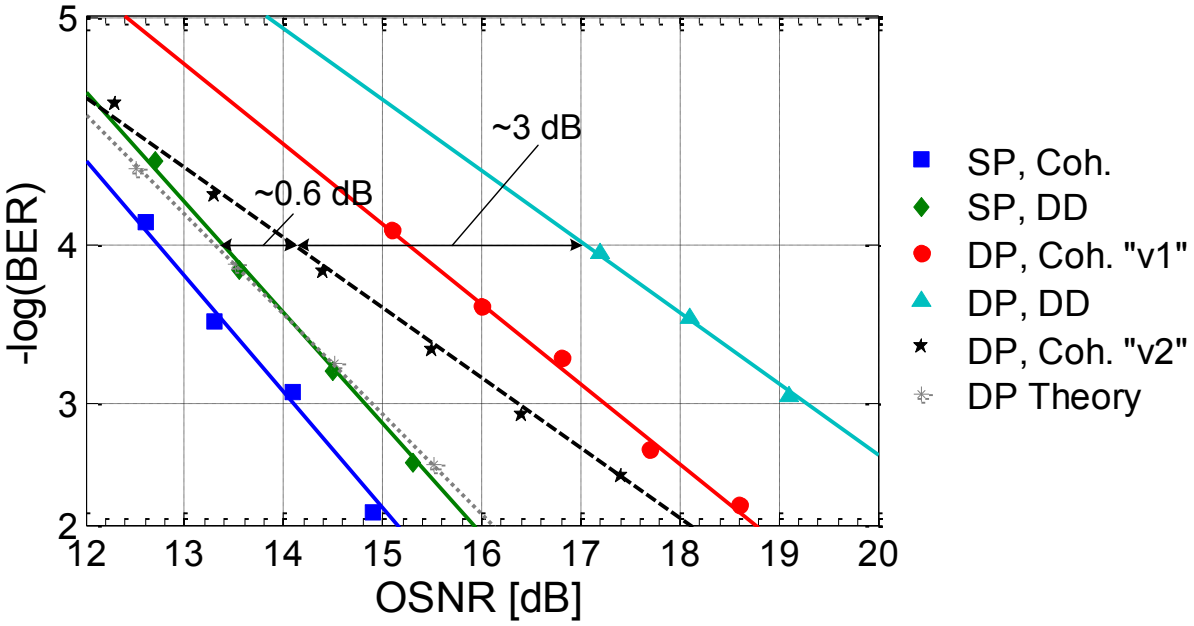


Figure 3.11. Laboratory BER performance of single- (SP) and dual-polarization (DP) 28 Gbaud QPSK with direct (DD) and coherent detection (Coh.) schemes in a back-to-back configuration. The black dashed line demonstrates improved code performance using the DSP described in this work which contains refinements and corrections over the initial version of the DSP (red line).

over DD) which is consequently the target OSNR for most transmission systems based on QPSK. The gray dotted line marks the theoretical lower limit of 28 Gbaud PDM-QPSK BER vs. OSNR performance in an AWGN channel.

### 3.2. DSP for PDM-16QAM

The signal processing flow for PDM-16QAM changes in two major ways compared to the processing for PDM-QPSK. Most importantly, we adopt a more robust polarization demultiplexing algorithm based on Independent Component Analysis (ICA). This algorithm requires precise symbol timing, necessitating a reversal of the timing recovery and pol-demux steps. The timing recovery algorithm, however, remains unchanged. Second, we update the carrier recovery algorithm to better adapt for 16QAM. The Viterbi-Viterbi algorithm described in §3.1.4 works for 16 QAM, although it is suboptimum; the power-of-four operation does not

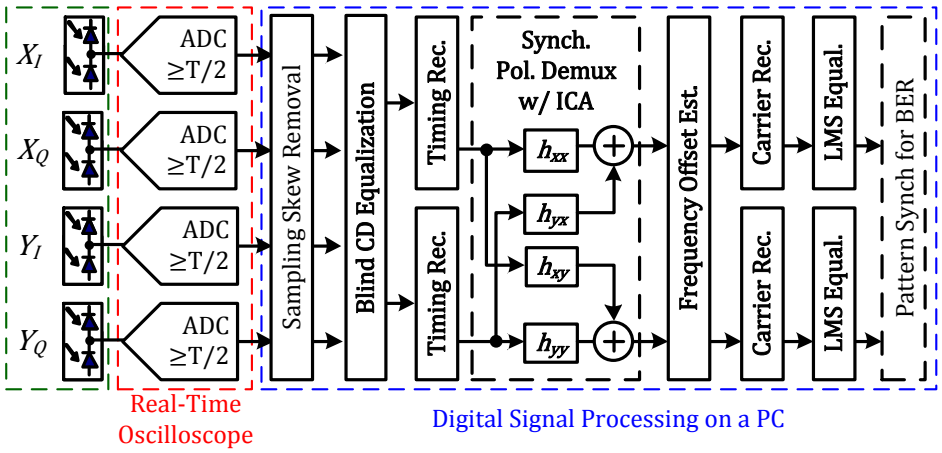


Figure 3.12. General signal processing flow for PDM-16QAM. Note timing recovery is performed before polarization demultiplexing.

completely remove the modulation as it does for QPSK. Therefore we have implemented a decision-directed phase integrator for better phase tracking and more robust performance.

### *3.2.1. Polarization Demultiplexing with Independent Component Analysis*

As explained in the previous paragraphs, CMA does not adapt optimally for modulation formats that are not constrained to a constant modulus. An alternate method of separating polarization is ICA. ICA is based on the understanding that the two orthogonal polarization modes are statistically independent and uncorrelated. The principal of ICA source separation is the central limit theorem: the mixture of non-Gaussian signals tends to Gaussian. Therefore ICA attempts to maximize the "non-Gaussianity" (entropy) of the signal. The advantage to this approach is that an ICA equalizer can separate any two signal sources regardless of modulation format provided that they are each, in general, not Gaussian-distributed [66].

The ICA equalizer is configured in an identical fashion to the butterfly structure of the CMA-based equalizer, Fig. 3.12. The tap update rule, however, is based on the Natural Gradient method. The Natural Gradient method possesses the equivariance property; it converges

asymptotically based on the stochastic properties of the source signals and regardless of the channel (or mixing) description [66]. Let

$$\boldsymbol{S}(k) = \begin{bmatrix} S_1(k) \\ S_2(k) \end{bmatrix} \tag{3.18}$$

be two statistically independent, non-Gaussian signals. The convolutive mixture of the two signals is

$$\boldsymbol{x}(k) = \begin{bmatrix} x_1(k) \\ x_2(k) \end{bmatrix} = \sum_{p=0}^{L} \boldsymbol{H}_p \boldsymbol{s}(k-p), \tag{3.19}$$

where $\boldsymbol{H}_p$ is the $2x2$ channel matrix at the $p^{th}$ tap and $L$ is the filter length. The Natural Gradient method can be used to iteratively compute the tap weights of $\boldsymbol{W}_p$, the compensating matrix at the $p^{th}$ tap.

First, initialize the center taps of the compensating filter to one, $\boldsymbol{W}_{L/2}(0) = \boldsymbol{I}$. Next, apply the compensating filter

$$\boldsymbol{y}(k) = \sum_{p=0}^{L} \boldsymbol{W}_p(k) \boldsymbol{x}(k-p). \tag{3.20}$$

Third, compute the reverse filter output

$$\boldsymbol{v}(k) = \sum_{q=0}^{L} \boldsymbol{W}_{L-q}^{H}(k) \boldsymbol{y}(k-q). \tag{3.21}$$

And finally update the filter weights with the rule

$$\boldsymbol{W}_p(k+1) = \boldsymbol{W}_p(k) + \mu \left( \boldsymbol{W}_p(k) - \boldsymbol{g}\big(\boldsymbol{y}(k-L)\big) + \boldsymbol{v}^H(k-p) \right). \tag{3.22}$$

In (3.22), $\boldsymbol{g}(y) = y/|y|$ is the chosen nonlinear function for sub-Gaussian signals [66].

For the case in optical systems where the two convolved signals are the orthogonal polarization modes, the polarization demultiplexing equalizer is required to compensate for PMD. While a single-tap ICA equalizer can asynchronously separate sampled data, to compensate for polarization mode dispersion (PMD) the equalizer needs enough (more than one) taps to cover the time walk-off of the polarization modes. Thus timing recovery must be

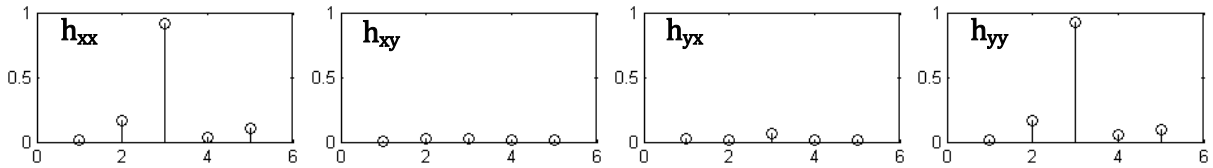

Figure 3.13. Magnitude of the pol-demux filter weights after ICA convergence for example laboratory data. The tap labeled "three" is the center of 5 taps. Note that $h_{xy}$ and $h_{yx}$ are very small, indicating that this data had polarization largely aligned with the receiver X and Y ports.

performed prior to the polarization mode separation via ICA. The post-convergence weights of a 5-tap, ICA-evolved polarization demultiplexing filter appear in Fig. 3.13 for an experimental 32 Gbaud PDM-16QAM signal in a back-to-back configuration.

### *3.2.2. Carrier Recovery for 16QAM*

The carrier phase recovery algorithm used for 16 QAM transmission is derived from the "stop-and-go" decision-directed algorithm described in [67] and in [68], Fig. 3.14. Also called a "phase integrator", the algorithm employs a decision-directed recovery loop to estimate the carrier phase with the rule

$$\theta_{k+1} = \theta_k - \mu_\theta \mathrm{Im}\{z_k e_k^*\}, \tag{3.23}$$

where $\theta_k$ is the phase estimate, $z_k$ are the message symbols, $\mu_\theta$ is the step size parameter, and

$$e_k = z_k - a_k \tag{3.24}$$

is the error signal. Typically $\mu_\theta$ is chosen between 0.01 and 0.05 for our systems.

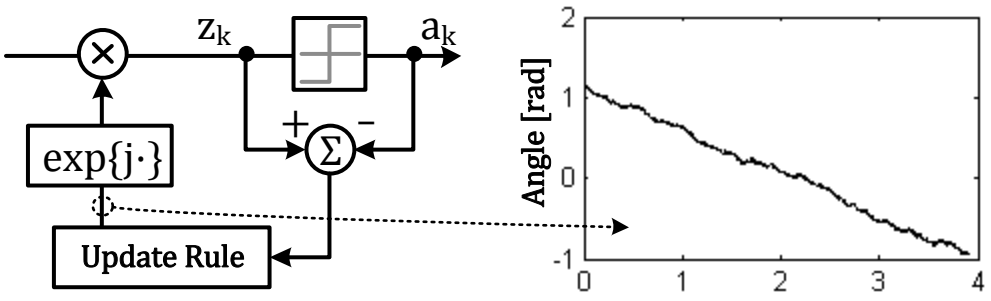

Figure 3.14. Block diagram of the data-aided integrator for carrier phase recovery for 16QAM.

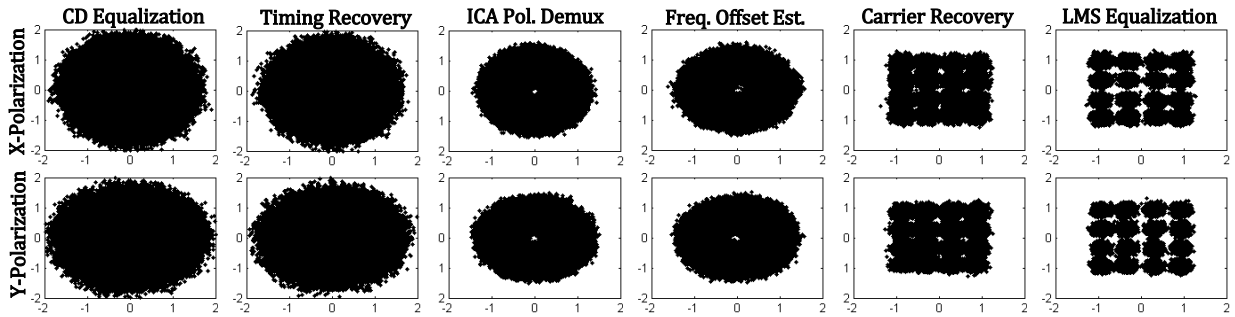

Figure 3.15. Constellation diagrams of a laboratory-captured 32 GBaud PDM-16QAM signal. Each pair of diagrams shows the output of each step of the DSP.

*3.2.3. Summary of Processing Flow*

We summarize the DSP described in §3.2.1-3.2.2 visually in Fig. 3.15. The output of each processing step is represented in a constellation diagram for each polarization. After CD equalization the samples appear as a "blob"; there is no immediately recognizable modulation scheme. The timing phase is extracted and the constellation retains its "blob" shape since the polarizations have not been deconvolved. Next, the polarization demultiplexing step separates the X- and Y-polarizations by enforcing the Natural Gradient criteria and the constellation becomes a disk with constrained amplitude. After the frequency offset has been estimated the to remove the linear component of the phase distortion message symbols display three distinct rings. Once a phase estimate is made to extract the time-varying phase evolution of the data symbols the 16QAM constellation appears upright. Finally, the LMS equalizer tightens the constellation about the nominal symbol positions in preparation for slicing and BER evaluation.

The back-to-back BER vs. OSNR performance of a PDM-16-QAM signal appears in Fig. 3.16 for two different baud rates. At BER rates $>10^{-3}$ the DSP is able to recover the signals to within ~2 dB of theoretical limits. However, the experimental signal demonstrate an error floor for increasing OSNR at BERs of $\sim10^{-4}$ and $\sim10^{-5}$ for 32 and 16 Gbaud, respecitively. These errors floor arise due to the implementation penalty of the laboratory setup (described in more detail in §9).

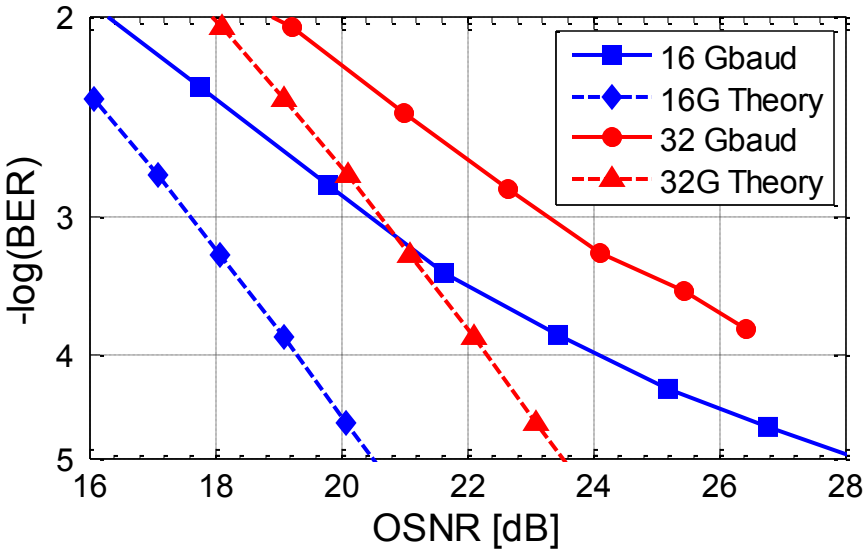


Figure 3.16. Back-to-back BER vs. OSNR performance of 16 Gbaud and 32 Gbaud PDM-16-QAM. The error floors that appear at $10^{-4}$ and $10^{-5}$ for 32 and 16 Gbaud, respectively, are due to the laboratory implementation penalty.

# CHAPTER 4

# MINIMIZING NONLINEAR TRANSMISSION EFFECTS

## 4.1 Dispersion Map Optimization for DQPSK

DQPSK is a promising modulation format for next-generation high-speed fiber optic communication systems due to its narrow spectral width, tolerance to CD and PMD [74]. Additionally, RZ pulse carving increases long-haul SNR margin. Initial deployments of DQPSK may occur on network infrastructure with OOK channels, or in banks adjacent to other DQPSK channels at the same line rate. Existing networks are a patchwork of different fiber types, span lengths, and dispersion maps, making it important to evaluate and quantify DQPSK performance in a hybrid network configuration with adjacent OOK channels.

Nonlinear phenomena like SPM, XPM, and FWM are the major capacity-limiting effects in optical fiber. Phase-based modulation formats are particularly sensitive to phase distortions caused by SPM and XPM. Recent work has shown that careful dispersion management can effectively limit transmission penalties caused by nonlinear impairments in DQPSK systems [75-78]. Here we examine the effect of dispersion map on 28 Gbaud RZ-DQPSK for both single and dual-polarization formats with either 12 Gb/s OOK or identical QPSK side channels.

We adjust the dispersion map of a point to point optical link while keeping the loss per span fixed while utilizing either direct detection or a coherent receiver for detection. For each dispersion map, we extract the required OSNR to achieve a BER of $10^{-3}$, under the assumption that FEC can yield gains that achieve error-free transmission. This metric allows demonstration

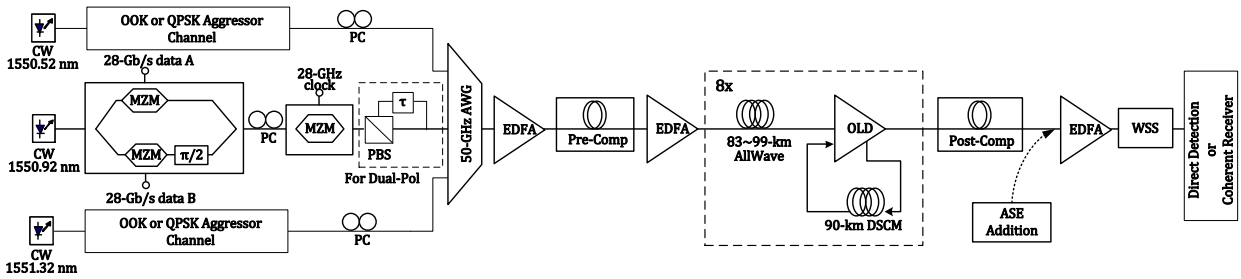


Figure 4.1. Experimental setup of hybrid system incorporating eight identical spans.

of an optimization rule for DQPSK with OOK side channels that we extend to encompass PDM-QPSK with coherent detection.

The experimental setup, Fig. 4.1, is configured in three different ways.

1. Two 12 Gb/s NRZ-OOK side channels are placed in the two adjacent 50 GHz channel around a center 28 Gbaud single-pol RZ-DQPSK (56 Gb/s) channel creating a hybrid network. The three channels are co-polarized for worst-case analysis and are multiplexed using an AWG. After transmission, the DQPSK is selected with a bandpass filter (BPF) and interferometrically detected (see Fig. 2.5b).
2. The interferometric detector is replaced with a coherent receiver to test both single and dual-polarization QPSK formats of the center channel.
3. The 12 Gb/s OOK side channels are replaced with 28 Gbaud PDM-QPSK channels identical to the center one and detected in a coherent receiver.

The point to point optical link consists of eight identical spans of AllWave (G.652) fiber and an ADVA Optical Line Driver (OLD). Each span also contains a dispersion compensating module (DCM) providing negative dispersion to compensate 90 km of AllWave fiber. Utilizing a set of tuning spools, we are able to adjust the residual dispersion per span (RDPS) by changing the length of each span while employing the same DCM. We keep the per-span loss constant at 22 dB with internal variable optical attenuators (VOA) in the OLDs to ensure no loss-dependent

Table 4.1. Experimental values for dispersion map optimization experiments.

| PARAMETER | TESTED VALUES |
|---|---|
| Span Length [km] | 83, 86, 90, 93, 96, 99 |
| RDPS [ps/nm] | -112, -68, 0, +51, +102, +153 |
| Pre-Compensation [ps/nm] | -170, -680, -1020 |
| Launch Power [dBm] | -2, 0, +2, +4 |

effects. Additionally, the link uses a pre-compensation module to provide negative dispersion before launching the channels into the spans. At the end of the link, two tunable fiber Bragg gratings (TFBG) compensate for any net residual dispersion after transmission. The pre-compensation modules are tunable in 10 km increments (-170 ps/nm) and the TFBGs are tunable in ±10 ps/nm increments. This setup affords control of several variables of practical interest: received OSNR, RDPS, launch power, and pre-compensation.

For all experiments employing setups (1) and (2), we fix the launch power of the 12 Gb/s OOK side channels at +0 dBm (typical of deployed systems) while we vary the launch power of the DQPSK channel from -2 to +4 dBm for each dispersion map. We control the RDPS from -119 ps/nm to +153 ps/nm, noting that regional and long haul DWDM networks operating at 40 Gb/s and 10 Gb/s typically range from +50 to +150 ps/nm RDPS [78]. For each RDPS value, we analyze three different pre-compensation values: -170, -680, and -1020 ps/nm, corresponding to 10, 40, and 60 km of pre-compensation, respectively (where 20 to 40 km might be common for 10 Gb/s deployed systems). Table 4.1 summarizes the experimental parameters. The span lengths and RDPS values correspond (i.e. 83 km spans = -112 ps/nm RDPS) while the pre-compensation and launch power values are varied parameters for each dispersion map.

Figure 9 shows the required OSNR for BER = $10^{-3}$ of 56 Gb/s RZ-DQPSK with (a) -170 ps/nm, (b) -680 ps/nm, and (c) -1020 ps/nm of pre-compensation. With -170 ps/nm, Fig. 9(a), good robust performance is observed over the range of RDPS studied. All DQPSK

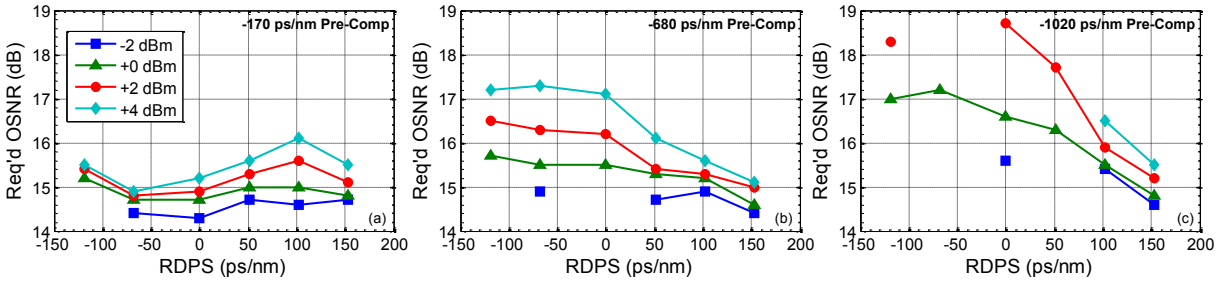


Figure 4.2. OSNR to achieve BER of $10^{-3}$ vs. RDPS for 56 Gb/s RZ-DQPSK with (a) -170 ps/nm (b) -680 ps/nm and (c) -1020 ps/nm of pre-comp. The legend indicates the center QPSK channel launch power.

configurations examined yield a BER < $10^{-3}$ for OSNR > 16 dB. The absolute best link performance occurs with -68 ps/nm of RDPS and a required OSNR of 15 dB. In contrast, for both -680 ps/nm and -1020 ps/nm of pre-compensation, the optimum RDPS was +153 ps/nm. The improvement in BER performance at larger-magnitude RDPS can be understood from the fact that larger RDPS provides a more significant walk-off in group delay between the DQPSK and OOK channels, increasing the DQPSK channel's tolerance to XPM effects. We find for +2 dBm launch power that a near-optimum map includes -170 ps/nm pre-comp and -68 ps/nm RDPS. This is similar to previously-reported results [77] determined through a global numerical optimization for 28 Gbaud DQPSK, which found -150 ps/nm of pre-compensation and -10 ps/nm of RDPS optimum.

Because single-pol DQPSK performs relatively well with 10 km of pre-compensation regardless of the chosen RDPS, we chose the +0 and +153 ps/nm dispersion maps to compare performance of coherent single and dual-pol QPSK (experimental setups two and three). Figure 4.3 shows that moving to a coherent receiver offers a 2 dB advantage with single-pol RZ-DQPSK. Additionally, we see that dual-pol performance nearly matches that of single-pol with a coherent receiver. When we move to QPSK adjacent aggressor channels, Fig. 4.4, the 90 km per span dispersion map (0 ps/nm RDPS) enables launch powers in excess of 6 dBm for single-pol QPSK while still maintaining BER less that $10^{-3}$. Dual-pol QPSK achieves 3.5 dBm launch

power before falling below $10^{-3}$ BER. In both cases, the 0 ps/nm RDPS dispersion offers > 2 dB performance improvement compared to the +153 ps/nm dispersion map.

Using interferometrically-detected, single-pol, 28-GBaud RZ-DQPSK with adjacent 12-Gb/s NRZ-OOK aggressor channels, an inline compensation scheme with RDPS of +153 ps/nm is insensitive to pre-comp between -10 to -60 km worth of AllWave, but may degrade rapidly with deviations from the target RDPS. The most robust map uses the smaller pre-comp of -170 ps/nm and is far less sensitive to variation in the in-line compensation. Coherent detection of single- and dual-pol QPSK indicates significant dependence on dispersion map, making it is advisable to consider the performance of future 100G overlays when designing 10G long haul dispersion maps.

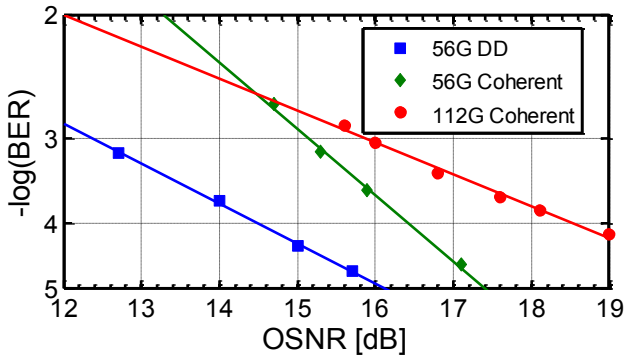


Figure 4.3. Coherent QPSK results compared to direction detection after 8 spans transmission with +153 ps/nm RDPS and 12 Gb/s OOK neighboring channels. Per channel launch power is +0 dBm.

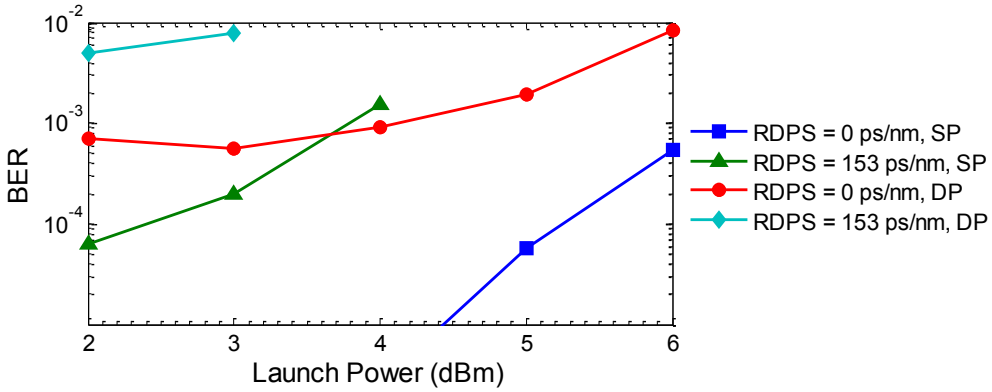


Figure 4.4. Coherent QPSK results in the presence of other QPSK channels for RDPS of 0 ps/nm (90 km spans) and 153 ps/nm (99 km spans). SP = single-pol, DP = dual-pol.

## 4.2 OQPSK as an Alternative to QPSK

Offset quadrature phase shift keying (OQPSK) is a variation of the more commonly used QPSK modulation format in which the in-phase and quadrature binary signals are shifted by half a symbol period with respect to each other. The shift ensures that the field transition of either I or Q between zero and one occurs during the maximum eye opening of the other component. Consequently the total electric field is never zero. In contrast, QPSK experiences zero amplitude for every 180 degree symbol transition (1/4 of all symbol transitions). This feature of OQPSK has been exploited in wireless systems by using lower-cost and higher-efficiency amplifiers. Because OQPSK has reduced intensity variations compared to QPSK it may limit the nonlinear penalties accrued because of nonlinear refraction (see §2.2).

The OQPSK signal can be defined as

$$s(t) = \sum_k \left[ g(t - kT_s) a_{I,k} \cos(2\pi f_c t) - g\left(t - kT_s - \frac{T_s}{2}\right) a_{Q,k} \sin(2\pi f_c t) \right], \qquad (4.1)$$

where $g(t)$ is the pulse shape, $T_s$ is the symbol period, and $a_{I,k}$ and $a_{Q,k}$ are the data sequence symbols of the in-phase and quadrature components of the signal. NRZ-OQPSK can be readily implemented in the optical domain with the standard I/Q modulator (Fig. 2.2) by inserting a $T_s/2$ delay between the I and Q components of the binary drive signals. However, RZ signaling can only be accomplished by carving the I and Q signals independently which is not practical given the integrated nature of the I/Q modulator.

OQPSK requires coherent detection; no equivalent direct-detection structure like Fig. 2.5b for QPSK is practically implementable. Once detected and digitized, the DSP flow for OQPSK is largely similar to QPSK. The exception is that OQPSK *requires* the polarization demux step be performed prior to a modified timing and carrier recovery algorithm. OQPSK

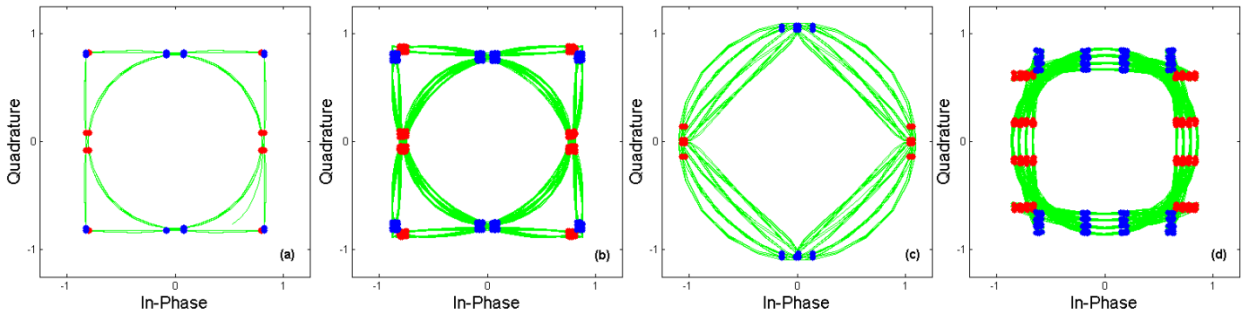


Figure 4.5. Constellation diagrams showing symbol transitions of (a) NRZ-OQPSK, (b) filtered NRZ-OQPSK, (c) RZ-OQPSK, and (d) filtered RZ-OQPSK. Filter parameters: order 3.5 super Gaussian, Eqn. (2.29).

symbol timing $\hat{\tau}$ and carrier phase $\hat{\theta}$ can be estimated by the joint, feedforward, non-data-aided algorithm [79]

$$\hat{\tau} = \frac{T_s}{4\pi}\arg\left\{\int_0^{kT} r^2(t)\exp\{j2\pi t/T_s\}\,dt\right\} - \frac{T_s}{4\pi}\arg\left\{\int_0^{kT} r^2(t)\exp\{-j2\pi t/T_s\}\,dt\right\}, \quad (4.2)$$

$$\hat{\theta} = \frac{1}{4}\arg\left\{\int_0^{kT} r^2(t)\exp\{j2\pi t/T_s\}\,dt\right\} + \frac{1}{4}\arg\left\{\int_0^{kT} r^2(t)\exp\{-j2\pi t/T_s\}\,dt\right\}. \quad (4.3)$$

Compared to the timing recovery algorithm (3.9) for QPSK that searches for the spectral lines of the magnitude-squared operation, OQPSK requires only squaring. This difference can provide a reduction in implementation complexity because timing and carrier recovery are performed via the same angular operators. However, the frequency offset estimation performance is limited by the quadrature amplitude leaking into the angle computation [80]. After the timing and carrier phase is recovered a $T_s/2$-spaced LMS equalizer removes any residual ISI.

To assess the transmission performance differences between QPSK and OQPSK three identical signals (either QPSK or OQPSK) are placed 50 GHz apart on the ITU-T grid, Fig. 4.6. All of the channels are generated using the same I/Q modulator and therefore (necessarily) demultiplexed and time-delayed (to decorrelate the bit patterns) with respect to each other before transmission. The transmission link is constructed of 6 spans of 75 km of non-zero dispersion-shifted fiber (NZDSF, G.655) or 8 spans of 90 km of SSMF (G.652). The NZDSF link employs 12 km of pre-compensation (+51 ps/nm) and 80 km of compensation (-360 ps/nm) per span

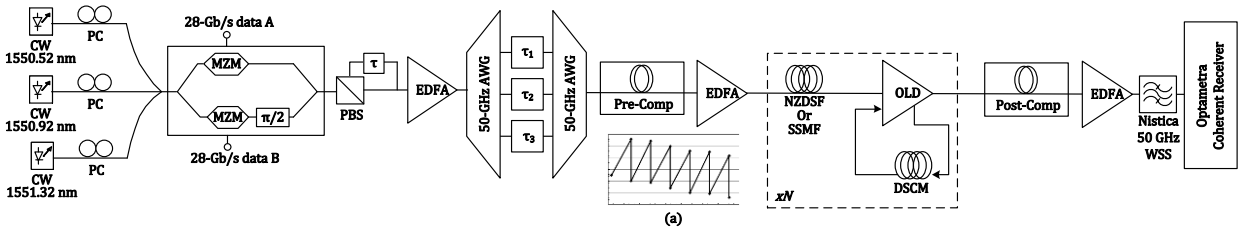


Figure 4.6. Experimental network setup. Inset (a) demonstrates the zero-symmetric NZDSF dispersion map.

(RDPS = -21 ps/nm). The SSMF link has 10 km (-170 ps/nm) or pre-compensation and 0 ps/nm of RDPS. After transmission the center channel is selected with a 50 GHz WSS, detected with a coherent receiver, digitized at 50 GS/s with a real-time scope, and then processed offline in Matlab on a PC.

It is often suggested that the first rollouts of 100G channel may occur in a "hybrid" configuration whereby currently operating 10 Gb/s OOK channels are replaced with 100G channels. However, this triple-channel arrangement is designed to isolate the nonlinear effects of either the QPSK or OQPSK modulation format since the effects of XPM due OOK neighboring channels are identical no matter the modulation format of the central channel. Since the magnitude of XPM impairments increase with decreasing effective area and decreasing dispersion, NZDSF systems are expected to exhibit a more significant performance difference between QPSK and OQPSK than in SSMF links.

Single-polarization transmission at 56 Gb/s exhibits a clear advantage for OQPSK over QPSK in NZDSF, Fig. 4.7. XPM effects accrue rapidly to degrade the signal as launch powers increase. Yet OQPSK can be launched with 1-2 dB higher power compared to QPSK before reaching the $10^{-3}$ hard-FEC BER limit. Dual-polarization experiments demonstrate a performance advantage for OQPSK across a range of launch powers in NZDSF, Fig. 4.8a, although this gain is modest. In SSMF, Fig 4.8b, OQPSK and QPSK offer nearly identical transmission capabilities.

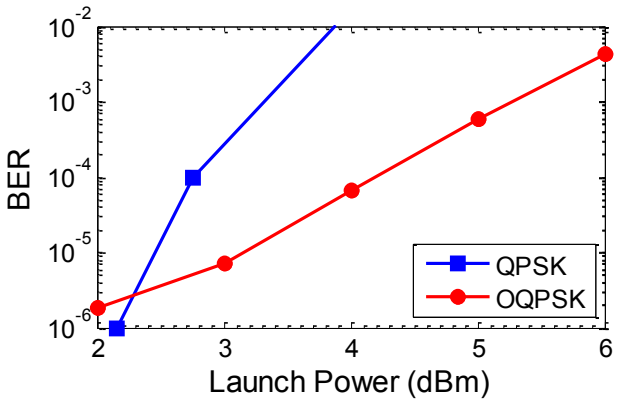


Figure 4.7. Single-polarization BER performance vs. high launch power of QPSK and OQPSK in NZDSF demonstrating a 1-2 dB advantage for OQPSK.

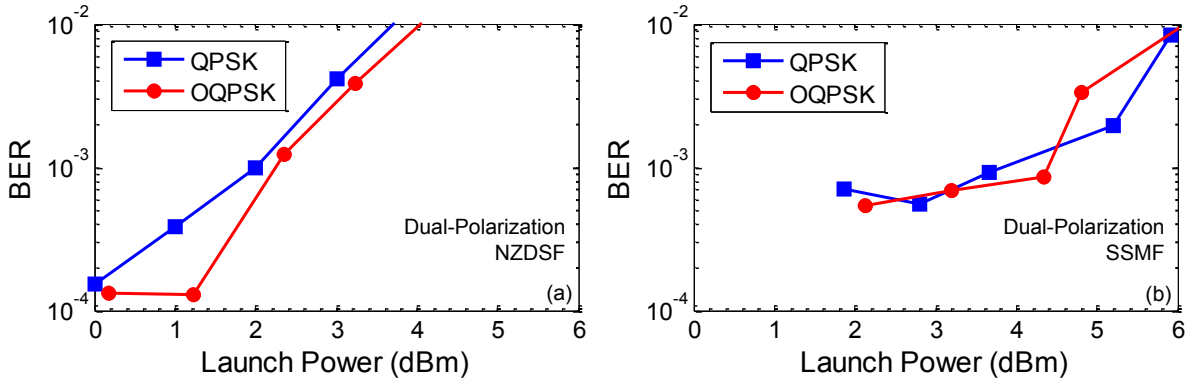


Figure 4.8. Dual-polarization BER vs. launch power comparison of OQPSK and QPSK in the (a) NZDSF link and (b) SSMF link. The performance advantage for OQPSK is noticeable, albeit modest, in the high-nonlinearity, low-dispersion NZDSF link (a).

The performance of OQPSK in the presence of AWGN is identical to QPSK, assuming that timing and carrier phase is properly estimated. And as demonstrated here, the reduced amplitude fluctuation of OQPSK may help mitigate XPM signal degradations for links with low dispersion or high nonlinearity. OQPSK therefore offers a potential option for some 100G deployment environments.

# CHAPTER 5

# SCALING 100G HYBRID OPTICAL LINKS

As explained in §4, the earliest rollouts of 100G technology are likely to occur on both existing and new infrastructure [81-83]. Existing networks designed for lower-speed channels use a range of dispersion maps and fiber types that are not necessarily optimal for phase-based modulation formats like QPSK [84]. As a consequence, it is important to be able to predict 100G transmission penalties in linear and nonlinear regimes across a range of deployment environments.

In order to identify optimum transport solutions, many network operators and hardware designers engineer extensive computer simulations unique to every application. This process is inordinately time consuming; it requires that fiber and propagation modeling are accurate to achieve meaningful results (see §5.1). Additionally, simulations often rely on relative, rather than absolute, performance penalties that are difficult to directly apply to real links.

In this effort, we develop a simulation environment with good absolute accuracy by codifying experimental components, fiber, and methods of our 100G testbed within a commercial simulation package. We then use the testbed and simulation environment in conjunction to establish a measurement of the total nonlinear phase accumulation for crafting engineering rules. To indicate the total nonlinear phase shift accrued in transmission, we employ the Nonlinear Threshold (NLT) metric. Our approach specifically identifies both SPM and XPM components of the NLT.

The NLT metric arises from the desire to aid the modeling process by encapsulating into one parameter the nonlinearity-induced transmission penalties. Recent work [85-87] has suggested that the product of per-span launch power $P_{\text{line}}$ and the number of spans $N_{\text{span}}$ is a good metric. Simulations [88] revealed for several fiber types that it is more robust to consider the *total* nonlinear phase shift $\phi_{NL}$,

$$\phi_{NL} = N_{\text{span}}\left(\gamma_{\text{line}} P_{\text{line}} L_{\text{eff,line}} + \gamma_{\text{DCF}} P_{\text{DCF}} L_{\text{eff,DCF}}\right), \tag{5.1}$$

which weights $P_{\text{line}} N_{\text{span}}$ by the nonlinear strength $(n_2/A_{\text{eff}})$ of the line fiber and dispersion-compensating fiber. As such, $\phi_{NL}$ not only includes the nonlinear phase contributions of both fiber types, but in networks where $P_{\text{line}}$ is proportional to $P_{\text{DCF}}$, $\phi_{NL} \propto P_{\text{line}} N_{\text{span}}$. The NLT is based directly on this proportionality relationship: defined as the product of $N_{\text{span}}$ and the launch power that yields a specific OSNR penalty at a reference BER. The NLT thus corresponds to a specific transmission penalty, and may be insensitive to the number of spans as long as $\phi_{NL}$ remains constant. For this work, we select the OSNR penalty to be 1.5 dB and the reference BER to be $10^{-3}$. That is, $NLT = P_{NLT} N_{\text{span}}$, where $P_{NLT}$ is the launch power corresponding to a 1.5 dB OSNR penalty at BER = $10^{-3}$.

### 5.1 Experimental and Simulation Network

The experimental and simulation networks consist of a single 112 Gb/s PDM-QPSK channel surrounded by four 10.7 Gb/s NRZ-OOK channels, two on each side in the nearest 50 GHz channels, Fig. 5.1. The signals are combined in a 50 GHz AWG and then amplified for link transmission. The point-to-point optical network consists of $N$ spans, variable from zero to eight. Each span is constructed of either SSMF or NZDSF fiber, a dual-stage EDFA, and an optional

midstage DCM. Digital signal processing of the received PDM-QPSK signal is performed according to the description in §3.1.

We examined two dispersion maps for both the SSMF and NZDSF links: 0% and 100% inline compensation per span achieved by either including or not including the DCM. The SSMF spans are nominally 90 km and the NZDSF spans are nominally 80 km. Table 5.1 contains the relevant fiber parameters. For each dispersion map, we swept the launch power of the center PDM-QPSK channel and the adjacent OOK channels independently to separately identify XPM and SPM penalties. At each combination of QPSK and OOK launch powers we determined the OSNR for BER = $10^{-3}$ by adding noise at the link termination. This experimental process was carried out on both SSMF and NZDSF links of two, four, six, and eight spans.

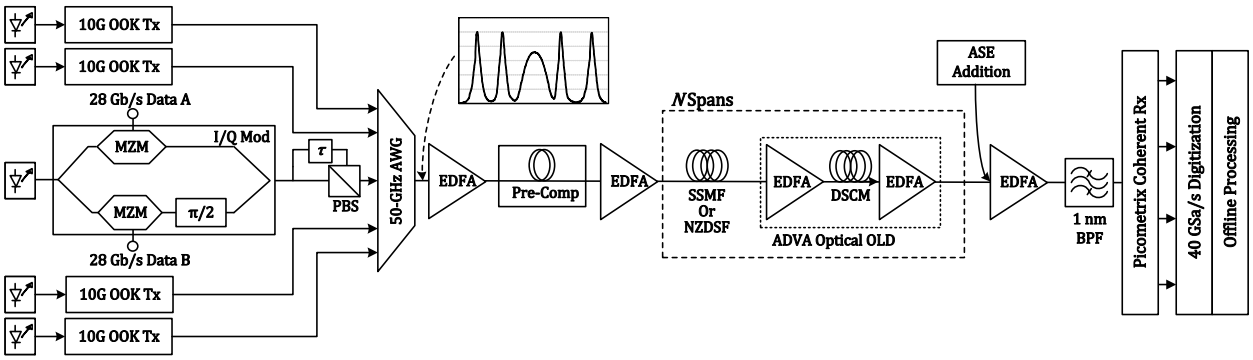


Figure. 5.1. Schematic of experimental and simulation network configuration. Inset shows optical spectrum of the PDM-QPSK channel with side OOK channels. Number of spans N is varied from 2 to 8. The ADVA OLD is a dual-stage amplifier with mid-stage access for a DSCM. Noise is added at the end of the link for OSNR analysis.

Table 5.1. Fiber parameters of the two different transport fibers and the DCF in the DSCMs. The nonlinear coefficient of DCF is nearly five times that of SSMF and 2.5 times NZDSF. *D = -107.0 for SSMF links and D = -24.8 for NZDSF links.

| PARAMETER | SSMF | NZDSF | DCF |
|---|---|---|---|
| Nonlinear index, $n_2$ ($x10^{-20}$) | 2.3 | 2.6 | 2.7 |
| Core Effective Area, $A_{eff}$ [$\mu m^2$] | 80.0 | 52.0 | 21.0 |
| Nonlinear Coefficient, $\gamma$ [km/W] | 1.165 | 2.033 | 5.209 |
| Dispersion, $D$ [ps/nm-km] | 17.0 | 4.5 | * |

## 5.2 The Simulation Environment

We use the RSoft OptSim simulation engine for software modeling. OptSim propagates complex vector signals as samples in the time domain, evolving them using the Time-Domain Split-Step method [89], and operating with IIR filtering blocks rather than FFT-based algorithms. OptSim can model all nonlinear fiber propagation characteristics, including, but not limited to, PMD, birefringence, SPM, XPM, FWM, and cross-polarization modulation (XPolM).

As a first step to quantitatively reproduce laboratory results in simulation, we measured all signal-affecting parameters of the components in the laboratory: linear and nonlinear fiber characteristics, filter shapes of AWGs and BPFs, extinction ratio and s-parameters of I/Q modulators, RF drive voltage of the modulators, and receive electrical filtering due to the coherent receiver photodiodes and oscilloscope front end. After codifying all measurable characteristics, we fine-tuned the simulation parameters to match testbed results. Working first in a back-to-back configuration, Fig. 5.2a, we finely controlled the drive voltages and biases of the I/Q modulator to yield excellent recreation of the measured 28 Gbaud NRZ-PDM-QPSK spectrum, Fig. 5.2b. We also studied (in simulation) modulator chirp, polarization dependent loss, and transmit polarization state and determined that reasonable variations in these parameters have a small effect on the back-to-back BER performance. The extinction ratio (ER) of the modulator, however, affects the slope of the BER vs. OSNR curves; it was modified to match the laboratory measurements. We note that time-domain matching is largely impractical, and find that matching transmit spectrum yields excellent results. We find absolute BER vs. OSNR convergence within ±0.25 dB between simulation and experiment in the back-to-back configuration, Fig. 5.2c.

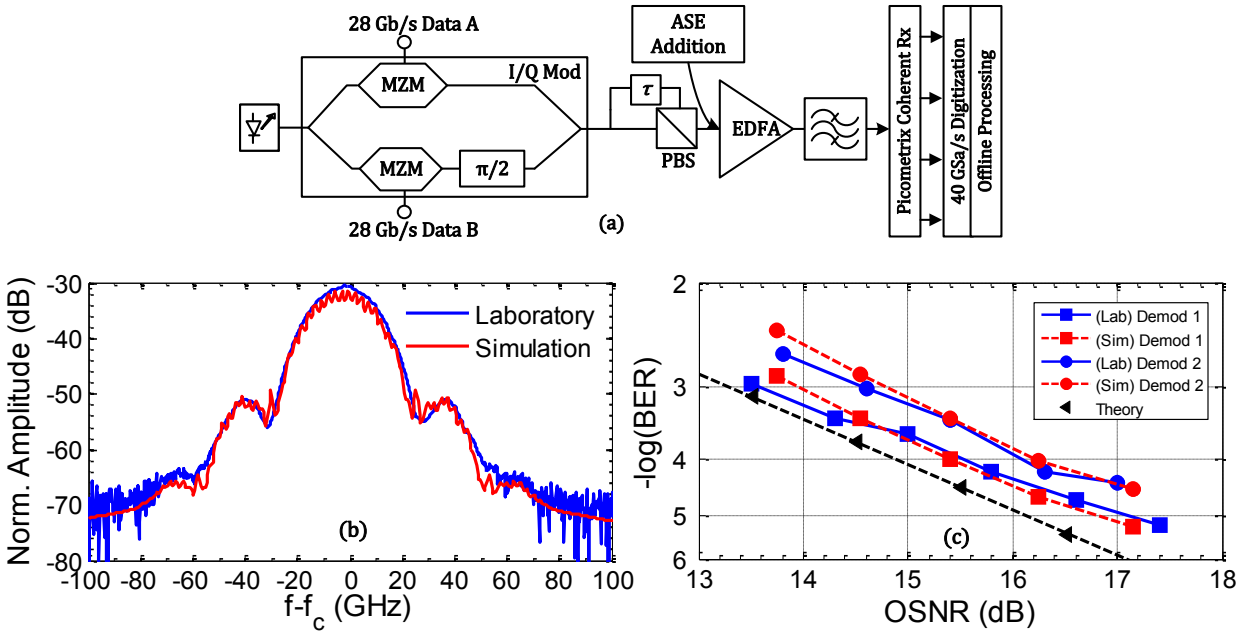


Figure 5.2. (a) Back-to-back configuration of 112 Gb/s PDM-QPSK with (b) spectra and (c) BER vs. OSNR performance comparison between laboratory and simulation for two different demodulation routines.

Adding transmission fiber greatly increases the computational complexity of the simulation and therefore the ability to reproduce laboratory results. In the linear transmission regime the primary signal impairments are CD and PMD, both of which are electronically compensated in the DSP engine. Once the transmission system enters the nonlinear regime it becomes more difficult to match the absolute simulation and laboratory result.

We achieved absolute matching of the simulation and laboratory results within ±0.5 dB in most cases, Fig. 5.3. These results are only a small sample of the total data set (it would be impractical to show all of the data here) but are a good indication of the set as a whole. The remainder of the data set is encapsulated in the NLT computation in the section to follow. Significantly, these results demonstrate robust matching across a wide range of practical link scenarios with different dispersion maps, fiber types, and link lengths. We also observe excellent correspondence between the single-channel PDM-QPSK transmission (SPM effects only) and the hybrid transmission (QPSK channel with 10G OOK neighbors) laboratory and simulation

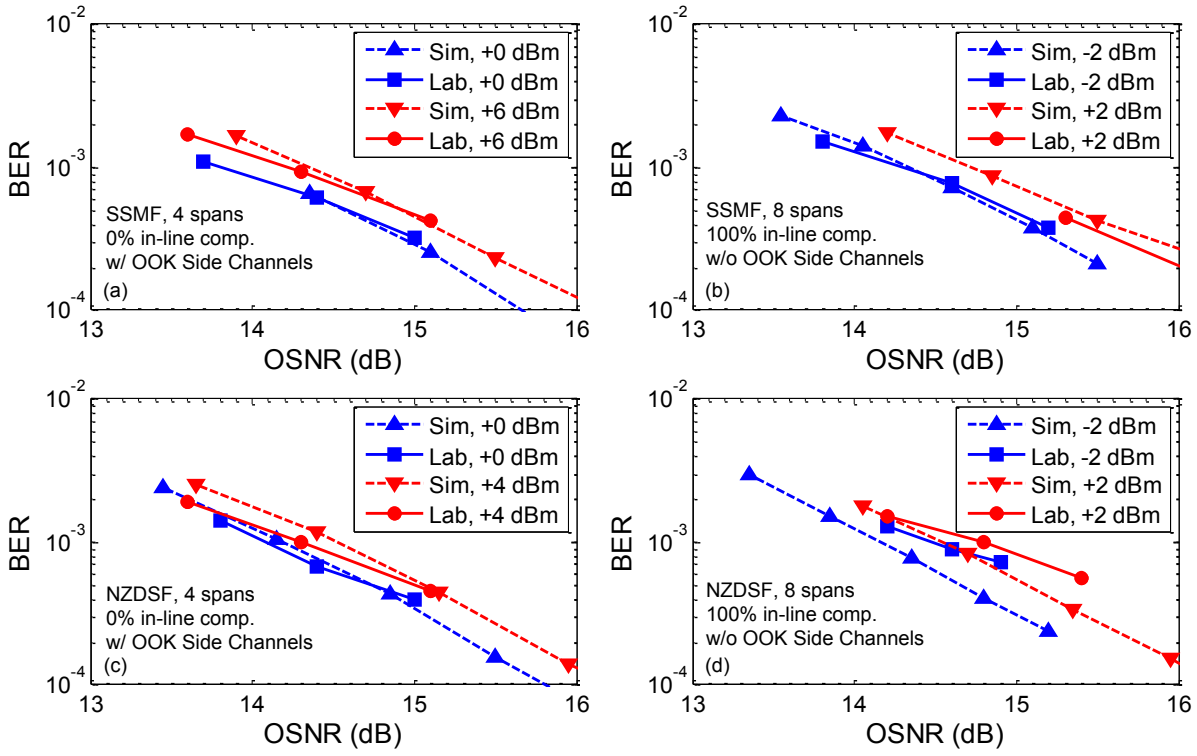


Figure 5.3. Simulation and laboratory results for PDM-QPSK transmission over a range of link configurations: (a) 4 spans of SSMF, no DCMs, +0/+6 dBm launch power, -4 dBm OOK power; (b) 4 spans of NZDSF, no DCMs, +0/+4 dBm launch power, -4 dBm OOK power; (c) 8 spans of SSMF, with DCMs, -2/+2 dBm launch power, no OOK channels; (d) 8 spans of NZDSF, no DCMs, -2/+2 dBm launch power, no OOK channels.

results. More work remains to be done, particularly for NZDSF fiber which accrues more nonlinearities because of its smaller core effective area.

### 5.3 The Nonlinear Threshold and XPM Offset

Figure 5.4 depicts an example case that depicts the separate effects of XPM and SPM. There are two distinct features: (1) at low QPSK channel launch powers (where SPM effects are expected to be low), the required OSNR increases with side channel launch power, and (2) for each side channel launch power, $OSNR_{req}$ increases with QPSK launch power after ~0 dBm. Feature (1) is attributed to XPM effects between the OOK side channels and the center QPSK channel, and feature (2) is attributed to SPM effects of the QPSK channel on itself. Importantly,

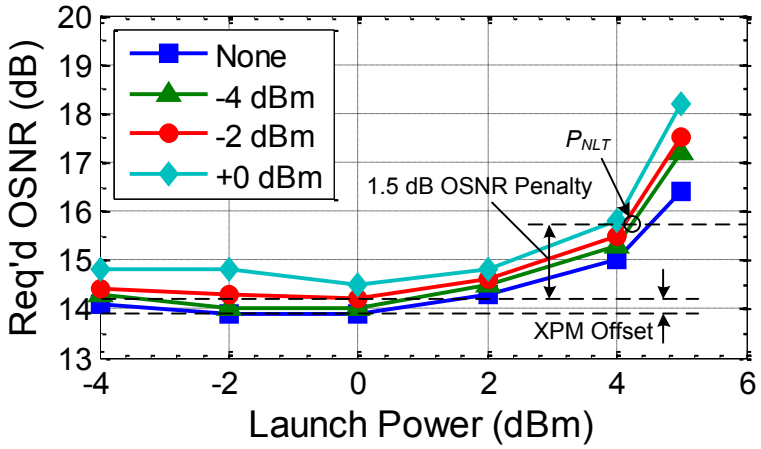


Figure 5.4. $P_{NLT}$ and XPM Offset determination from experimental data for 6 spans, NZDSF fiber with 0% inline compensation. Legend indicates launched power of side channels. $P_{NLT}$ is the power corresponding to a 1.5 dB OSNR penalty relative to the lowest launch power point (-4 dBm). The XPM offset is the required OSNR penalty relative to the side channel case at the lowest power point (-4 dBm).

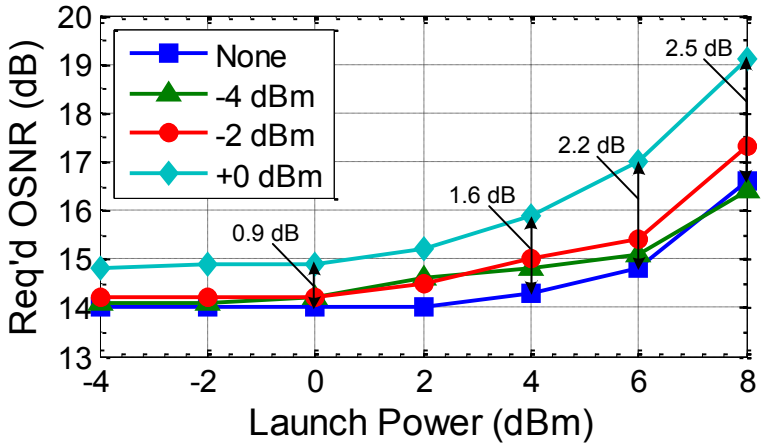


Figure 5.5. Increasing XPM penalty with increasing PDM-QPSK channel launch power for 6 spans of SSMF fiber with 100% compensation. The legend indicates launch power of side channels.

we observe for this case of no inline compensation that XPM and SPM effects are essentially independent. Also identified in Fig. 5.4 are the NLT and XPM offset metric used in later analysis, illustrated for the -4 dBm side channel case.

In contrast to 0% inline compensation cases, we observe that XPM and SPM penalties are not necessarily independently in 100% compensation cases. Depicted in Fig. 5.5 by black arrows, we see an enhancement of the required OSNR beyond the simple addition of SPM and XPM penalties. This effect is most pronounced in SSMF and NZDSF links of six or eight spans

and 100% inline compensation. This characteristic marks an XPM-SPM interaction in the determination of the BER (and hence, OSNR penalty).

### 5.4 Results

We determined the XPM offset and NLT for link configurations examined. The results for 0% compensated links are in Fig. 5.6, and for 100% compensated links in Fig. 5.7. Figures 5.6a and 5.6b depict the measured and simulated NLT for 0% inline compensation in SSMF, and Figs. 5.6c and 5.6d contain the results for NZDSF. We note that for both simulation and experiment *and* for both SSMF and NZDSF, the NLT is insensitive to changing side channel power (previously exampled in Fig. 5.4). We attribute this characteristic to the group delay difference arising from the large local net dispersion of 0% compensated cases. Both simulation and laboratory results show 1.5 to 2 dB advantage and lower XPM penalties for SSMF fiber over NZDSF fiber, due to SSMF larger effective area and higher dispersion. Additionally, the NLT differs by no more than 1 dB between simulation and experiment for links of both fiber types. The NLT increases as the total link length expands, indicated improved tolerance to nonlinear transmission effects. Simulations also revealed the same NLT slope for span counts of 12 and 16.

For 100% compensated cases, Fig. 5.7, the NLT *decreases* with both increasing span count and side channel launch power. This feature indicates an increasing nonlinear phase penalty on the QPSK channel due to SPM and XPM effects. These schemes with low local net dispersion therefore accrue more nonlinear phase. Both simulation and experiment accordingly demonstrate lower absolute NLT compared to 0% compensated cases.

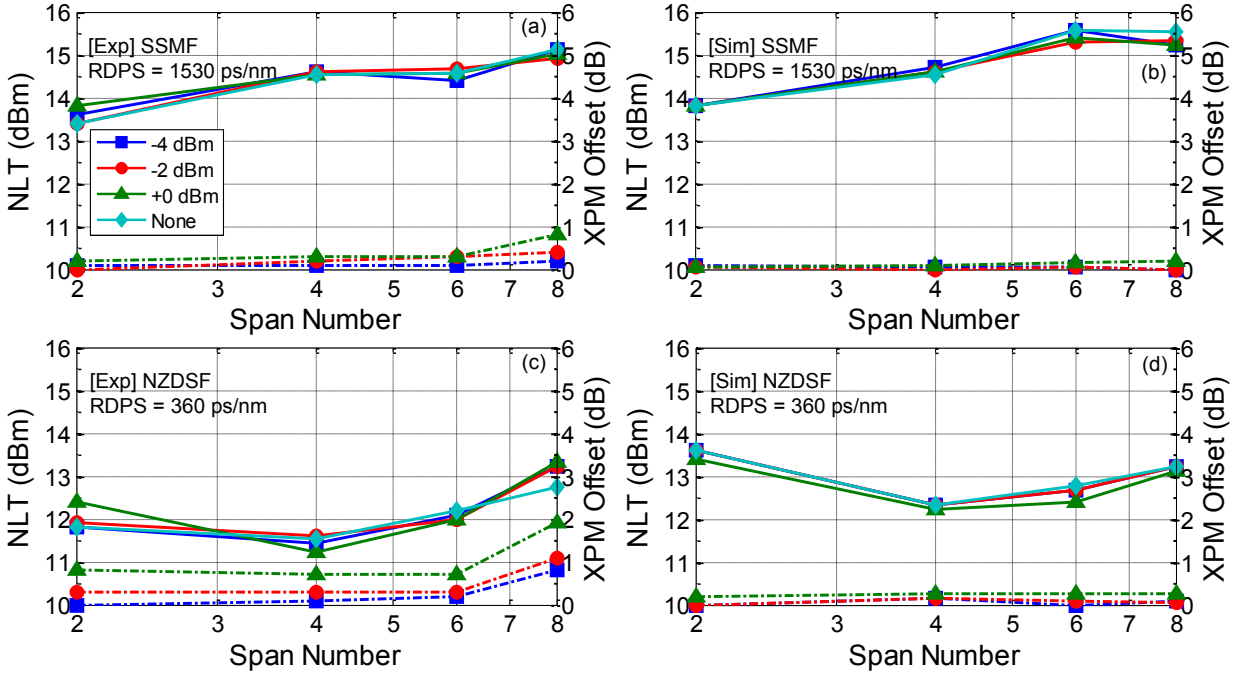


Figure 5.6. Nonlinear threshold (solid lines) and XPM Offset (dashed lines) for 0% inline compensation in (a), (b) SSMF and (c), (d) NZDSF in both experiment and simulation. The legend in (a) indicates OOK side channel launch power and applies to all figures (a)-(d). Higher NLT means better performance. NLT demonstrates insensitivity to side channel power in both SSMF and NZDSF links, and increases with increasing span count.

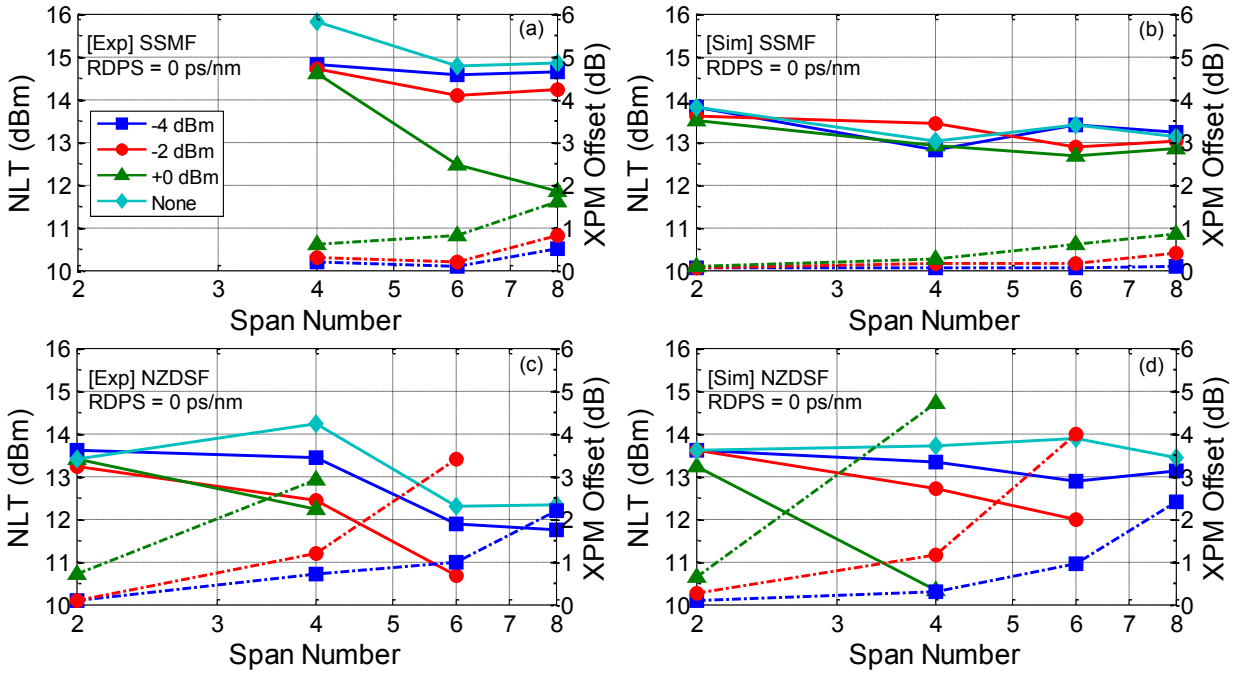


Figure 5.7. Nonlinear threshold (solid lines) and XPM Offset (dashed lines) for 100% inline compensation in (a), (b) SSMF and (c), (d) NZDSF in both experiment and simulation. The legend in (a) indicates OOK side channel launch power and applies to all figures (a)-(d).

The dashed lines of Figs. 5.6 and 5.7 depict the XPM offset. We observe relative insensitivity of the XPM offset to increasing span count in 0% compensated cases compared to 100% compensated cases. The XPM offset is especially sensitive to both side channel power and span count in NZDSF links with 100% compensation. This attribute is consistent with NLT difference between the two fiber types – SSMF links demonstrate higher NLT across all span counts and dispersion maps.

Lastly, we performed additional simulations employing a setup identical to that in Fig. 5.1, replacing only the 10G side channels with 28 Gbaud PDM-QPSK channels to match the center channel. As in the previous tests, we fixed the side channel launch power and scanned the center PDM-QPSK channel to extract $P_{NLT}$. We compare the NLT and XPM Offset metrics for QPSK and OOK side channels in the SSMF link with both 0% and 100% inline compensation, Fig. 5.8.

We immediately observe that the NLT is nearly identical for both side channel cases in both dispersion compensation schemes (although the 100% compensation case exhibits a lower NLT for very low span count). Because the side channels are fixed in launch power, they provide a fixed XPM penalty that increases with span count. Our NLT is therefore determined only by the change in center channel launch power. Accordingly, our NLT metric exhibits behavior similar to that observed for the OOK side channel case. The XPM Offset contains the main difference in performance for these two cases. With 0% inline compensation the XPM Offset is small for both side channel cases as expected, since group velocity mismatch quickly walks off adjacent channels. In the 100% compensated link, the XPM Offset monotonically increases with span count when OOK channels are used, up to ~1 dB at 8 spans. In contrast, the PDM-QPSK side channels incur < 0.25 dB XPM penalty at 8 spans [90].

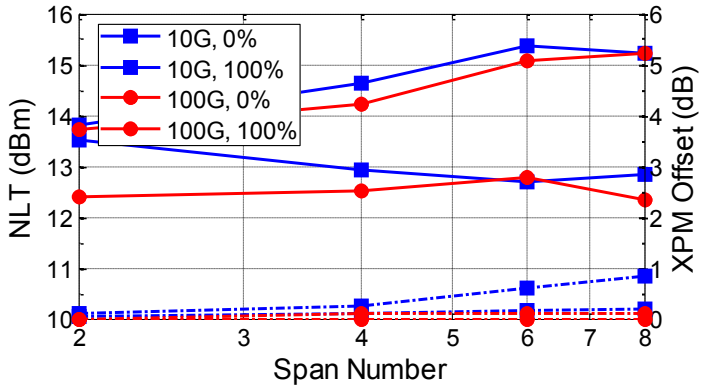


Fig. 5.8. Simulation results comparing the NLT and XPM Offset metric for 10.7 Gb/s OOK (10G) and 112 Gb/s (100G) PDM-QPSK side channels for 0 and 100% inline compensation. The channel of interest in both cases is 112 Gb/s PDM-QPSK. The NLT values and trends are similar for different side channel types on the same dispersion map.

To conclude, through extensive experimentation and measurements, we established a simulation environment accurate to within ±0.25 dB in linear regimes and ±1.5 dB in highly nonlinear regimes. We utilized this combined experimental and simulation testbed to investigate the nonlinear performance of a hybrid 100G/10G network. The nonlinear penalties were quantified via the NLT metric, the product of $P_{NLT}$ and Nspan, and supplemented by the introduction of the XPM offset metric. Both simulation and experiment results reveal that the highly dispersive regime of 0% inline-compensated links yields stronger tolerance to nonlinearities, especially XPM, and are relatively straightforward to create design rules. Links comprised of all QPSK channels will have similar yet improved performance compared to the demonstrated hybrid 0% compensation case and should exhibit the same NLT and similar ease of creating design rules.

Both NZDSF and SSMF links with 0% inline compensation demonstrated NLT insensitivity to OOK side channels with launch power up to +0 dBm. The NLT also increases with increasing span count. Conversely, the NLT degrades with increasing span count in 100% inline-compensated links due to accumulating XPM effects. NZDSF links demonstrate 1.5 to 2.0 dB more NLT penalty compared to SSMF links. Confirmed in simulation, these results allow

accurate estimation of nonlinearity-constrained link performance for a range of span counts. Additionally, the results establish a means of greatly simplifying point-to-point optical network design [90].

# CHAPTER 6

# CROSSTALK IMPAIRMENTS IN 100G DWDM NETWORKS

Network transparency in future DWDM networks is crucial, and has been driven by ROADM deployments [92, 93]. ROADMs provide a flexible and cost-effective way to add or drop one or more wavelengths at a node, while passing other wavelengths [94-97]. The filter shapes of the switching elements that comprise a ROADM are non-ideal; they vary in spectral shape and isolation [98]. Therefore, added signals are corrupted by the residual signals within the same channel, giving rise to in-band crosstalk. Other sources of crosstalk include back-reflections from imperfect connectors, Rayleigh backscattering, stimulation Brillouin scattering, and FWM in low-dispersion fiber. These system impairments are additive at each successive add/drop node. Additionally, the non-uniform spectral content of crosstalk signals prevents the simple use of crosstalk power (crosstalk-to-signal ration) as the sole metric for penalty prediction [99].

The simulation results in [95] show that the "weighted" crosstalk is a reliable metric for determining system transmission penalties of ROADM crosstalk in a 43 Gb/s DPSK system. Several other efforts have also been made to compute the crosstalk-induced transmission penalties [100-102]. In this work, we demonstrate that weighted crosstalk is a reliable parameter for penalty prediction in 112 Gb/s PDM-QPSK system, regardless of spectral shape, bandwidth, or wavelength offset of ROADM filters. We also show that this analysis is applicable to systems with different fiber types and dispersion maps. Then, we extend the crosstalk investigation to

long-haul 112 Gb/s systems operating in the nonlinear regime and demonstrate enhancement of nonlinear penalties due to in-band crosstalk.

### 6.1 ROADM Filtering and In-band Crosstalk

The 1xN wavelength-selective switch (WSS) is basic building block of ROADM. In Fig. 6.1, $WSS_1$ and $WSS_2$ drop and add channels, respectively. Each WSS is characterized by a bandpass filter. The amplitude spectrum of a commercial WSS bandpass filter (for a single channel) is shown in Fig. 6.2 for various channel bandwidths. Since the filters that describe the WSS transfer function are imperfect, signal propagation through a sequence of ROADM nodes spectrally shapes the transmitted signals, limiting bandwidth and creating amplitude and phase variations. The effective bandwidth of cascaded ROADMs is a limiting factor is optical data transport. For example, the filter shapes of the commercial WSS, Fig. 6.2, are usually modeled as a third-order super-Gaussian. When cascaded, the effective 3-dB bandwidth of a super-Gaussian filter decreases. Specifically, after nine passes through a $3^{rd}$-order SG-modeled ROADM a signal would see less than 40 GHz of effective passband, Fig. 6.3. Higher-order SG filters have sharper roll-off allowing their cascaded bandwidth to remain high while low-order SG filters exacerbate the effective bandwidth decrease due to cascaded filters.

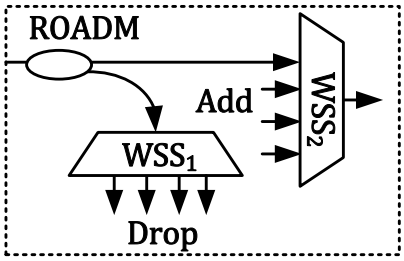

Figure 6.1. 1xN WSS-based ROADM.

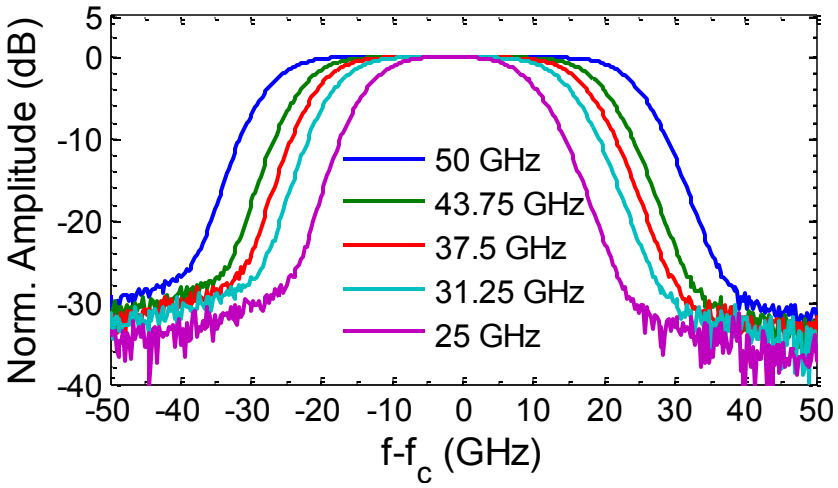


Figure 6.2. Passband shape of a commercial WSS [41] for various filter channel spacing choices.

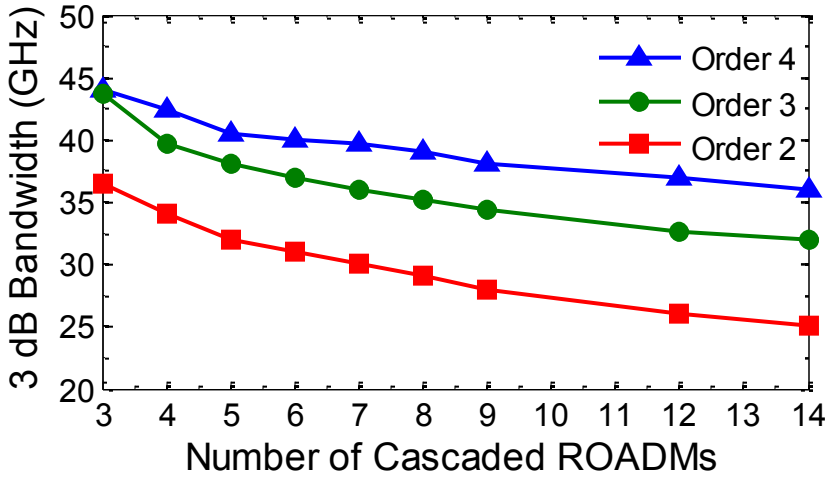


Figure 6.3. Bandwidth narrowing for single channel passband with the increasing number of 50-GHz ROADMs for different super Gaussian orders.

The wavelength addition function of a ROADM, Fig. 6.4, is defined in the following way: $S_i(f)$ is the primary channel of interest (add channel), $S_b(f)$ is the blocked (or dropped) channel, $H(f)$ is the WSS filter that drops the channel, and $X(f) = H(f)S_b(f)$ is the net crosstalk spectrum. In-band crosstalk arises when the dropped channels are not perfectly blocked by the transmit port of $WSS_2$.

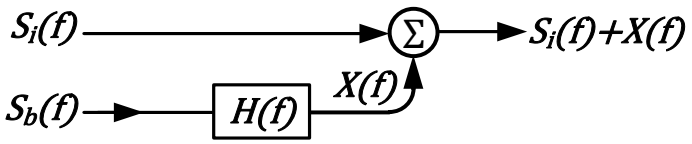

Figure 6.4. Signal power flow of in-band crosstalk, including notation.

In the general sense in-band crosstalk may be spectrally different than the primary channel of interest. Conventional crosstalk is defined as the *unweighted* ratio of total power in the interfering channel to the total power in the primary signal

$$\frac{P_x}{P_i} = \frac{\int X(f)df}{\int S_i(f)df}. \tag{6.1}$$

However, this definition (6.1) fails to account for the spectral content of the crosstalk signal relative to the primary signal. Crosstalk signal power near the edges of the primary channel induces smaller penalties than crosstalk power near the center [102]. That is, the penalty induced by in-band crosstalk very much depends on the characteristics of the blocking filter $H(f)$.

Therefore we introduce a weighting function $W(f)$ that is proportional to normalized spectral shape of the primary signal. That is

$$W(f) = \frac{kS_i(f)}{av[S_i(f)]}. \tag{6.2}$$

The weighted crosstalk spectrum is computed as $X_W(f) = X(f)W(f)$. Integration to determine total power in the spectra yields the net weighted crosstalk value:

$$\frac{P_{X_W}}{P_i} = \frac{\int X(f)W(f)df}{\int S_i(f)df}. \tag{6.3}$$

The scale factor $k$ of the weighting function $W(f)$ is determined by ensuring that the weighted crosstalk metric yields the same result as the standard crosstalk metric when the crosstalk signal has the same spectrum as the primary signal, $S_i(f) = X(f)$. Using (6.2) and (6.3)

$$k = \frac{av[S_i(f)]\int S_i(f)df}{\int S_i^2(f)df}, \tag{6.4}$$

and therefore

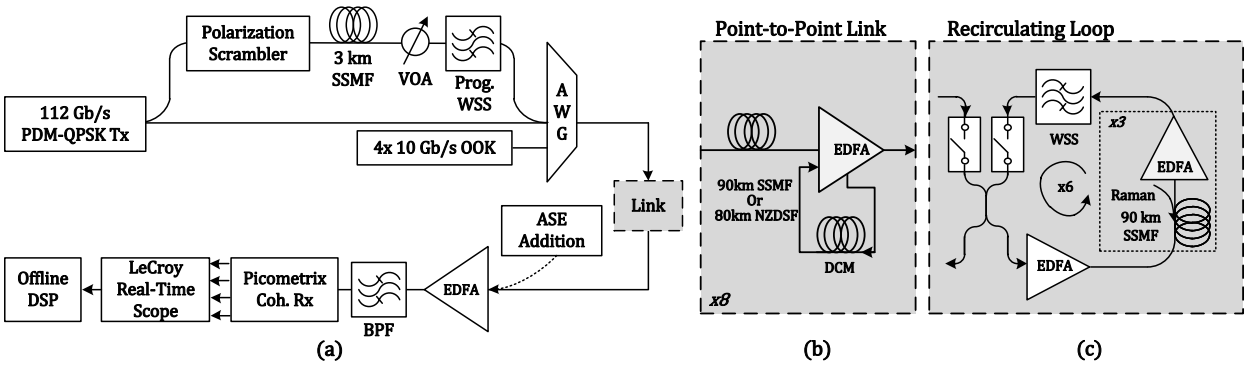


Figure 6.5. Experimental network configuration of (a) crosstalk addition and detection. The transmission link is configured as either a (b) ~700 km point-to-point optical link using SSMF or NZDSF fiber or a (c) 1600 km recirculating loop with SSMF and EDFA/Raman amplification.

$$\frac{P_{X_W}}{P_i} = \frac{\int X(f) S_i(f) df}{\int S_i^2(f) df}. \tag{6.5}$$

Eqn. (6.5) has the required properties of being zero when the crosstalk $X(f)$ is totally out of band and reproducing the conventional crosstalk definition when $X(f) = \alpha(f)$ where $\alpha$ is the scale factor; the weighted crosstalk reduces to $\alpha$.

Experimentally, the crosstalk signal is created by splitting off a fraction of the primary PDM-QPSK signal, Fig. 6.5. This copy of the primary signal is then polarization scrambled, propagated through 3 km of fiber to reduce carrier coherence and eliminate bit-alignment penalties, attenuated, filtered, and then added back to the primary signal. The programmable WSS employs a Digital Micromirror Device (DMD) [41] to control the center wavelength, isolation, and passband shape of $H(f)$, the blocking filter. This experimental arrangement replicates the ROADM functionality diagramed in Fig. 6.4. There are other potential sources of crosstalk in optical communication systems including back-reflections from imperfect connectors, Rayleigh backscattering, and Four-Wave mixing products; this experimental setup is a completely general method of crosstalk generation.

A wide variety of filter shapes were explored. Figure 6.6 show the normalized filter shapes programmed into the WSS, along with corresponding shapes of the primary signal $S_i(f)$

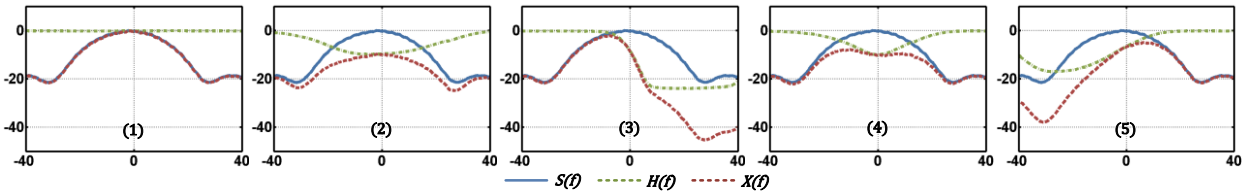


Figure 6.6. Insets (1)-(5) show the QPSK spectrum *S(f)*, the chosen and measured WSS filter shapes *H(f)*, and the crosstalk spectrum after filtering *X(f)*. The y-axis has units of dB and the x-axis has units of GHz.

and crosstalk signal $X(f)$. Filter 1 is the control case of no filtering (e.g. the interfering channel is an exact copy of the primary channel). Filter 2 is the blocked channel of a 50 GHz WSS with the max isolation reduced to 10 dB. Filter 3 is a 0.17 nm shift to longer wavelength of the standard blocking channel. Filter 4 is a "pinched" blocking channel with approximately 0.2 nm of bandwidth and reduced isolation by 15 dB. Filter 5 is a 0.17 nm shift to shorter wavelength with reduced isolation to 18 dB.

The combined primary plus crosstalk signal is first transmitted through the point-to-point link of Fig. 6.5b, which is arranged in one of three configurations.

1. 90 km SSMF spans with matching -1530 ps/nm DCMs (100% inline compensation) and -170 ps/nm of pre-compensation;
2. 80 km NZDSF spans with matching -360 ps/nm DCMs (100% inline compensation) and -170 ps/nm of pre-compensation;
3. 80 km NZDSF spans without DCMs or pre-compensation (0% inline compensation).

Using a launch power of +2 dBm, we measured the BER as function of OSNR of the PDM-QPSK for each link configuration (1)-(3) without crosstalk added. We then measured the OSNR vs. BER for each filter shape (1)-(5), Fig. 6.7, over a range of crosstalk powers, repeating for each link configuration. After extracting the required OSNR for BER = $10^{-3}$ for all cases, we computed the required OSNR penalty with respect to the *same* link configuration without crosstalk. Figures 6.7(a), (b), and (c) show this OSNR penalty as a function of *unweighted*

crosstalk (the ratio of power in the crosstalk signal to power in the primary channel). The PDM-QPSK launch power in all cases is +2 dBm.

Crosstalk without filtering induces largest OSNR penalties (Filter 1 case) per amount of crosstalk in all link configurations. Filter 2, which suppresses signal power in the center of crosstalk band, causes lowest penalties in all link cases. Filter 4, designed to emulate a "pinched" blocked channel, with approximately 0.2 nm of bandwidth (as opposed to 0.4 nm) and reduced isolation, offers second-lowest OSNR penalties for all link configurations. These observations clearly suggest that a blocking filter which reduces the relative amount of crosstalk power in the center of the band offer lowest performance penalties.

Using the *weighted* crosstalk metric, Figs. 6.7(d)-(f), there is a one-to-one correspondence between the crosstalk and the OSNR penalty. The weighted crosstalk thus accounts for the effects of spectral shaping, and can be used to readily predict the OSNR penalty for any filter profile. Furthermore, this weighting technique works for equally well for each of the three link configurations examined.

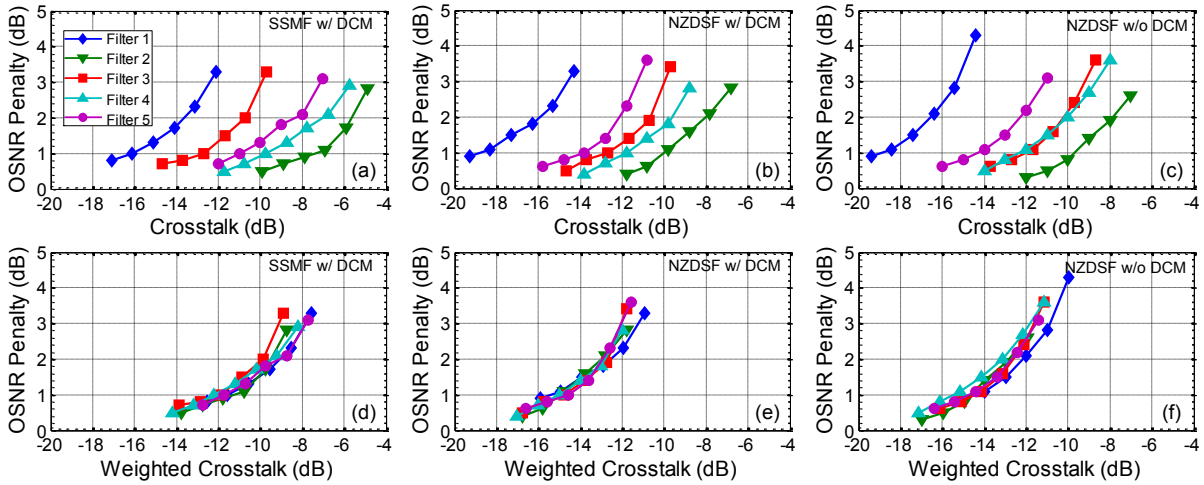


Figure 6.7. OSNR penalty for BER $=10^{-3}$ vs. unweighted and weighted crosstalk in an 8-span point-to-point link of (a), (d) SSMF fiber with matching DSCMs, (b), (e) NZDSF fiber with matching DSCMs, and (c), (f) NZDSF fiber without DSCMs. PDM-QPSK launch power in all cases was +2 dBm. The legend in (a) applies to all cases (a)-(f).

## 6.2 Nonlinearity-Enhanced Crosstalk Effects

In-band noise can create both linear and nonlinear transmission penalties [103] and it is therefore important to understand the potential nonlinear impairments that arise due to in-band crosstalk. Two different link configurations are examined, Fig. 6.5, and for simplicity only unshaped crosstalk (Filter 1, Fig. 6.6) is used. For each link configuration in these transmission experiments the OSNR penalty is computed with respect to the required OSNR for BER = $10^{-3}$ of the same link configuration *without crosstalk*.

First, we observe that the NZDSF link exhibits additional transmission penalty compared to the SSMF link at the same launch power, Fig. 6.8. Second, the crosstalk penalty increases with increasing launch power. Because each penalty is measured relative to the same link configuration without crosstalk, this data demonstrates an enhancement of the crosstalk penalty that originates from nonlinear mechanisms. We also observe nonlinearity-enhanced crosstalk penalty for increasing transmission length, Fig. 6.9. For example, the 1620 km SMF transmission tolerates 0.5 dB less crosstalk (at the 2 dB penalty mark) than does the back-to-back. When moving from +2 to +3 dBm the tolerance again decreases by 1.5 dB, Fig. 6.9. Note that the results demonstrated in Figs. 6.8 and 6.9 are for the single-channel transmission case. That is, without the 10 Gb/s OOK side channels shown in 6.5a.

Inter-channel nonlinearities also enhance the crosstalk-induced transmission penalties in a similar manner to the mixing of ASE and signals [104]. We add the four 10 Gb/s OOK channels depicted in Fig. 6.5a to propagate with the center 112 Gb/s PDM-QPSK channel on a 50 GHz grid (a “hybrid” link configuration). The in-band crosstalk penalties for -2 dBm OOK side channels are 3 dB larger than for transmission without the side channels (measure at a penalty of 2 dB), Fig. 6.10.

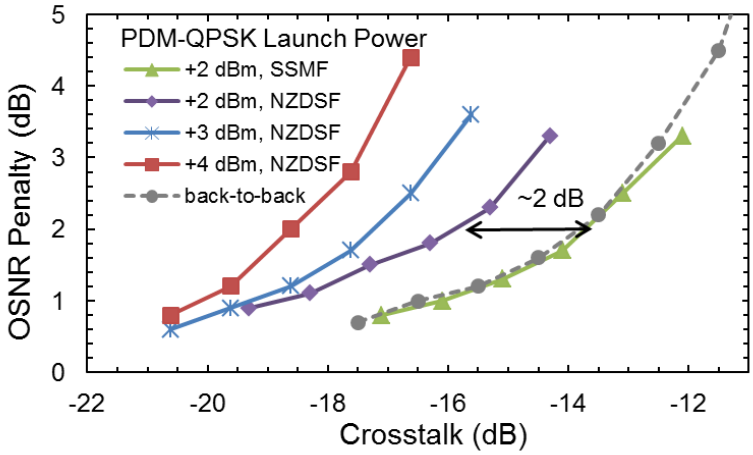


Figure 6.8. Crosstalk penalty comparison of point-to-point SSMF (8x90 km) and NZDSF (8x80 km) transmission for various launch powers.

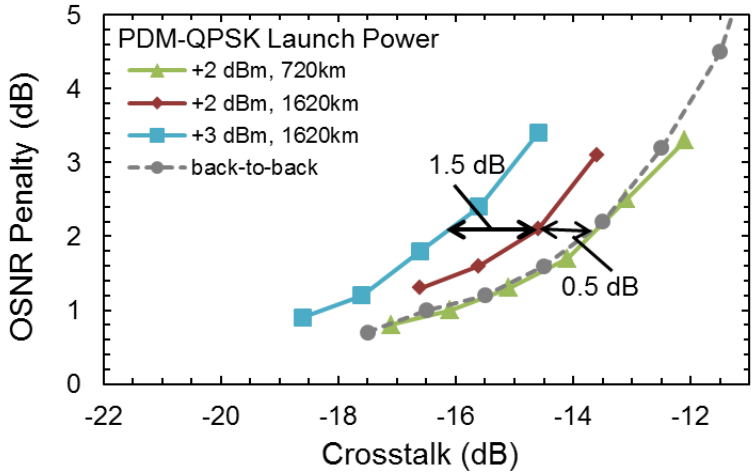


Figure 6.9. Crosstalk penalty comparison of 720 km and 1620 km SSMF transmission with two different launch powers.

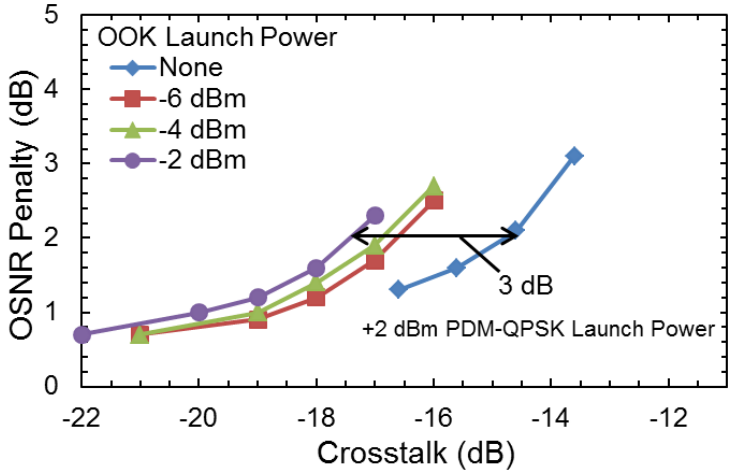


Figure 6.10. Crosstalk penalty comparison after 1620 km SSMF transmission with different OOK side channel powers.

The inter- and intra-channel nonlinear interactions that cause the crosstalk penalty enhancement can be explained via the parametric gain (PG) process [104]. The nonlinear interaction of signal and in-band ASE power is a PG process that produces nonlinear phase noise (NLPN) and amplitude noise (NLAN). The crosstalk power introduced by non-ideal ROADM filters is considered a noise source (it is incoherent, uncorrelated, and statistically independent of the channel of interest) and consequently the NLPN and NLAN due to the PG interaction with the primary signal increase with both signal and crosstalk power as well as with the introduction of adjacent channels [105].

The transmission penalties for in-band crosstalk are larger than for ASE of the same power. To demonstrate this feature the simulated back-to-back BER vs. OSNR was computed and compared against the simulated BER vs. optical signal-to-crosstalk ratio (OSXR), Fig. 6.11. The OSNR and OSXR of Fig. 6.11 were measured in a 0.4 nm (50 GHz) bandwidth – approximately the bandwidth of the PDM-QPSK signal – for a fair comparison. The red curves vary $OSXR_{0.4nm}$ at a fixed $OSNR_{0.4nm}$: 20 dB (solid) and 9 dB (dashed). With 20 dB of $OSNR_{0.4nm}$ the crosstalk power must be ~1.5 dB lower to achieve the same performance. If we color the ASE noise by forcing it to have the same spectral shape as the crosstalk signal (blue

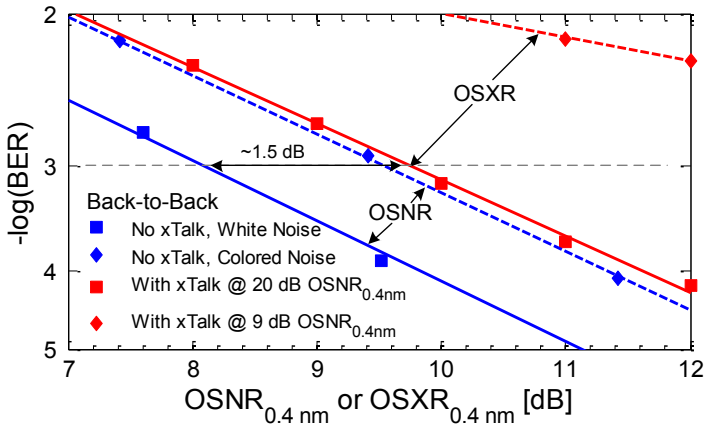


Figure 6.11. Blue curves: simulated BER vs. $OSNR_{0.4nm}$ for white and colored noise. Red Curves: simulated BER vs. $OSXR_{0.4nm}$ with 20 dB and 9 dB of crosstalk addition.

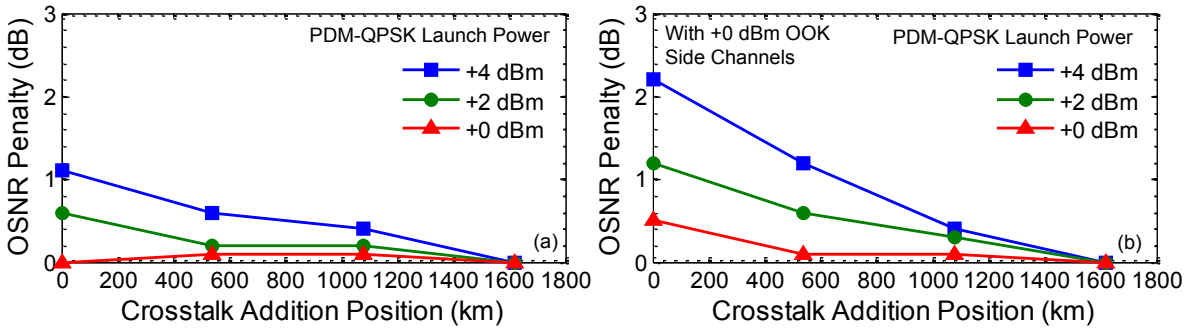


Figure 6.12. Simulation results of adding crosstalk at various points in the 1620 km SSMF transmission for (a) single-channel transmission and (b) with OOK side channels.

dashes) then the BER penalty is similar to the crosstalk-induced penalty. The BER performance is therefore revealed to be dependent on the spectral shape of the additive noise. Furthermore, crosstalk can be considered colored noise for the sake of determining its effect on signal performance and the nonlinear penalties induced by the crosstalk noise will be larger than those induced by the equivalent power of white noise.

The nonlinearity-enhanced crosstalk penalties can also be demonstrated by propagating the crosstalk signal different distances. Using simulations we varied the point of crosstalk addition from the beginning to the end of the 1620 km SSMF link, Fig. 6.12, with both single-channel and hybrid transmission setups. With -12 dB of crosstalk we observe that as the crosstalk addition position moves from the beginning to the end of the link the OSNR penalty decreases. For the single-channel transmission, Fig. 6.12a, the OSNR penalty also increases with as launch power increases. When OOK side channels are added, Fig. 6.12b, the OSNR penalty further increases.

These results demonstrate that crosstalk addition nearer the termination of the link induces smaller transmission penalties, especially for high launch powers. In other words, the system with less nonlinear interaction between crosstalk and signal power achieve greater tolerance to crosstalk. If the total crosstalk power is distributed and added in equal amounts

along the link then the penalty is less than if the total crosstalk power were added at the beginning of transmission, but more than if added near the end.

### 6.3 Ending Remarks

This work has reviewed a significant impairment for ROADM-enabled 100G networks. We have demonstrated experimentally the efficacy of using a weighted crosstalk metric to predict OSNR penalties in 112 Gb/s PDM-QPSK networks regardless of the spectral shape, bandwidth, or wavelength offset of the crosstalk. This crosstalk weighting technique is readily extensible to field-deployed systems that may be impacted by multiple sources of crosstalk. In the second part of this effort we demonstrated that fiber nonlinear interactions enhance the crosstalk-induced transmission penalties via PG processes. Simulation results confirm these experimental observations by demonstrating that crosstalk penalties increase with transmission length and with the addition of neighboring WDM channels.

# CHAPTER 7

# CONSIDERATIONS FOR THE GRID-AGNOSTIC 100G PDM-QPSK NETWORK

## 7.1 Filter Bandwidth and Carrier Spacing Tolerances of 32 Gbaud PDM-QPSK

Research efforts to move beyond 100 Gb/s per-channel line rates requires optimization of spectral efficiency. Recent work [106-109] has proposed all-optical multi-subcarrier generation as a technique to increase transmission capacity while leveraging lower-speed electronic hardware. Other work [110-112] has demonstrated the tolerance to subcarrier spacing and filter widths for multi-carrier systems with 100 Gb/s channel rates. Here, we investigate multi-subcarrier, 32 Gbaud PDM-QPSK tolerance to subcarrier spacing and filtering.

At 32 Gbaud, PDM-QPSK supports the ~28% overhead required for enhanced (soft) FEC [51] on 100 Gb/s line rates. We report the required OSNR for Q = 3 (BER = $1.3 \times 10^{-3}$) for a combination of subcarrier spacing and optical filtering less than the standard 50 GHz through an all-EDFA 1600 km link. Results reveal that proper selection of optical and electrical filtering enables tight (37.5 GHz) channel spacing in both linear and nonlinear transmission regimes, increasing system spectral efficiency compared to 28 Gbaud.

The experimental setup, Fig. 7.3, shows generation of phase-locked subcarriers by driving a lithium niobate phase modulator with a sine wave ~8 Vpp. Driving a $LiNbO_3$ modulator in this way can create 4 or 5 unique subcarriers, depending on the drive voltage and bandwidth of the modulator. The drive frequency of the modulator determines the frequency spacing between the subcarriers. WSS 1 separates the center carrier and two nearest harmonics.

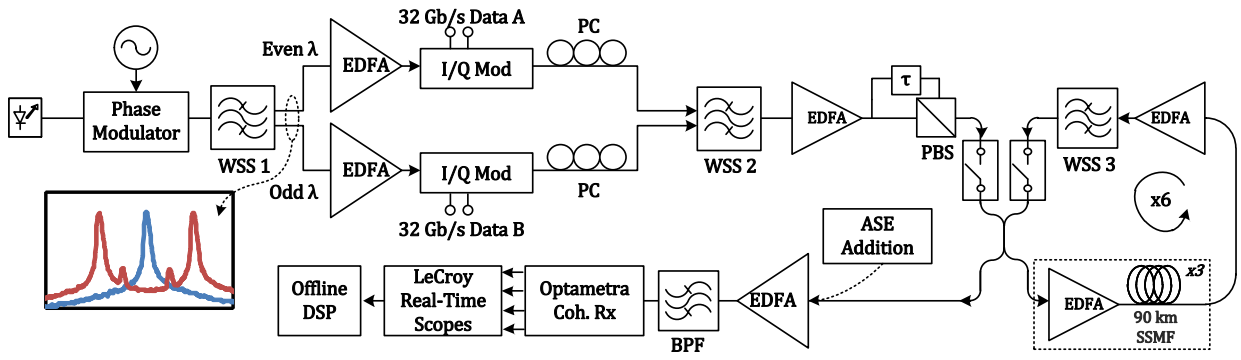


Figure 7.1. Experimental network configuration showing subcarrier generation from a single laser, all-EDFA recirculating loop, and coherent reception. Inset depicts phase-locked harmonics at the output of the phase modulator. WSS 1 is used as an interleaver to separate subcarriers, WSS 2 is used to filter each channel, and WSS 3 is employed as a gain equalizing filter.

The harmonics and center carrier are modulated independently at 32 Gbaud before recombination in WSS 2, which controls the transmit filter bandwidth. After recombination, the signals are polarization multiplexed to make 128 Gb/s PDM-QPSK per subcarrier, yielding a total channel rate of 384 Gb/s.

The recirculating loop consists of three spans, each span comprised of a single EDFA and 90 km span of SSMF fiber. The loop also contains a WSS configured as a gain equalizing filter (GEF). The data is circulated six times in the loop before unloading. The center PDM-QPSK channel is detected by a coherent receiver, and then digitized using a pair of LeCroy real-time oscilloscopes at 80 GS/s and ~30 GHz of analog bandwidth. After digitization and before processing, we employ a software Chebyshev filter of order 10 and cutoff frequency 20 GHz to remove neighboring signal energy received in the 30 GHz electric bandwidth of the scope. Offline processing is performed as described in §3.1.

For each subcarrier spacing (50, 43.75, 37.5, and 31.25 GHz) we program WSS 2 to have either 50, 43.75, 37.5, 31.25, or no per-subcarrier filtering (~$4^{th}$ order Super-Gaussian), illustrated in Fig. 7.2. The filter bandwidths are selected to always be less than or equal to the

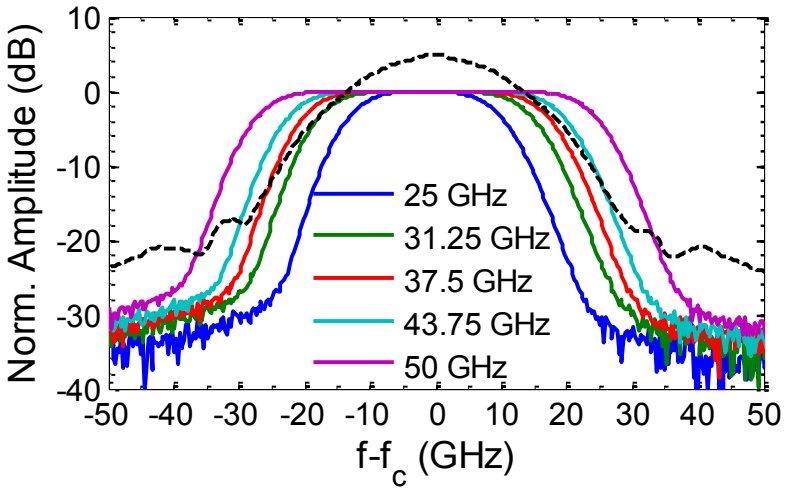


Figure 7.2. $WSS_2$ filter shapes for each setting compared to the 32 Gbaud PDM-QPSK signal.

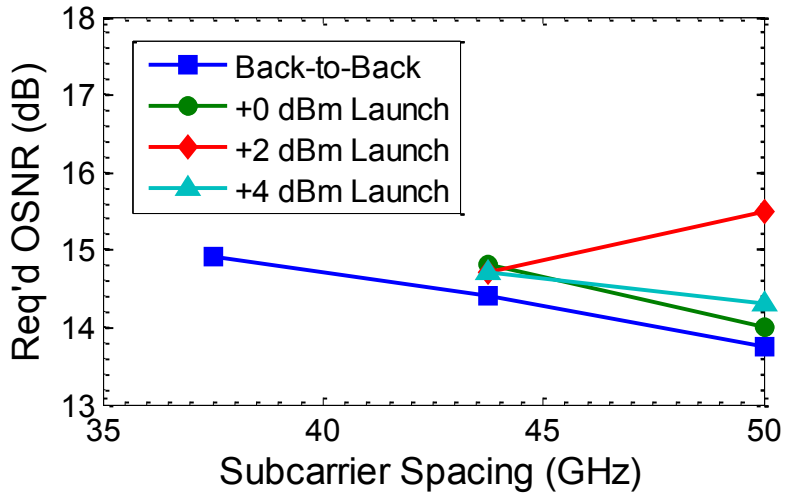


Figure 7.3. $OSNR_{req}$ after 1600 km loop transmission without per-subcarrier filtering. The legend indicates per-channel launch power.

per-subcarrier spacing. We determine the required OSNR for Q = 3 (BER = $1.3 \times 10^{-3}$) for each combination of per-subcarrier spacing and optical filtering.

Without per-subcarrier filtering, Fig. 7.3 the PDM-QPSK is highly sensitive to linear crosstalk (overlapping power spectra) due to dense subcarriers. Subcarrier spacing tighter than 43.75 GHz without filtering incurs penalties such that Q = 3 is not achievable after loop transmission. Back-to-back measurements show a 1.25 dB penalty at 37.5 GHz spacing, yet tighter spacing does not achieve Q = 3.

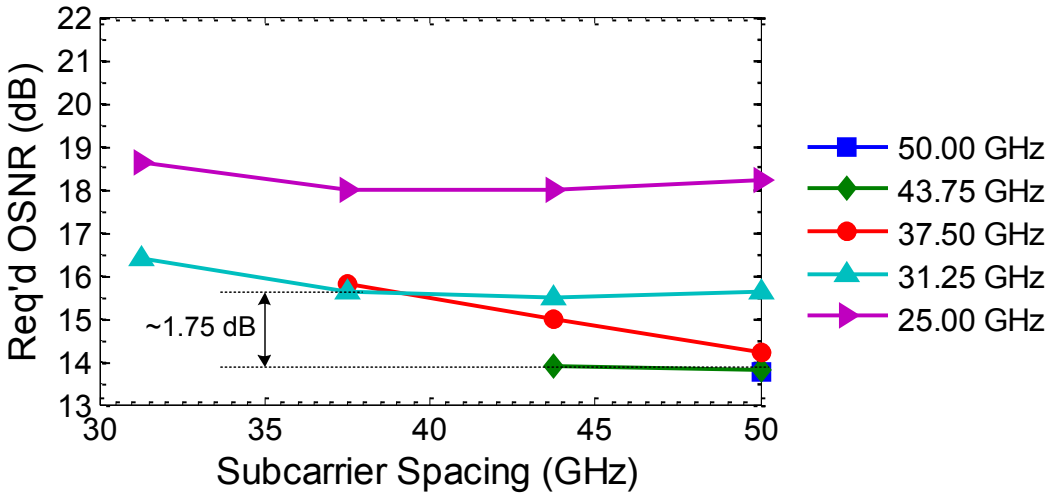


Figure 7.4. Performance of 32 Gbaud PDM-QPSK after filtering in a back-to-back configuration. The legend indicates the $WSS_2$ filter setting.

When the channels are filtered before multiplexing, significant performance improvements are realized, Fig. 7.4. In Fig. 7.3, we report ~1.75 dB penalty with 37.5 GHz subcarrier spacing and either a 31.25 GHz or 37.5 GHz optical filter compared to 50 GHz spacing and filtering (back-to-back).

The penalty for 37.5 GHz spacing increases by 1 dB after 1600 km loop transmission, Fig. 7.5. This subcarrier spacing corresponds to a 25% improvement in spectral efficiency (compared to standard 50 GHz spacing). Furthermore, both back-to-back and loop transmission cases demonstrate performance gains when moving from a 37.5 GHz filter to a 31.25 GHz filter when employing 37.5 GHz subcarrier spacing, which we attribute to the reduction in inter-subcarrier crosstalk. However, tighter filtering induces ISI, degrading system performance.

It is of particular note the improvement in system performance for 37.5 GHz subcarrier spacing when a 31.25 GHz optical filter is used. We observe OSNR transmission requirements near those of 43.75 and 50 GHz spacing. This implies that proper optical filtering reduces any *additional* penalty that may arise from crosstalk-nonlinear interactions (see §6.2) [113].

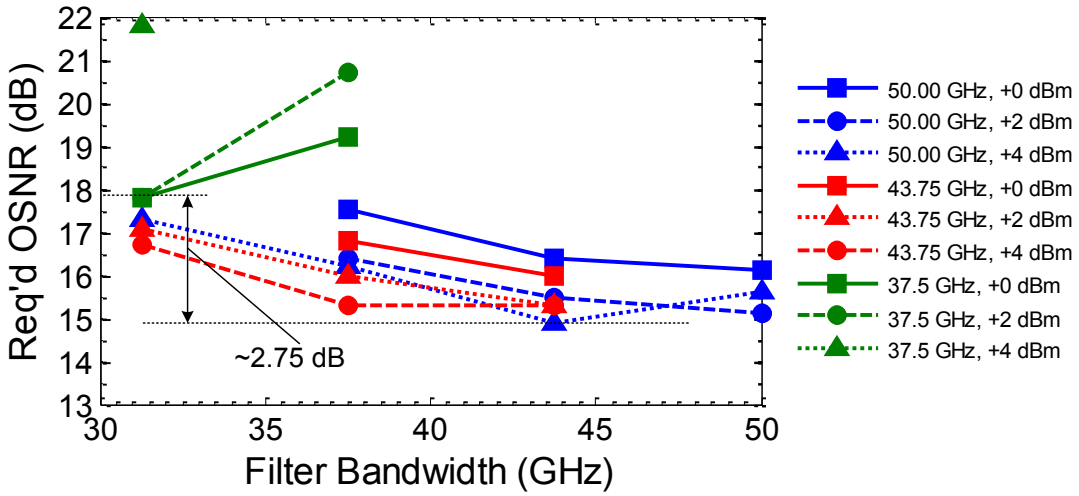


Figure 7.5. Performance of 32 Gbaud PDM-QPSK after filtering in a 1600 km loop transmission configuration. The legend in indicates subcarrier spacing and per-channel launch power.

### 7.2 Colorless Coherent Receivers for Gridless Optical Networks

In optical transmission networks with coherent receivers, optical filtering or demultiplexing is not strictly necessary to receive an individual channel. Channel selection can be achieved by tuning the LO near the desired frequency and followed by electronic filtering (either digitally or via the front-end bandwidth of the A/D). Together tunable LOs, coherent receivers, and DSP enable optical network deployments not constrained by static channel filters or specific grid assignments.

Ideally, balanced coherent receivers are naturally immune to common mode signals and thus do not produce photocurrents resulting from signal-signal and direct-detection interference. All out of band channels can therefore be easily discriminated by low pass filtering [10]. However these channels do produce a DC photocurrent which must be accommodated by the photodiodes and subsequent electronics. We note that single-ended photodiode based receivers can be useful as colorless receivers with proper limits on the number of channels [114]. Also, replacing the optical hybrid with a symmetric 3x3 optical hybrid using single-ended coherent detection effectively reduces the direct-detection terms [115], providing an effective solution

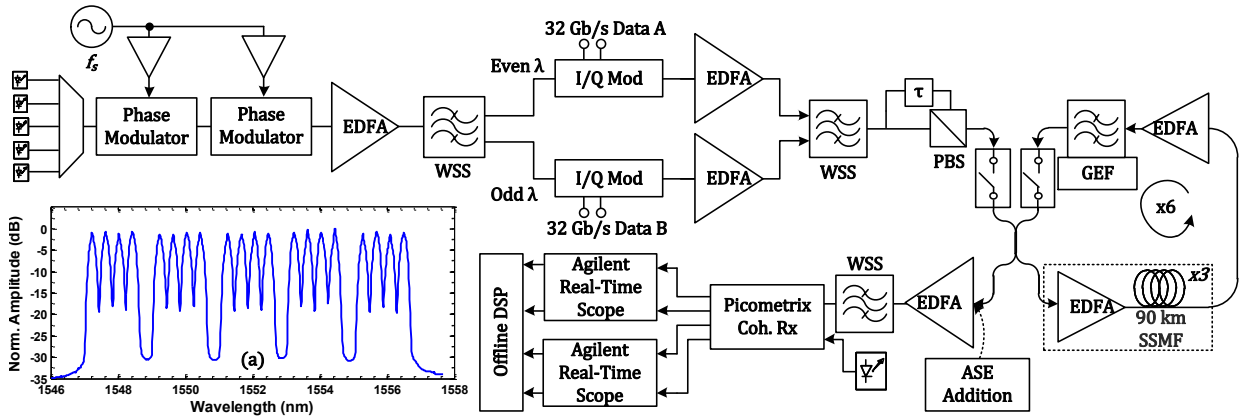


Figure 7.6. Experimental network configuration demonstrating generation and transmission of twenty 32 GBaud PDM-QPSK signals and colorless detection. Inset (a) depicts the power spectrum of the 32 Gbaud QPSK signals immediately after the polarization multiplexing.

without a balanced receiver. However, the full exploitation of colorless receiver capabilities has been limited by DC current capabilities and dynamic range of balanced coherent receivers.

Recently a new generation of receiver that is specifically designed to provide a large dynamic range and accommodate large DC photocurrents has become available. The new Picometrix CR-100D coherent receiver with Inphi TIAs is designed to support colorless applications. The receiver is constructed in the standard 2x2 optical hybrid configuration with balanced photodiodes, employing TIAs that support the high photocurrents required in a colorless network. We demonstrate colorless operation of this receiver with 32 GBaud PDM-QPSK in back-to-back and 1600 km transmission configurations with a range of received powers and WDM channels. We show <1 dB OSNR penalty for receiving up to 20 channels at once in both back-to-back and 1600 km cases

Our experimental setup is diagramed in Fig. 7.6. We multiplex 5 DFB and ECL lasers spaced 250 GHz apart. These laser carriers are modulated in two subsequent phase modulators driven by 25 GHz clock signals. After amplification a programmable WSS drops every other 25 GHz harmonic, then splits the remaining 50 GHz-spaced harmonics into even and odd sub groups. The even and odd harmonics are each independently modulated at 32 Gbaud in a

commercial LiNbO3 I/Q modulator. Another programmable WSS performs the 50/100 GHz interleaving and power equalization functions on the 32 Gbaud QPSK signals. Finally, all of the channels are polarization-division multiplexed (PDM) to generate twenty 32 Gbaud PDM-QPSK signals. Inset (a) of Fig. 7.6 depicts the PDM-QPSK channels after the polarization multiplex.

The PDM-QPSK channels are either transmitted back-to-back or loaded into a recirculating loop. The loop consists of three spans of SSMF (G.652) fiber with no inline dispersion compensation and all-EDFA amplification. Each of the three spans is nominally 90 km. A programmable WSS is used as a gain equalizing filter and to ensure the stability of loop transmission. The data circulates six times before unloading for a total of ~1620 km total transmission distance.

After transmission, the channels are received with a Picometrix CR-100D coherent receiver that utilizes the new Inphi high-current trans-impedance amplifiers (TIAs). This TIA offers wide dynamic range and high input current capabilities designed to support colorless 100G reconfigurable networks [116]. The electrical outputs of the TIAs are digitized using dual Agilent 80 GSa/s real-time oscilloscopes. The digital data is processed offline on a PC. Offline processing consists of six steps as described in detail in §3.1: (1) chromatic dispersion equalization, (2) asynchronous polarization demux, (3) timing recovery, (4) carrier-LO frequency offset estimation, (5) equalization, and (6) carrier phase recovery.

To establish baseline performance of the Picometrix CR-100D coherent receiver we configured the experimental network of Fig. 7.6 in a back-to-back setup. Using a programmable WSS we selected to receive either one, two, four, or twenty channels at once. We kept the per-channel receive power static at -10 dBm using a VOA and set the LO power to +13 dBm. The OSNR vs. BER performance of the center (1551.52 nm) channel for the one, two, four, and

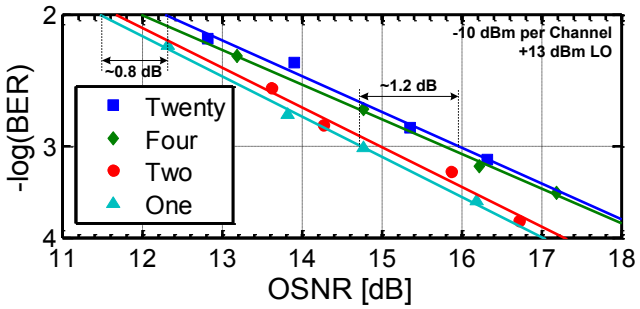


Figure 7.7. Back-to-back OSNR vs. BER of the center (1551.52 nm) channel with between one and twenty received channels.

twenty channel cases appears in Fig. 7.7. We observe <1 dB penalty at the target BER of $10^{-2}$. This small penalty is likely due to slight amounts of linear crosstalk for two reasons: (1) the four- and twenty-channel cases are nearly identical, and (2) the BER vs. OSNR scans at higher per-channel powers demonstrate performance of all channels within ±0.25 dB OSNR measurement error.

Next, we swept the per-channel receive power over a 10 dB range from -20 dBm to -10 dBm for the cases of one, two, and four receive channels. Additionally, we examined up to +9 dBm receive power for the single-channel case. The required OSNR for BER of $10^{-2}$ appears in Fig. 7.8a for these varying channel powers. We observe only slight variations of the required OSNR centered around 12 dB for any of the different receive channel amounts. Furthermore, there is no discernible penalty for single-channel received powers of up to +9 dBm.

In the last of our back-to-back experiments we received all twenty of the PDM-QPSK channels with a per-channel power of approximately -10 dBm (~3 dBm total receive power). We scanned the local oscillator to individually select each of the twenty channels for independent BER vs. OSNR examination. We show the required OSNR for BER $10^{-2}$ of all of the channels in Fig. 7.8b. This data reveals an approximately 1 dB variation over all of the channels which is likely due to imperfections of the polarization multiplex and power equalization steps in the experimental setup.

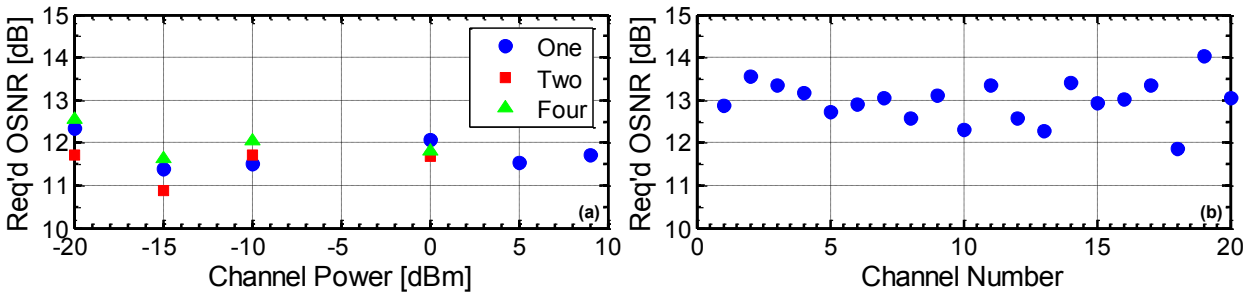


Figure 7.8. Back-to-back required OSNR for BER = $10^{-2}$ for (a) a range of per-channel power with one to four incident channels and (b) for all 20 channels with -10 dBm received power per channel.

In our transmission experiments we loaded all twenty channels into the recirculating loop diagramed in Fig. 7.6 and allowed the data to circulate six times for a total transmission distance of ~1600 km. The channels were each launched at nominally +0 dBm. However, over the distance of the transmission the non-flat gain spectrum of the EDFAs gave rise to an approximately ±1 dB variation in per-channel power (despite presence of the in-loop GEF). After transmission all twenty channels were received through a programmable WSS designed to emulate the in-network drop of a variable number of channels.

For each of one, two, four, or twenty drop channels we tested the per-channel receive power at -10 and -15 dBm (the LO was set at +13 dBm for all experiments). In each test we scanned the OSNR (while keeping the receive power constant) and determined the BER performance of the center (1551.52 nm, #10) channel only. The loop transmission results are shown in Fig. 7.9.

For -10 dBm per-channel received power we observe required OSNRs for BER = $10^{-2}$ within 0.5 dB of 13 dB for all numbers of received channels, Fig. 7.9a. This is exactly in the range of all required OSNRs computed for Fig. 7.8b, and represents an approximately 1 dB penalty against the individual channel's back-to-back performance (1551.52 nm, #10).

When the per-channel received power is set to -15 dBm we observe similar results, Fig. 7.9b. All variations in number of received channels yields required OSNRs slightly above 13 dB.

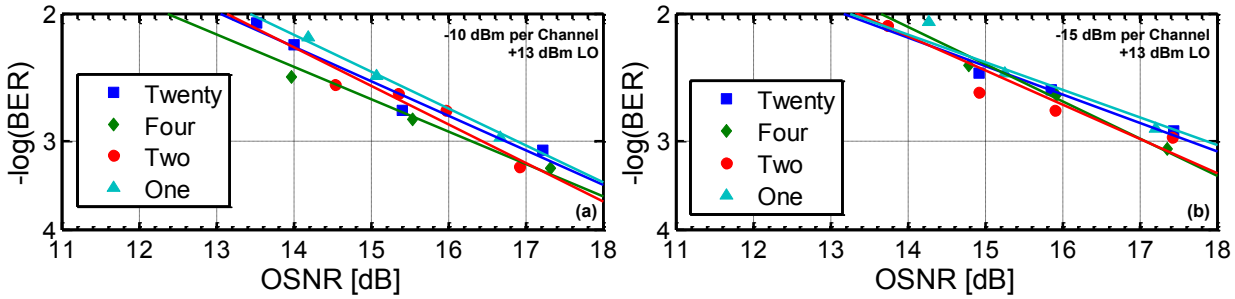


Figure 7.9. 1600 km loop transmission results with approximately +0 dBm launch power per channel using two different received powers: (a) -10 dBm per channel, and (b) -15 dBm per channel. For up to 20 channels the receiver demonstrates negligible performance differences at the $10^{-2}$ target BER.

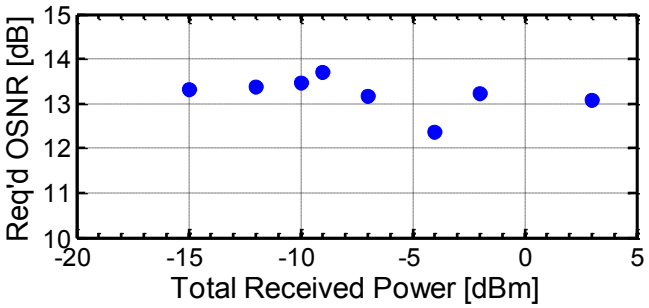


Figure 7.10. The $OSNR_{req}$ extracted from Fig. 7.9 (a) and (b) and plotted as function of total received power rather than per-channel received power.

For both cases of per-channel received power (-10 dBm and -15 dBm) the OSNR vs. BER performance differences for all numbers of received channels falls within the ±0.25 dB OSNR measurement uncertainty.

Each of the cases of per-channel received power and number of channels shown in Fig. 7.8(a) and (b) represents a different total received power. We therefore extracted the required OSNR for BER = $10^{-2}$ and recast the data as a function of total received power, shown in Fig. 7.10. For all total received power cases from -15 dBm to +3 dBm the required OSNR falls within ±0.5 dB of 13 dB (excepting the outlier at -4 dBm which is -0.6 dB down). This constant performance indicates robust receiver operation over a 20 dB range of total received power and demonstrates support for more than twenty received channels.

To conclude we have demonstrated the new Picometrix CR-100D coherent receiver in a 1600 km gridless transmission. Our results show a <1 dB required OSNR penalty for BER = $10^{-2}$ with up to twenty receive channels.

# CHAPTER 8

# MARGIN PREDICTION FOR 100G PDM-QPSK NETWORKS

Network scaling rules that enable the accurate prediction of system margins are critical to designing and deploying optimized high-speed WDM fiber networks [117] to meet traffic growth demands [118-120]. In addition to the variety of span lengths in existing networks there is a great variety of deployed fiber types. The three primary characteristics that define the fiber channel – loss, dispersion, and nonlinearity – are intrinsic to understanding how network performance scales with different fiber types.

Research over the last few years has demonstrated that uncompensated links offer performance advantages over dispersion-managed systems [121, 122] and that any network upgrades to or greenfield installations of coherent systems should adopt uncompensated transmission. Because of this seemingly inevitable move in the network much effort has been made to understand the theoretical and practical performance limits of uncompensated links. By doing so we hope to craft engineering rules to aid the design of future network deployments.

Specifically, theoretical modeling has sought to recast the traditional definition of SNR to include a nonlinear noise variance. The simplest approach is to add the nonlinear noise variance (however it may be derived) to the variance of the ASE yielding the form

$$\mathrm{SNR_{NL}} = \frac{A}{\sigma_{ASE}^2+\sigma_{NL}^2}. \tag{8.1}$$

This form implies a number of constraints on the variance of the nonlinear interference $\sigma_{NL}^2$; it must be statistically independent of the ASE (with variance $\sigma_{ASE}^2$ ) [36] and Gaussian distributed. Importantly, it has been shown that the signal components are statistically independent and Gaussian distributed both before and after DSP [123]. This behavior can be understood by considering that dispersion, particularly in uncompensated links, renders the 4 signal components as independent and noise-like.

FWM is the dominant, capacity-limiting nonlinear noise effect. In the highly dispersive regime, the FWM terms (of which XPM is a subset) that require phase-matching tend to be minimal due to channel walk-off. Since XPM appears as an ensemble average across all of the WDM channels in the set of *N* coupled Nonlinear Schrodinger equations that describe pulse propagation of each of *N* WDM channels and since the channels and individual components appear independent, it is possible to consider the nonlinearity statistically. Theoretically, XPM could be compensated if all of the WDM channels could be processed simultaneously, although in practice that is not possible.

Approximate expressions for $\sigma_{NL}^2$ have been developed by a number of methods. For example, using a "Gaussian Noise" (GN) model based on a FWM approach and relying the observation that after DSP the statistical distribution of received constellation points is Gaussian, Carena et al. [123] and Poggiolini et al. [124] developed integral expressions for the nonlinear interference. Experimental observations [125] of scaling with link length conform to a partially coherent addition of interference between spans.

Analytic expressions for maximum capacity and optimum launch power have been developed by Mecozzi et al [126] instead using a perturbation approach. One of the earliest efforts [127], expounded upon in [128] and in [130], derived an analytical expression for the

intensity fluctuations of XPM noise. Another derivation of (nonlinear) maximum capacity for various fiber types utilized the Volterra series expansion [131]

Despite different analytical approaches, there are striking commonalities among the models developed in [123], [124], [126], [127], [129], and [130] as well as the empirical models demonstrated in simulation and experiment in [131-133]. First, and as previously mentioned, they all develop a modification of the SNR definition to include nonlinear noise that takes the form $\mathrm{SNR_{NL}} = A/(\sigma_{ASE}^2 + \sigma_{NL}^2)$, Second, and in all cases, the variance of the nonlinear noise term is proportional to cube of the channel power, $P_{\mathrm{ch}}^3$, and the square of the nonlinear coefficient, $\gamma^2$. This result may be inescapable. FWM is a third-order Kerr-nonlinearity in silica fibers; it generates a fourth signal based upon the mixing products of three others, $f_g = f_i + f_j - f_k$, where the magnitude of the generated signal is proportional to $\gamma^2 P_i P_j P_k$ [134]. The nonlinear variance has also been shown to be inversely proportional to the absorption coefficient $\alpha$ and the dispersion coefficient $D$ [122, 36, 124-128]. It should therefore be possible to create design rules that allow for adaption of design solutions across networks with different fiber types.

In this work we experimentally quantify the system performance of a 1600km link comprised of one of three different fiber types: TrueWave REACH (G.655, MDF), AllWave (G.652, SMF), and ultra-large area fiber (LAF). For each fiber type we transmit seven PDM-QPSK channels, at 28 or 32 GBaud corresponding to the line rate needed to support hard- [50] and soft-FEC [51] BER limits. We quantify the BER vs. OSNR performance and compute the transmission penalty over a range of launch powers for each combination of baud rate and fiber type. We establish the link margins and identify the power corresponding to maximum link margin. Our results demonstrate that all of the fiber types tested support >1600 km transmission with robust margins at either the hard- or soft-FEC baud rate. SMF and LAF yield transmission

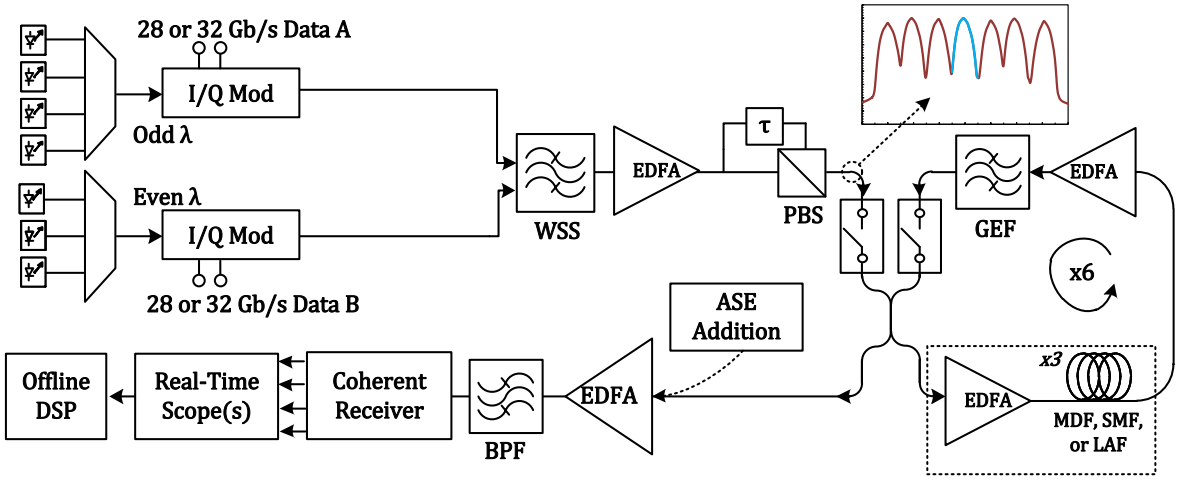


Figure 8.1. Experimental network configuration for seven-channel PDM-QPSK transmission. The network employs a recirculating loop of three spans of either MDF, SMF, or LAF fiber. The transmitted signal is received with a Picometrix coherent receiver and digitized on a real-time oscilloscope.

margins well above the requirements for 1600 km transmission, indicating their efficacy for ultra-long haul transmission or advanced modulation formats.

Using link margins we then determine how link capacity and optimum launch power scale with fiber parameters. Finally we show, for the first time, that link performance scales with fiber parameters $\alpha$, D, and $\gamma$ and as shown in (2) that scaling is consistent with the observation [123, 124] that the nonlinear interference can be modeled as excess Gaussian noise and hence can be simply added to the ASE noise as shown in Eq. (1).

## 8.1 Experimental Network Configuration

The PDM-QPSK test network consists of 7 channels on a 50GHz grid, a recirculating loop and a coherent receiver with custom demodulation, Fig. 8.1. Even and odd channels are modulated separately in independent commercial I/Q modulators (Oclaro) at either 28 or 32 Gb/s. After modulation all seven channels are interleaved with a commercial WSS (Nistica). The

Table 8.1. Nominal fiber parameters for seven-channel PDM-QPSK experiments

| PARAMETER | SMF | MDF | LAF |
|---|---|---|---|
| Loss, α [dB/km] | 0.19 | 0.21 | 0.18 |
| Core Effective Area, $A_{eff}$ [$\mu m^2$] | 80 | 55 | 130 |
| Dispersion, *D* [ps/nm-km] | 17.0 | 7.3 | 20 |
| Nonlinear Coef., γ ($x10^{-3}$) [$m^{-1}W^{-1}$] | 1.16 | 1.91 | .717 |

channels are then polarization multiplexed to form either 112 or 128 Gb/s data signals. The inset in Fig. 8.1 depicts the seven PDM-QPSK channels just before transmission.

For transmission, all seven channels are loaded into a recirculating loop comprised of three spans, all-EDFA amplification, and optical dispersion compensation. Each span is identically configured with either MDF, SMF, or LAF fiber and is nominally 90 km. Table 8.1 lists the fiber parameters. We circulate the data in the loop six times for a total transmission distance of ~1600 km. Once transmitted, the data is unloaded from the loop and the center channel is optically filtered and then detected by a Picometrix coherent receiver and then digitized.

WDM systems require optimization of both optical and electrical filters at the receiver to minimize inter-channel interference (ICI) without incurring significant ISI. Since we maintain a 50GHz channel separation for all the work reported here, there is minimal ICI and we choose a broad optical filter that will not induce any ISI. The electrical filters of the DSP generally attempt to create a matched filter and the hardware of the receiver should not restrict the electrical bandwidth to the point where it prevents the DSP from creating an optimized filter. We have found that the optimized electrical filter has a bandwidth of $> 0.6\,R_s$ [135]. Thus the 28 Gbaud signals require >16 GHz electrical bandwidth and the 32 Gbaud signals require >19 GHz.

For the both 28 Gbaud (32 Gbaud) we use a single (dual) Agilent oscilloscope operating at 1.4 samples-per-symbol. After digitization the data is processed offline on a PC.

Offline processing consists of six steps: (1) blind chromatic dispersion estimation, (2) asynchronous polarization demultiplexing, (3) symbol timing recovery, (4) carrier-LO frequency offset estimation, (5) LMS equalization, and (6) carrier phase estimation. Carrier phase estimation is performed using a variation of the Viterbi-Viterbi (power-of-four) method for QPSK that computes the filter taps based on a minimum mean-square error criterion for the phase of the symbols. The filter is kept at a static length of 19 symbols for all experiments. Details of our algorithm have been previously reported [63] and are available in §3.1.

For each loop configuration (different fiber type) and for each baud rate we varied the per-channel launch power from -6 dBm to +6 dBm. At each launch power we performed an OSNR vs. BER scan by loading ASE noise at the receiver. For the 28 GBaud tests we extracted the required OSNR to achieve the hard-FEC BER of $10^{-3}$ and for the 32 GBaud experiments we extracted the required OSNR for the soft-FEC BER limit of $10^{-2}$.

### 8.2 Results

The measured spectra of the PDM-QPSK signal provides an excellent metric for assessing the quality and reproducibility of transmitter performance as well as calibrating numerical simulations [137]. The properly optimized pulse carver provides a broader spectrum and slightly better performance overall, Fig. 8.2a. The slightly lower sidelobes apparent in the 32 GBaud spectrum are indicative of bandwidth capabilities of the I/Q modulators and pulse carver. The 50 GHz WSS filter, which is closely approximated with a $4^{th}$-order super-Gaussian shape, is seen to have negligible impact on the main lobe.

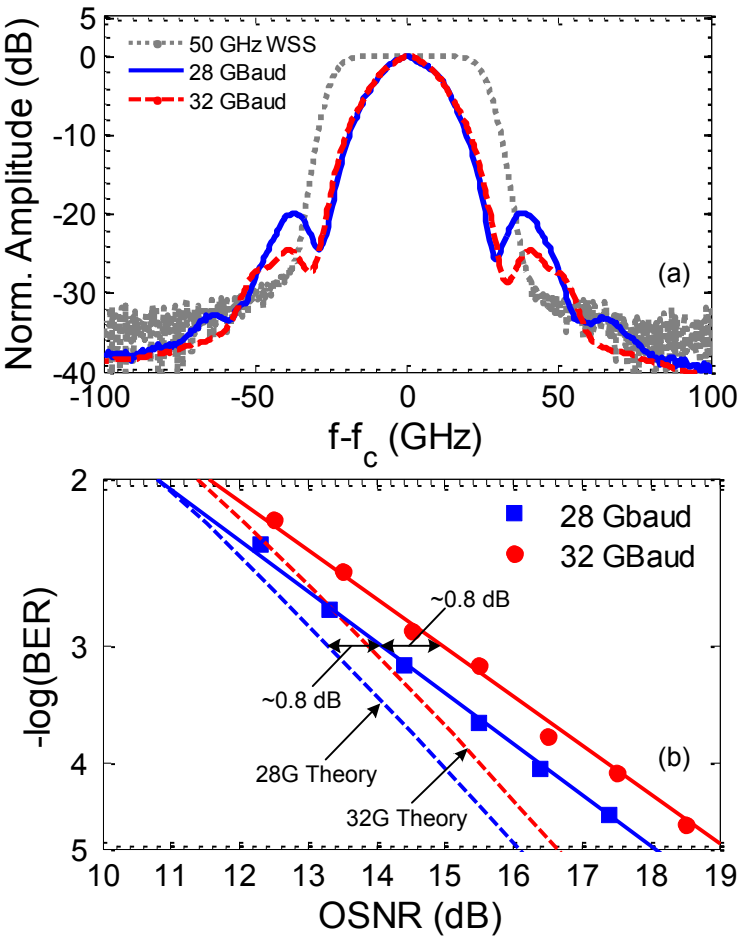


Figure 8.2. Back-to-back NRZ-PDM-QPSK spectra compared to the 50 GHz WSS filter and (b) back-to-back BER vs. OSNR performance comparison of 28 and 32 GBaud PDM-QPSK. The dashed lines indicates the theoretical OSNR performance of PDM-QPSK signals in an AWGN channel.

We first established the back-to-back baseline performance by evaluating the BER vs. OSNR at 28 and 32 GBaud, Fig. 8.2b. The 32 Gbaud PDM-QPSK signal achieves $10^{-2}$ BER at an OSNR of 11.6 dB, approximately 1 dB from the theoretical limit. The 28 Gbaud signal requires 14 dB OSNR to achieve a BER of $10^{-3}$, approximately 1.4 dB from the theoretical limit. We observe an ~0.8 dB penalty increasing the baud rate from 28 to 32 GBaud compared to the expected 0.6 dB. These results demonstrate the excellent performance of the transmitter, receiver and demodulation code in the linear regime.

The back-to-back BER vs. OSNR curves are fitted with on error function of the following form

$$\mathrm{p}_1\mathrm{OSNR}_{\mathrm{dB}} + p_2 = -10\log\{2\mathrm{erfc}^{-1}(2\cdot \mathrm{BER})^2\}, \quad (8.2)$$

where $p_1$ and $p_2$ are the fitting parameters (least-squares method). Equation (2) implies a linear relationship between OSNR on a dB scale and BER on an log+erfc scale (with the BER values descending) and comes from the analytic BER equation for QPSK, $\mathrm{BER}_{\mathrm{QPSK}} = 0.5\mathrm{erfc}\{\sqrt{SNR/2}\}$.. The multiplicative parameter $p_1$ determines the slope on a dB scale; it is accordingly an exponent on a linear scale. The second fitting parameter $p_2$ indicates an offset (in dB). For the 32 GBaud curve we find $[p_1\ p_2] = [-0.6881\ 0.5294]$ and for the 28 GBaud curve we find $[p_1\ p_2] = [-0.7069\ 0.1870]$. For comparison, the theoretical 32G and 28G curves have $[p_1\ p_2] = [-1.000\ 4.083]$ and $[p_1\ p_2] = [-1.000\ 3.503]$, respectively. Observe that the fitting parameters for the theoretical curves indicate only an offset, which comes from casting SNR to OSNR via the relationship $R_s/B_N$. That is $p_2$ can be computed from $10\log(32/12.5) = 4.08$ dB and $10\log(28/12.5) = 3.50$ dB for 32G and 28G formats, respectively.

We note that the experimental data reveals both a shallower slope and a slight offset compared to the theoretical curves. The OSNR offset can be attributed to the limited extinction ratio of the $LiNbO_3$ I/Q modulator; a finite extinction ratio appears directly as a power penalty $(r_e + 1)/(r_e - 1)$. The slope of the BER curve is determined by the bandwidth limitations of the modulator electro-optic response and the A/D front-end filter. Together the extinction ratio and filtering determine the digital pulse shape. Lastly, we recognize that the curve fit implies that the theoretical and experimental data will cross around the $10^{-2}$ BER point. This characteristic is clearly non-physical and therefore limits the applicability of the fit to the ~7 dB range of OSNR

values from 12 to 19 dB and to the three decades of BER from $10^{-2}$ to $10^{-5}$. Nevertheless, these curves fits play a critical role in correctly calibrating the nonlinear interference calculations in §8.3.

For the 1600km loop transmission performance we observe a smooth transition from the linear to nonlinear regime as launch power is increased for all 3 fiber types and for both baud rates, Figs. 8.3a and 8.3b. The data points represent measured results. The solid lines are computed using the NLI model of [3], which is described in detail in §8.3. The observed ~1.5-2 dB transmission advantage for SMF and LAF in the linear regime (for both 32 and 28 Gbaud) corresponds to their lower per-span loss compared to MDF. From Table 8.1 we expect 18.9 dB of loss for 90 km of MDF and 17.1 dB of loss for 90km of SMF. In our experiments we achieve ~20 dB and ~18 dB, respectively, due to monitoring taps at both the input and output of the inline amplifiers. While the dB/km loss coefficient of LAF is lower than in SMF, the splice losses between the LAF to SSMF jumper cables yield per-span losses nearly identical to SMF. Therefore the ASE-dominated linear transmission regime performance is identical in SMF and LAF. However, the measured BER minima that marks the transition into the nonlinear regime occurs at a higher per-channel launch power in LAF as expected from the lower nonlinear coefficient.

The minimum observed BER occurs at -2, -0.5, and +1 dBm launch power for MDF, SMF, and LAF, respectively, at the 32 GHz baud rate. At 28 Gbaud, the BER minimums occur at -2, -0.25, and +0.5 dBm, respectively. Once in the nonlinear regime our transmission experiments yield a 3-3.5 dB advantage for SMF over MDF. We also observe a ~2-2.5 dB advantage for LAF over SMF. These relative performance differences are observed for both 28 and 32 GBaud signals.

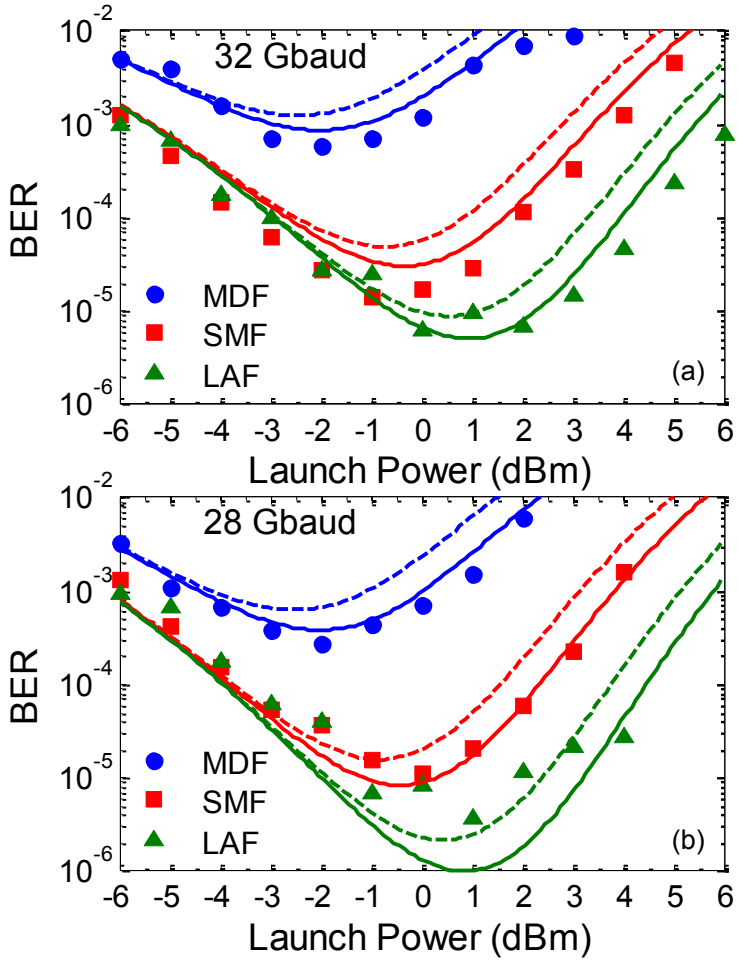


Figure 8.3. 1600 km transmission results for PM-QPSK at (a) 28 and (b) 32 Gbaud as a function of per-channel launch power with MDF, SMF, and ULA fiber types. The solid and dashed lines are theoretical margin calculations using the definition of nonlinear SNR in Eqns. (8.3-8.5) for incoherent and coherent noise accumulation, respectively.

A complimentary figure of merit to BER performance for link transmission is the OSNR *penalty* defined as the difference between the required OSNR after link transmission and the back-to-back required OSNR for the same BER. The OSNR transmission penalties for 32 and 28 GBaud appear in Figs. 8.4(a) and (b), respectively. In linear regimes the OSNR penalty is characteristically small. Indeed, the penalty is negligible for launch power less than -3dBm for both SMF and LAF fiber. We also observe that for all launch powers smaller than the BER minimum point, the OSNR penalty is less than 1 dB. As the link enters the nonlinear regime the OSNR penalty increases exponentially with increasing power. The exponential increase

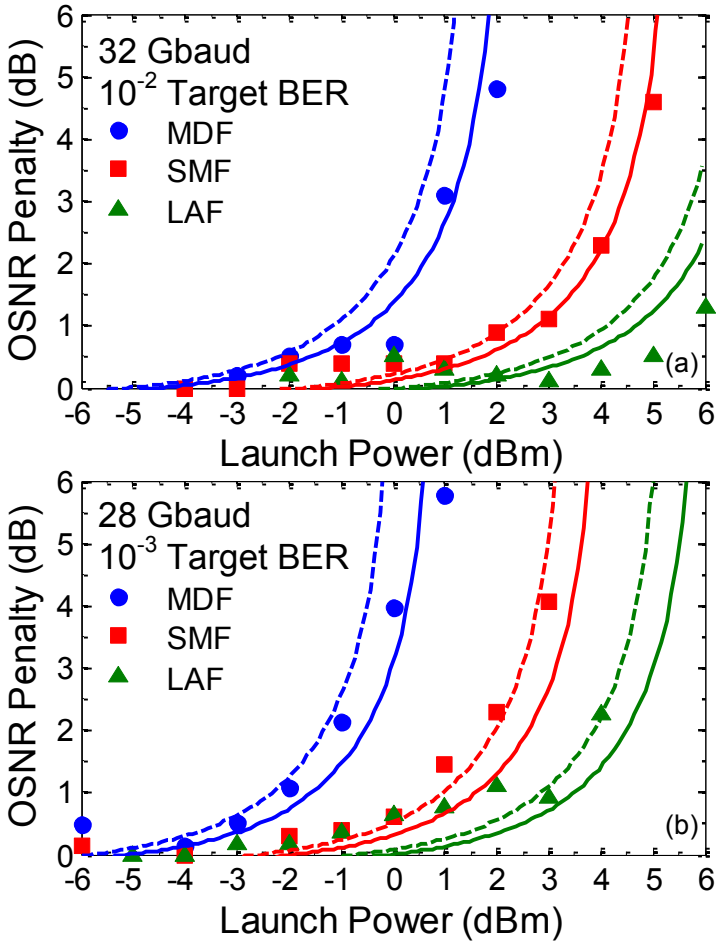


Figure 8.4. OSNR penalty results after 1600 km transmission for (a) 28 and (b) 32 GHz baud rates as a function of per-channel launch power with MDF, SMF, and ULA fiber types. The solid and dashed lines are theoretical margin calculations using the definition of nonlinear SNR in Eqns. (8.3-8.5) for incoherent and coherent noise accumulation, respectively.

$a\exp\{bx\}$ is characterized by a common (linear) exponent of $b{\sim}0.616$, where $x$ is the launch power in dBm and $a$ is a scalar offset. The penalties (of each baud rate) are offset by approximately 3 dB in launch power.

In the assessment of any link and to understand scaling behavior it is useful to be able to extract the contribution of the nonlinear noise, i.e. we seek to determine $\sigma_{NL}^2$ of Eqn. 8.1 from experimental results. First we recognize that at any operating point (launch power) the performance is determined by the available OSNR (i.e. the SNR is that given by Eqn. 8.1).

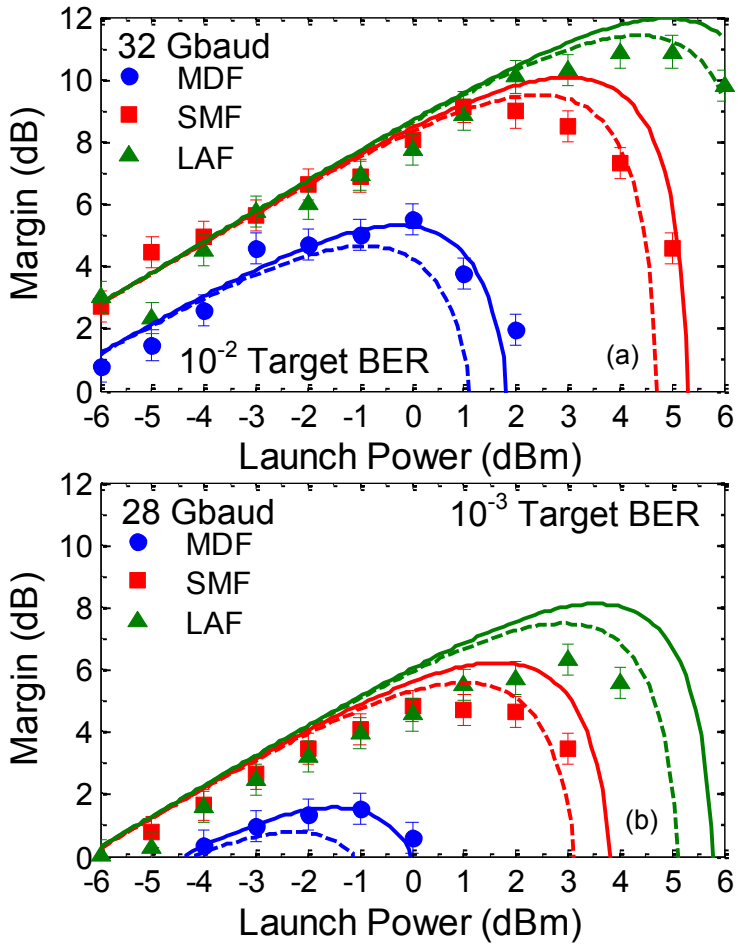


Figure 8.5. OSNR Margin after 1600 km transmission for (a) 32 and (b) 28 GHz baud rates as a function of per-channel launch power for MDF, SMF, and ULA fiber types. The solid and dashed lines are theoretical margin calculations using the definition of nonlinear SNR in Eqns. (8.3-8.5) for incoherent and coherent noise accumulation, respectively. Note that the maximum margin launch powers do not necessarily correspond to the launch powers that yield minimum BER from Fig. 8.3. The error bars indicate 0.5 dB variability in the margin determination.

We define link *margin* as the difference between the required OSNR for a particular BER and the maximum achievable OSNR. In a purely linear system the link margin increases 1 dB for every 1 dB increase in launch power independent of fiber type, since there is a 1 dB increase in OSNR for each 1 dB increase in launch power. 28 Gbaud channels operating at the hard-FEC limit, have a link margin >1.75 dB for all fiber types, Fig. 8.5a. We observe that MDF demonstrates an ~1.75 dB margin at -1 dBm launch power and SMF and LAF yield 4.75 dB and 6 dB maximum transmission margins, respectively. The linear regime extends to -2dBm for

MDF +1 dBm for SMF, and +4dBm for LAF, Fig. 8.5a. The margin then increases sublinearly up to the peak margin and then decreases with increasing launch power. The 1600 km MDF link has a maximum margin of ~5 dB near -0.5 dBm launch power. LAF achieves ~10 dB (maximum) margin at +4.5 dBm launch power. We note that for all cases the launch power that yields maximum margin does not necessarily correspond to the launch power of lowest BER performance.

### 8.3 Discussion

In the assessment of any link and to understand scaling behavior it is useful to be able to extract the contribution of the nonlinear noise; we seek to determine $\sigma_{\mathrm{NL}}^2$ from experimental results. We recognize that at any operating point (launch power) the performance is determine by the available OSNR, i.e. the SNR that given by Eqn. (8.1). We can recast Eqn. (8.1) in terms of signal and noise powers

$$\mathrm{OSNR_{NL}} = \frac{\mathrm{P_{sig}}}{\mathrm{P_{ASE}+P_{NLI}}}, \tag{8.3}$$

where $P_{\mathrm{sig}}$ is the per-channel launch power, $P_{\mathrm{ASE,link}}$ is the power of the ASE at the end of the link. We note here that this $\mathrm{SNR_{NL}}$ model contains only the ASE and NLI; linear crosstalk and ISI are other prominent impairments in many link configurations. However, our 50-GHz channel spacing ensures negligible linear crosstalk; ISI and other noise sources is calibrated using the fitting parameters of the back-to-back data explained shortly. Using the model developed in [3]

$$P_{NLI} = G_{NLI} N_s^{1+\epsilon}, \tag{8.4}$$

where

$$G_{NLI} = \left(\frac{2}{3}\right)^3 \frac{\mathrm{G_{WDM}^3}\gamma^2}{2\pi\alpha\beta_2} \ln\left\{\frac{\pi^2\beta_2}{2\alpha} B_{ch}^2 N_s^{2B_{ch}/\Delta f}\right\} \tag{8.5}$$

is the power spectrum of the nonlinear interference and

$$\epsilon = \frac{3}{10}\ln\left\{1 + \frac{6L_{\text{eff,a}}}{L_s \operatorname{asinh}\left\{\frac{\pi^2}{2}L_{\text{eff,a}}\beta_2 B_{ch}^2 N_s^{2B_{ch}/\Delta f}\right\}}\right\} \tag{8.6}$$

accounts for the coherent accumulation of nonlinear noise. $G_{\text{WDM}}$ is the power spectrum of the total WDM signal. For incoherent noise addition $\epsilon = 0$. In Eqns. (8.5) and (8.6) $B_{ch}$is the per-channel bandwidth, $L_s$ is the span length, $N_s$ is the number of spans, $\Delta f$ is the WDM channel spacing, $L_{\text{eff}} = (1 - \exp\{-2\alpha L_s N_s\})/2\alpha$ is the effective length, and $L_{\text{eff,a}} = 1\backslash 2\alpha$ is the asymptotic effective length.

In an ideal link (AWGN channel with matched filtering) we could compute $\text{OSNR}_{\text{NL}}$ using (8.5) and (8.6) and then determine the BER from the analytic definition

$$\text{BER}_{\text{QPSK}} = \frac{1}{2}\text{erfc}\left\{\sqrt{SNR/2}\right\}. \tag{8.7}$$

However, and as demonstrated in the back-to-back experimental data, our link does not conform to this relationship because of the imperfect response of the modulator. Using the fitting parameters calculated for the back-to-back data we computed the BER for the computed $\text{OSNR}_{\text{NL}}$ from (8.3)-(8.6), Fig. 8.3. That is, we determined the theoretical $\text{OSNR}_{\text{NL}}$ for each launch power using the known link characteristics and then computed the BER from (8.2). The dashed lines are for coherent NLI accumulation (32G: $\epsilon = 0.089$; 28G: $\epsilon = 0.101$) and the solid lines are for incoherent NLI accumulation.

The theoretical calculations reveal excellent adherence to the experimental data. We observe that the experimental and theoretical BER minimums occur near the same launch power. The linear and nonlinear regimes also demonstrate nearly identical BER slopes. We note a slight discrepancy between LAF experimental and theoretical BER minimums at 28 Gbaud. Nevertheless the linear and nonlinear regime data follows the theoretically-predicated trends.

The theoretical OSNR penalty predictions, Fig. 8.4, utilize the same fitting data to re-cast the computed required OSNR into our link performance. As in the BER vs. launch power figures, the dashed lines are for coherent NLI accumulation and the solid lines are for incoherent NLI. We observe that the experimental data falls between the theoretical coherent and incoherent penalties for nearly all launch power case and for both 28 and 32 GHz baud rates.

Link margin is the difference between the total available system SNR and a SNR needed to achieve a desired BER. Written formally (linear),

$$\text{Margin} = \frac{\text{SNR}_{\text{available}}}{\text{SNR}_{\text{desired}}}. \tag{8.8}$$

The practicalities of measuring an optical signal with an optical spectrum analyzer (OSA) make it important to understand this definition precisely. After transmission, and written in a longer fashion (and in dB), the margin definition is

$$\text{Margin[dB]} = \text{OSNR}_{\text{max}}\text{[dB]} - \left(\frac{P_{\text{sig}}}{P_{\text{ASE}}+P_{\text{ASE,added}}+P_{\text{NLI}}}\right)_{\text{dB}}, \tag{8.9}$$

where $P_{\text{ASE,added}}$ is the amount of ASE added to get the desired BER. An OSA can only measure $P_{\text{sig}}/(P_{\text{ASE}} + P_{\text{ASE,added}})$ – it cannot "see" the NLI. Therefore any computation of NLI made for comparison must take limitation into account. The second term on the right of Eqn. (8.9) is the required OSNR. Since the desired SNR is that which achieves a particular BER then we can write extract from the back-to-back curves (Fig. 8.2b) $\text{OSNR}_{\text{desired}} = 11.6$ dB or 14.1 dB for 32 and 28 GHz baud rates, respectively. And as we have discussed, for the case of optical transport in uncompensated regimes, the total SNR *available* is $\text{SNR}_{\text{NL}}$ given in (8.1) – that is, the SNR including any nonlinear effects. The link $\text{OSNR}_{\text{desired}}$can be written as

$$\text{OSNR}_{\text{desired}} = \frac{P_{\text{sig}}}{P_{\text{ASE}}+P_{\text{ASE,added}}+P_{\text{NLI}}}, \tag{8.10}$$

and therefore

$$P_{\mathrm{ASE,added}} = P_{\mathrm{sig}}/\mathrm{OSNR}_{\mathrm{desired}} - P_{\mathrm{ASE}} - P_{\mathrm{NLI}}. \quad (8.11)$$

Using Eqns. (8.9-8.11) we computed the theoretical margin for the six cases of our experiments (SMF, MDF, or LAF with 32 or 28 GBaud channels). These computations appear as the solid lines in the margin plots, Fig. 8.5. We observe excellent adherence of our data to the theoretical curves. We also note that the margin calculations contain no free "fitting" parameters – the link characteristics were simply plugged into Eqns. (8.3-8.5). As expected, the margin curves exhibit a 1dB/dB linear slope for low launch powers. As the launch power increases the nonlinear noise increase and the margin curve slowly bends to reach zero slope, after which it begins decreasing

As discussed in the introduction and shown in (8.8), the models developed in [36], [124], [126], [127], [129], and [130] for the variance of the nonlinear interference all contain a $\gamma^2 P_{ch}^3$ term. The differences in models, however, yield slightly different proportionalities of the variance. Nevertheless, the similarities among the models and the definition of FWM mixing strongly suggest that the power that achieves maximum capacity follows the proportionality relationship

$$P_{\max} \propto \left(\frac{\alpha|D|}{\gamma^2}\right)^{1/3}, \quad (8.12)$$

after applying the definition $D = -2\pi c\beta_2/\lambda^2$ and when viewed independently from baud rate. That is, the launch power that achieves maximum link capacity is solely determined by the parameters that describe the particular fiber optical cable – loss, dispersion, and nonlinearity.

We are careful to note that each of the models [36, 124, 126-129] make the following identical assumptions to arrive at (8.5): a WDM link with channels of identical modulation and baud rate no inline dispersion compensation, and sinc pulses. Our transmission experiments do employ WDM channels with identical modulation format and no inline compensation. However, our transmission signals do not have perfect sinc pulses. The model in [126] requires Raman

amplification and amplitude-only modulation although the models in [36, 127-130] use EDFA-only amplification and support any modulation format.

Nevertheless we closely meet the parameter requirements of the XPM variance approximations from [126] used to generate (8.5) for the following reasons. RZ carving ensures amplitude modulation by enforcing every symbol transition to pass through zero amplitude. Raman amplification appears in the computation of the XPM variance only a scale factor; XPM interactions are identical whether or not they occur along the length of the span or mostly at the beginning. Also, the variance approximation is appropriate for $L/z_d > 50$, where $L$ is the total link length, and $z_d = T^2/2\pi\beta_2$ is the dispersion length. Furthermore, the derivations in [36], [124], and [129] were made for EDFA-based links with phase-based modulation formats.

Finally, we performed several integral calculations from Eqn. (8.5) to demonstrate the shape of the nonlinear noise for 32 GBaud PDM-QPSK transmission, Fig. 8.6. Figure 8.6(b) with NRZ/RZ channels mirrors the experimental setup in Fig. 8.1. We observe that the nonlinear noise, in general, follows the shape of the aggregate WDM signal. That is, the nonlinear noise is distinctly colored for these three cases of non Nyquist-WDM transmission.

## 8.4 Conclusion

We have compared the transmission performance 28 and 32 GBaud PDM-QPSK which correspond to the hard and soft-FEC target baud rates in an all-EDFA recirculating loop of ~1600 km. Our experiments enable direct comparison of SMF, MDF, and ULA fiber types at both baud rates. Our results reveal that each fiber type yields robust margins >5 dB at the $10^{-2}$ soft-FEC limit, demonstrating efficacy for >1600 km transmission. Furthermore, the industrial

margins of >8 dB of both SMF and LAF will enable more advanced modulation formats that future networks will require.

Our experimental method isolated the fiber transmission performance by using a static amplification scheme and transmitter structure for each fiber type and baud rate. Consequently, our computed link margin directly describes the fiber-determined transmission capability at a given operating point. The launch power that yields maximum margin represents the optimum operating point. The optimum launch power to achieve maximum system margin for any combination of $P_{\text{launch}}$, $\alpha$, $\gamma$, and $D$ with PDM-QPSK channels can be predicted for systems with no inline dispersion compensation with the NLI computations and GN model, Eqns. (8.3)-(8.6), and provide a convenient way of predicting total system margin and its associated optimum launch power

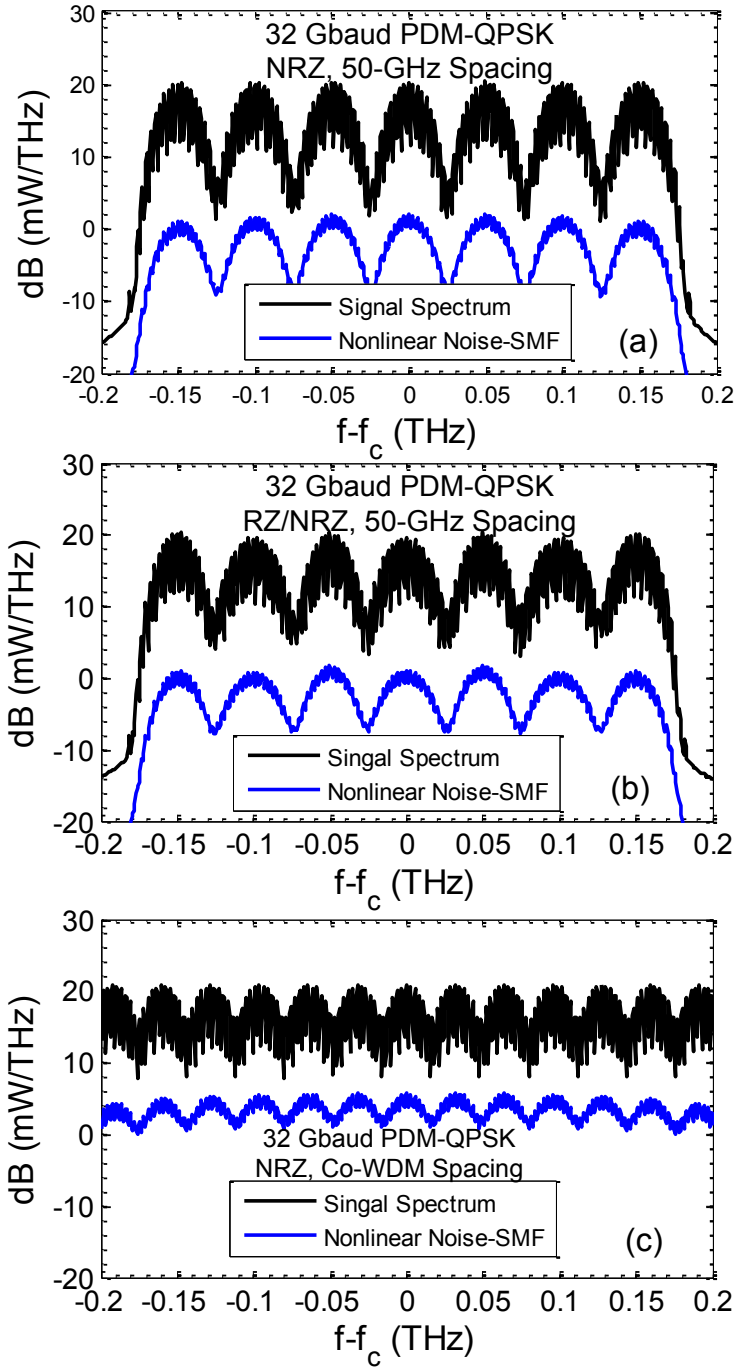


Figure. 8.6. Nonlinear noise calculations for +2 dBm launch power per channel, 32 Gbaud PDM-QPSK with (a) NRZ signaling on a 50 GHz grid, (b) NRZ/RZ signaling on a 50 GHz grid, and (c) NRZ signaling and Co-WDM baud-rate spacing.

# CHAPTER 9

# 16QAM FOR NEXT-GENERATION OPTICAL TRANSPORT

Sixteen-ary QAM is the next most logical step in modulation format from QPSK to meet increasing SE demands [141-143]. It can be generated simply in the same I/Q modulator structure as QPSK (see Fig. 2.2) by applying a four-level electrical drive signal. Winzer et al [141] demonstrated 14 Gbaud 16 QAM (112 Gb/s) on a 16.7 GHz grid over 630 km transmission using hybrid Raman/EDFA amplification. In follow-up work [142], the authors employed 28 Gbaud 16 QAM (224 Gb/s) in a hybrid Raman/EDFA link over 1200 km on a 50 GHz grid. Another effort [144] computed optimum 16 QAM constellations in for a combination pure phase noise or Gaussian noise. Huang et al [143] utilized 16 QAM in all-optical orthogonal frequency division multiplexing (OFDM) with 15 phase-locked subcarriers to construct a 1.5 Tb/s super channel and transmitted it over 1200 km. An extensive simulation effort [52] identified filter and bandwidth penalties for several modulation formats (including 16QAM) in a Co-WDM link arrangement. However, much work remains to experimentally craft guidelines for 16 QAM transmission – especially for how filter bandwidth, baud rate, signal processing, and subcarrier spacing trade-offs influence nonlinear or near-nonlinear regime transmission performance.

The following three sections contain experiments with PDM-16QAM signaling to address these outstanding issues. The first section presents a careful study of popular algorithms for 16QAM demodulation, with particular attention paid to polarization demultiplexing and equalization strategies. The next section reports a set of experiments that analyzed 16QAM

transmission in a heterogeneous network environment, that is, with adjacent channels of different modulation format. The final section adapts the nonlinear interference analysis of §8.3 to the case of PDM-16QAM transmission over several fiber types.

### 9.1. Comparison of DSP Architectures

Digital signal processing for 16QAM must compensate for the same impairments as for QPSK – CD, asynchronous sampling, polarization mode mixing, carrier frequency offset, and ISI. Algorithms for CD equalization, timing recovery, and frequency offset estimation in QPSK can be directly applied to 16QAM. However, the important steps of polarization demultiplexing, carrier recovery, and ISI equalization require small-to-large adaption for optimum performance; many different algorithms have been discussed [141, 145-147]. We compare two distinct polarization demultiplexing schemes and two equalization schemes for dual-pol 16QAM using experimental data after 100 km transmission. We propose an independent component analysis (ICA) polarization demultiplex with per-polarization LMS equalization for implementation simplicity and best performance.

To demodulate a PDM-16QAM signal after transmission in a fiber medium the DSP must, in general, perform CD compensation, extract the timing phase, separate the polarizations, and recover the carrier. We investigate two distinct DSP architectures for demodulation 16QAM and two variations for each architecture, Fig. 9.1. For all four cases (referred to as “Demod 1”, “2”, “3”, and “4”) we perform sampling skew removal and CD equalization first. We estimate the accrued chromatic dispersion in a blind fashion by minimizing the square-amplitude deviation from the mean of the received signal [56]. After CD compensation, Demod 1 & 2 perform timing recovery via the common digital square and filter method [62] and then separate

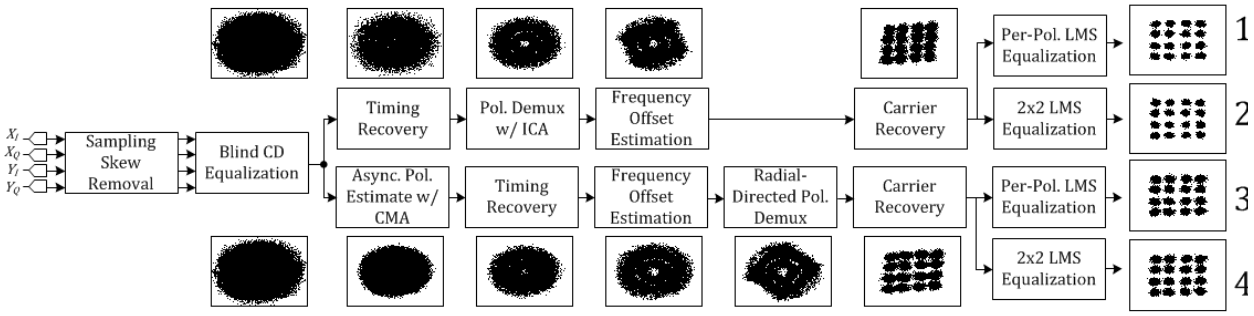


Figure 9.1. DSP flow of the four architectures investigated in this work along with example constellations after each processing step.

the polarizations with ICA. See §3.2.1 for details of the ICA-base polarization demultiplexing algorithm.

The next steps in Demod 1 & 2 are frequency offset estimation and carrier recovery. Carrier recovery is accomplished derived from the "stop-and-go" decision-directed algorithm described in [67, 68] (see §3.2.2). This algorithm employs a recovery loop to estimate the carrier phase with the rule $\theta_{k+1} = \theta_k - \mu_\theta \mathrm{Im}\{z_k e_k^*\}$, where is where $\theta_k$ is the phase estimate, $z_k$ are the message symbols, $\mu_\theta$ is the step size parameter, and $e_k = z_k - a_k$ is the error signal. Typically, $\mu_\theta$ is chosen to be around $10^{-2}$. After carrier recovery, Demod 1 employs a per-polarization LMS equalizer with 121 taps and Demod 2 employs a 2x2 (MIMO or "butterfly") LMS equalizer (of variable number of taps) to remove any residual inter-symbol interference before pattern synchronization and BER evaluation

The primary difference between Demod 1& 2 and Demod 3 & 4 is the polarization demultiplexing technique. In Demod 3 & 4 we employ an asynchronous constant modulus algorithm (CMA) equalizer to provide a first estimate of the state of polarization. The CMA is sub-optimum for 16QAM; unlike QPSK, 16QAM is comprised of three distinct rings, or moduli. After timing recovery and frequency offset estimation, Demod 3 & 4 utilize a radius-direction algorithm to complete the polarization mode separation. The RD algorithm attempts to exploit

the three-ringed character of 16QAM by enforcing this constraint on the non-separated symbols. As in Demod 1 & 2, Demod 3 & 4 are distinguished by the final LMs equalizer; Demod 3 employs the equalizer on a per-polarization basis (121 taps) and Demod 4 employs a 2x2 LMS equalizer (variable number of taps).

The PDM-16QAM test network consists of 20 channels arranged on a 25 GHz grid, a recirculating loop, and a coherent receiver, Fig. 9.2. The WDM signal is generated by first modulating two lasers (separated by 250 GHz) in an I/Q modulator driven by a 16 GBaud 4-level electrical signal. We add two binary electrical data streams in a passive coupler to create each four-level data signal and then amplify to approximately $V_{pi}$ with ultra-linear electrical amplifiers. Driving the I/Q modulator at $V_{pi}$ ensures operation within the mostly-linear regime of the sinusoidal MZM transfer function. We keep the baud rate at 16 GHz to minimize the implementation penalty (filtering & reflections) for best comparison of the demodulation routines. The two 16QAM signals are separated with a commercial WSS at the output of the modulator. The lower-wavelength channel is sent through a recirculating frequency shifter tuned to generate 20 copies (which are also delayed with respect to each other by the length of the fiber in the loop) on a 25 GHz grid. The channels of the frequency shifter are recombined with the signal that did not pass through the shifter in a WSS, which replaces the center (10th) channel. This WSS is also programmed to equalize the per-channel power to within ±1 dB. The twenty 16QAM signals are finally polarization multiplexed for a total data rate of 20·128 Gb/s = 2.56 Tb/s over 500 GHz of bandwidth which equates to a payload spectral efficiency of 4 b/s/Hz.

After the pol-mux, the WDM signal is loaded into a recirculating loop. The loop consists of three identical spans of 88 km of large-area fiber (LAF) and all-EDFA amplification. The LAF has parameters $\alpha \sim .18\ \mathrm{dB/km}$, $A_{\mathrm{eff}} \sim 130\ \mu\mathrm{m}^2$, and $D \sim 20\ \mathrm{ps/nm \cdot km}$. The recirculating

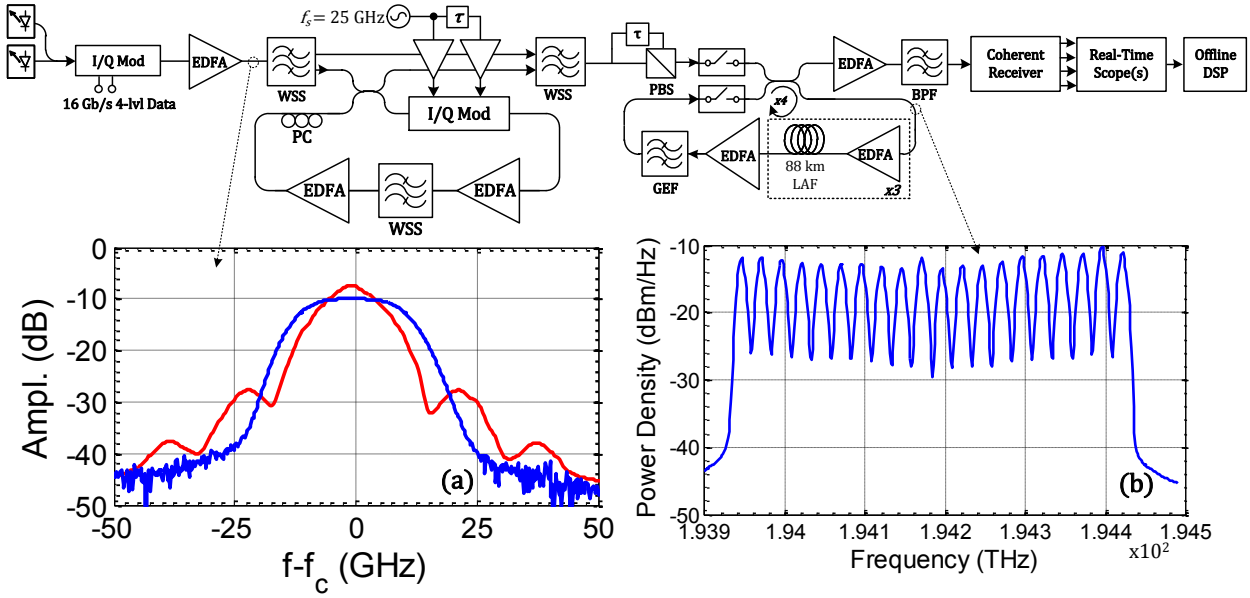


Figure 9.2. Experimental network configuration of a 20-channel PDM-16QAM system. The network employs a recirculating frequency shifter to generate 20 copies of the 16QAM signal and a recirculating loop of EDFA-amplified LAF spans. The 16QAM signal compared to the 25 GHz channel filter appears in inset (a). Inset (b) shows the 20 channel WDM signal as it is launched into the loop.

loop also incorporates a commercial WSS configured as a gain-equalizing filter (GEF). After transmission, the data is unloaded from the loop and detected with a Picometrix coherent receiver and then digitized at 80 GS/s with two synchronized Agilent real-time oscilloscopes. Finally, the samples are loaded onto a PC for offline processing in Matlab as described in previous section. We scanned the per-launch power from -4 dBm to +4 dBm. For each launch power we measured the BER vs. OSNR performance of the center PDM-16QAM signal by adding noise at the receiver. We then extracted the required OSNR for a BER = $10^{-2}$ per the soft-FEC requirement the 16 GHz baud rate enables (for a 100G payload).

We first measured the back-to-back BER vs. OSNR performance of the 16 GBaud PDM-16QAM signal with each of the four demodulation routines, Fig. 9.3(a). We also scanned the number of taps in the 2x2 LMS equalizer from 31 to 91 for Demod 2 & 4. Around $10^{-2}$ BER we observe an approximately 0.6 dB variation over the range of tap lengths. This variation expands to ~2 dB at BER=$10^{-3}$ and ~3.1 dB at BER = $10^{-4}$. The best-performing configuration of the

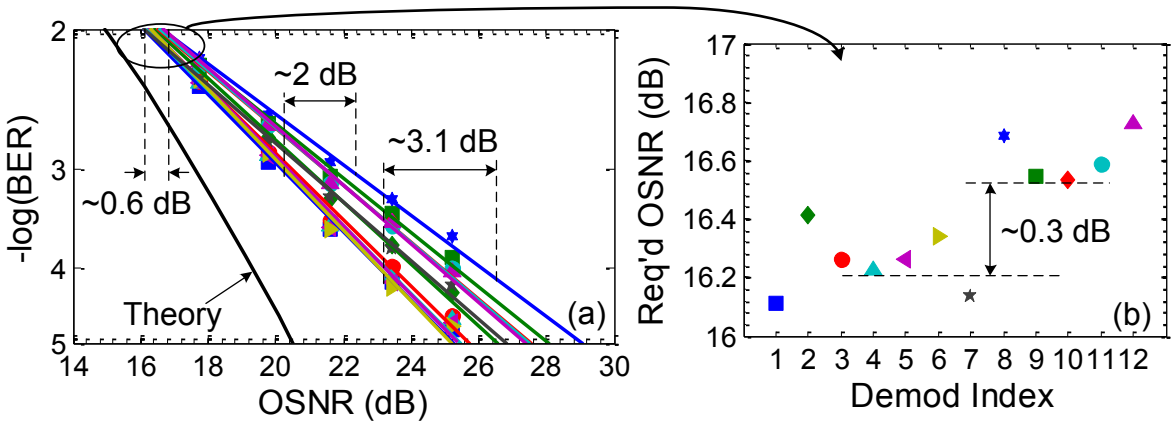


FIGURE 9.3 LEGEND

| DEMOD INDEX | SYM. | DEMOD NO. | NO. TAPS |
|---|---|---|---|
| 1 | ■ | 1 | 121 |
| 2 | ◆ | 2 | 31 |
| 3 | ● | 2 | 51 |
| 4 | ▲ | 2 | 61 |
| 5 | ◀ | 2 | 71 |
| 6 | ▶ | 2 | 91 |
| 7 | ★ | 3 | 121 |
| 8 | * | 4 | 31 |
| 9 | ■ | 4 | 51 |
| 10 | ◆ | 4 | 61 |
| 11 | ● | 4 | 71 |
| 12 | ▲ | 4 | 91 |

Figure 9.3. (a) Back-to-Back performance of the twelve different demodulation code configurations identified in the legend. The black line marks the theoretical performance of 16 GBaud PDM-16QAM in an AWGN channel is also shown. (b) The required OSNR for BER = $10^{-2}$ for each demodulation code configuration. The "Demod Index" of (b) corresponds to the assignment in legend.

demod code (Demod 1) demonstrates performance ~1 dB from the theoretical limit near $10^{-2}$ and ~2 dB from the theoretical limit near $10^{-3}$. For each code configuration we extracted the required OSNR for a BER of $10^{-2}$, Fig. 9.3(b). The required OSNR demonstrates that the optimum number of MIMO taps for Demod 2 & 4 is about 61; any further increase is detrimental to performance. However, Demod 1 & 3 which both employ per-polarization equalization outperform the MIMO equalizer. This behavior can be understood form the fact that back-to-back signals are only impaired by additive noise and thus do not require the $h_{xy}$ or $h_{yx}$ filters of the MIMO equalizer to average out the noise (assuming the previous polarization demultiplex converges properly).

We performed the same analysis on the center 16QAM signal after the transmission. We launched the WDM signal with per-channel powers ranging from -3 dBm to +4 dBm and performed an OSNR scan by adding noise at the receiver, after which we extracted the required OSNR for BER = $10^{-2}$ for each launch power case and for each demodulation case, Fig. 9.4. We observe two key characteristics of the transmission data. First, at low launch powers (-3 to +2 dBm) that correspond with the linear transmission regime, Demod 1 & 2 (#1-6 in Fig. 9.3) outperform Demod 3 & 4 (#7-12 in Fig. 9.3) in all corresponding cases. As the signal moves into the semi-nonlinear regime (+3 dBm, red squares), Demod 4 with the MIMO equalizer offers small but consistent performance advantages (~0.2 dB) compared to the ICA-based Demod 1 & 2. We attribute this behavior to the first asynchronous CMA polarization estimate which enables a better initial timing phase estimate before the final polarization demultiplex which therefore allows the final decision-directed LMS equalizer to perform better. Beyond +3 dBm launch power the nonlinear phenomena induce penalties that render the signal largely unrecoverable.

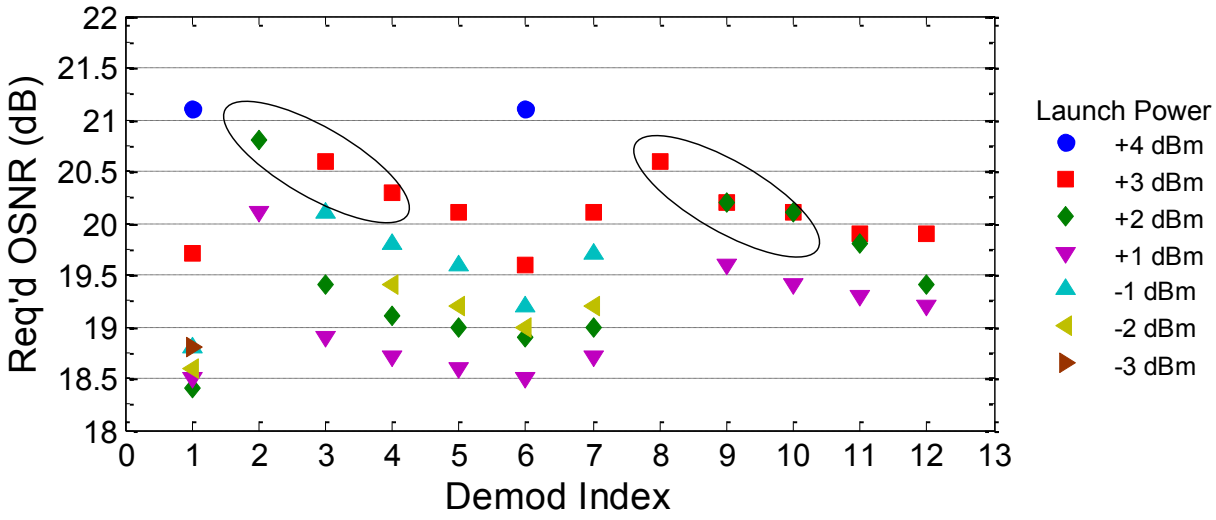


Figure 9.4. The req'd OSNR for BER = $10^{-2}$ of the center 16QAM channel for each demodulation code index after loop transmission. The colors correspond to the per-channel launch power shown in the legend. The demod index corresponds to the assignment given in the legend of Fig. 9.3.

## 9.2. Nonlinear Transmission Tolerances

The experimental network configuration for 16QAM transmission appears in Fig. 9.5. We utilize a recirculating frequency shifter to generate twenty-seven, 25 GHz-spaced tones, Fig. 9.5(a). A 25/50 GHz interleaver splits the 25 GHz tones into even and odd groups with 50 GHz spacing. The 14-carrier group of 50 GHz-spaced tones is then modulated for either OOK, BPSK, or QPSK at 32 GBaud. Next, the even and odd data channels are delayed with respect to each other using a commercial wavelength-selective switch (WSS) and then recombined. The WDM signal is combined in another WSS (which also performs channel power equalization) with a 32 GBaud RZ-PDM-16QAM which replaces the center ($7^{th}$) channel. The 16QAM signal is generated by driving an I/Q modulator with a 32 GBaud, 4-level electrical signal, Fig. 9.5(b). The subsequent RZ carver help clean up the time-domain pulse and is biased to yield a semi-flat spectrum to maximize the power contained in a single 50-GHz WDM channel, Fig. 9.5(c). Finally, all of the channels are polarization-multiplexed for transmission.

The recirculating loop consists of three spans of 88 km of large-area fiber (LAF), EDFA-only amplification, and no inline dispersion compensation. The data is circulated three times for a total transmission distance of ~792 km. After transmission, the data is unloaded and detected with a Picometrix coherent receiver and digitized at 80 GS/s with two Agilent real-time oscilloscopes. Offline processing is "Demod 1" described in §9.1. For each side channel modulation format we varied the per-channel launch power from -3 dBm to +1 to span a reasonable range of powers in commercial transmission. For each launch power point we measured the BER vs. OSNR performance of the center 16QAM channel by loading ASE noise at the receiver.

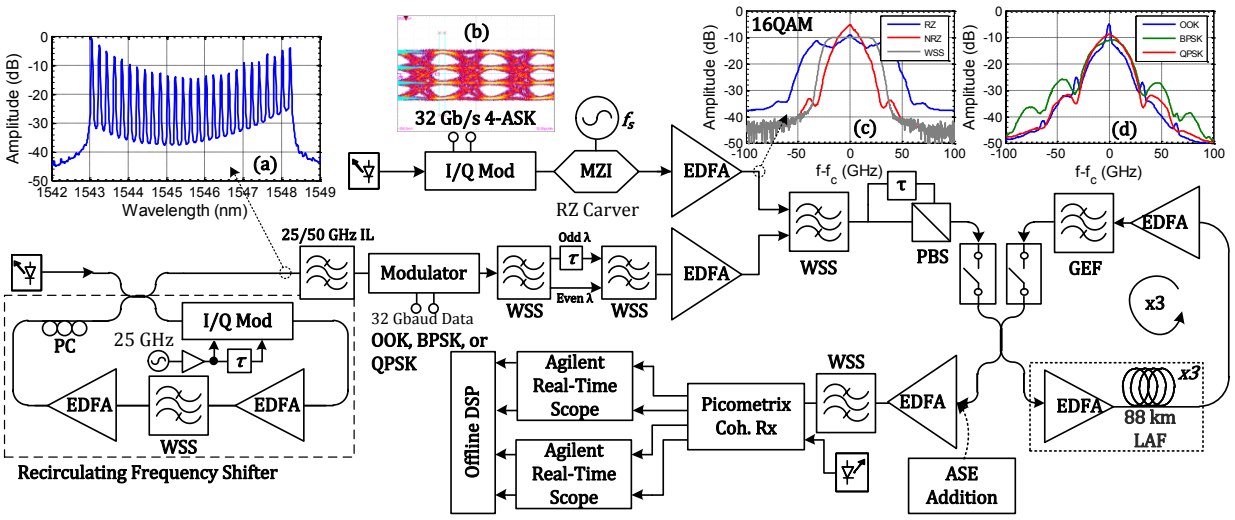


Figure 9.5. Experimental network configuration. A recirculating frequency shifter generates 27 tones spaced 25 GHz apart, inset (a). Every other tone (50 GHz) is modulated with either 32 GBaud OOK, BPSK, or QPSK, inset (d). These signals are configured to surround a 32 GBaud RZ-PDM-16QAM channel generated from a 4-level electrical signal driving an I/Q modulator, insets (b) and (c). A recirculating loop is employed for transmission over EDFA-amplified LAF spans.

The BER vs. launch power results of the center 16QAM signal for each side channel modulation format appear in Fig. 9.6. We observe in the baseline single-channel data (blue squares) that the RZ-PDM-16QAM signal achieves a minimum BER around +1 dBm launch power before transitioning into the nonlinear regime. With QPSK side channels, the 16QAM signal maintains linear transmission up to -1 dBm launch power. BPSK and OOK side channels (red triangles and green diamonds, respectively) drastically reduce the transmission capability of the center 16QAM signal, causing the minimum achievable BERs to skirt the $10^{-2}$ FEC limit for launch powers between -3 and +1 dBm. These results indicate that even at lower per-channel powers the nonlinear penalties induced by the BPSK and OOK channels are significantly worse than by QPSK channels. This can be understood from the symbol-o-symbol transitions – only 25% of all symbol transitions in a NRZ-QPSK signal traverse the zero point. Therefore the field intensity profile is much reduced compared to BPSK or OOK in which 50% of all transitions pass through zero amplitude.

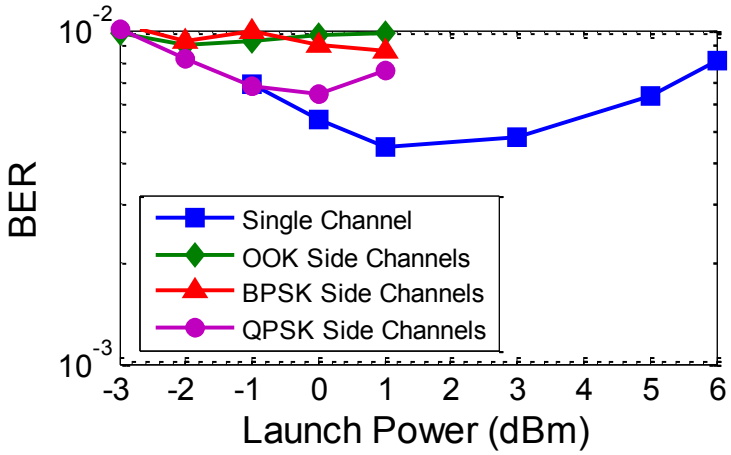


Figure 9.6. BER vs. launch power of the RZ-PDM-16QAM signal after 792 km LAF transmission with various types of side channels compared to the single-channel case.

At each launch power we measured the BER vs. OSNR performance by loading noise at the receiver. Using this data we extracted the required OSNR to achieve a BER of 10-2 for all combinations of launch power and side channel modulation type, Fig. 9.7. We observe from this data the expected increase in OSNR requirements as the per-channel launch power increases. Also, as demonstrated in the BER curves of Fig. 9.6, BPSK and OOK side channels induce larger transmission penalties on the 16QAM signal compared to QPSK side channels. The OSNR requirements of >20 dB shown in Fig. 9.7 indicate the much-limited allowable transmission distance of 16QAM signals compared to QPSK signals. The maximum achievable OSNR for these ~800 km transmission experiments is only about 23 dB at +1 dBm launch power; the system margin at +1 dBm launch power is ~1.25 dB.

The final experiment fixed the per-channel launch power to +1 dBm and the QPSK modulation format, but reduced the number of side channels in pairs, starting with the nearest neighbors, Fig. 9.8. We observe an immediate ~0.75 dB required OSNR benefit by removing the two nearest side channels. Because no further reduction in the number of side channels provides a reduction in required OSNR, we conclude that the nearest neighbor channels are the most significant in giving rise to nonlinear impairments. For high-density routes with low available

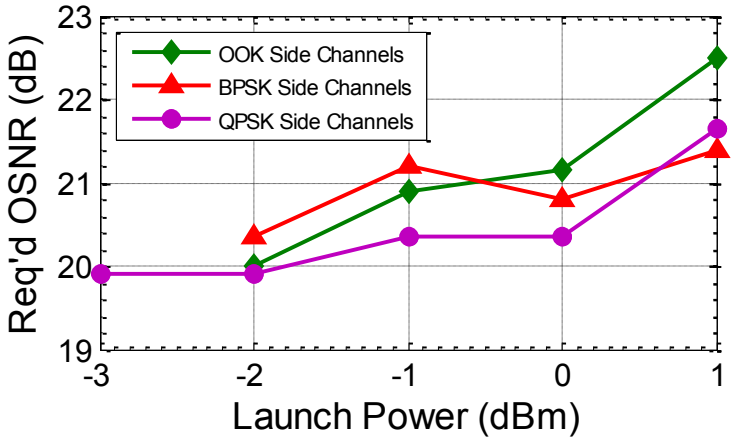


Figure 9.7. Required OSNR for BER = $10^{-2}$ of the 32 GBaud RZ-PDM-16QAM signal with various types of side channels after 792 km transmission.

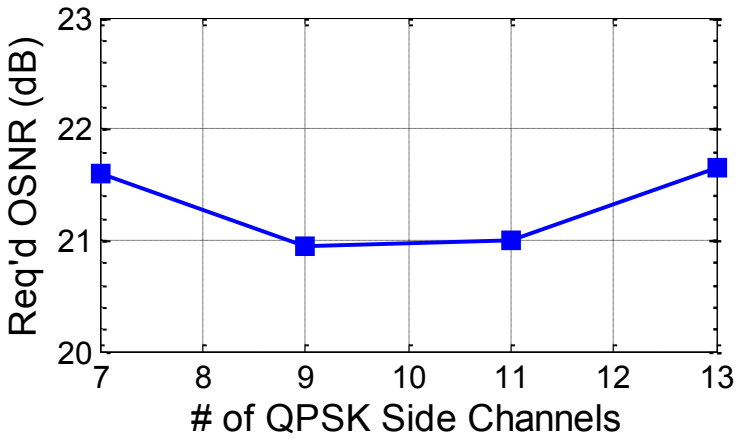


Figure 9.8. Required OSNR for BER = $10^{-2}$ of the 32 GBaud RZ-PDM-16QAM signal after 792 km transmission for a decreasing number of QPSK side channels (beginning from the inner-most).

OSNR margin, it might be necessary to remove one or both 50 GHz QPSK neighbors when upgrading to 16QAM signals.

### 9.3. Margin Prediction for 16QAM Transport

The experimental network for the PDM-16QAM transmission experiments appears in Fig. 9.9. We combine nine 50-GHz-spaced DFB and ECL lasers and modulate them via the same I/Q modulator driven by 32 GBaud 4-level electrical signals. The spectrum of a single 16QAM Fig. 9.10(a). A commercial WSS splits these 16QAM signals into two groups – one group of the

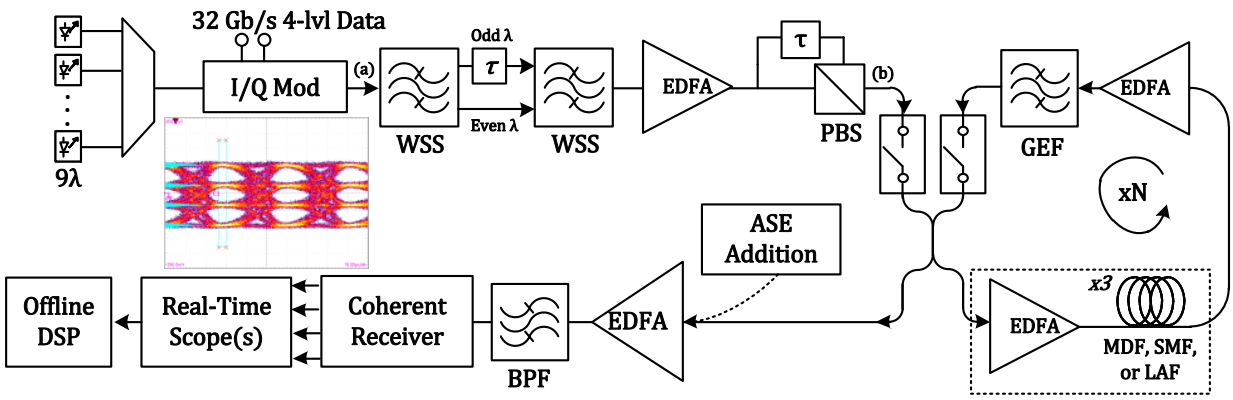


Figure 9.9. Experimental network configuration for the 16QAM WDM transmission experiments.

even channels and one group of the odd channels. These two channels groups are delayed relative to each other to decorrelate the data and then recombined in another WSS. Finally, we polarization-multiplex all of the channels to create nine, 256 Gb/s PDM-16QAM signals. The total WDM signal, Fig. 9.10(b), is then loaded into the recirculating loop for transmission. We note that channel 7 has a lower launch power than the other eight channels – this is because the carrier laser output power has degraded over time and no longer operates at maximum efficiency.

The recirculating loop consists of three spans of 90 km MDF, 90 km SMF, or 88 km of LAF, EDFA-only amplification, and no inline dispersion compensation. The data is circulated once for a total transmission distance of ~270 km. After transmission, the data is unloaded and detected with a Picometrix coherent receiver and digitized at 80 GS/s with two Agilent real-time oscilloscopes. Offline processing is "Demod 1" described in §9.1. For each fiber type we varied the per-channel launch power from -5 dBm to +6 to span a range of powers to thoroughly asses the fiber-limited transmission performance. For each launch power point we measured the BER vs. OSNR performance of the center 16QAM channel by loading ASE noise at the receiver.

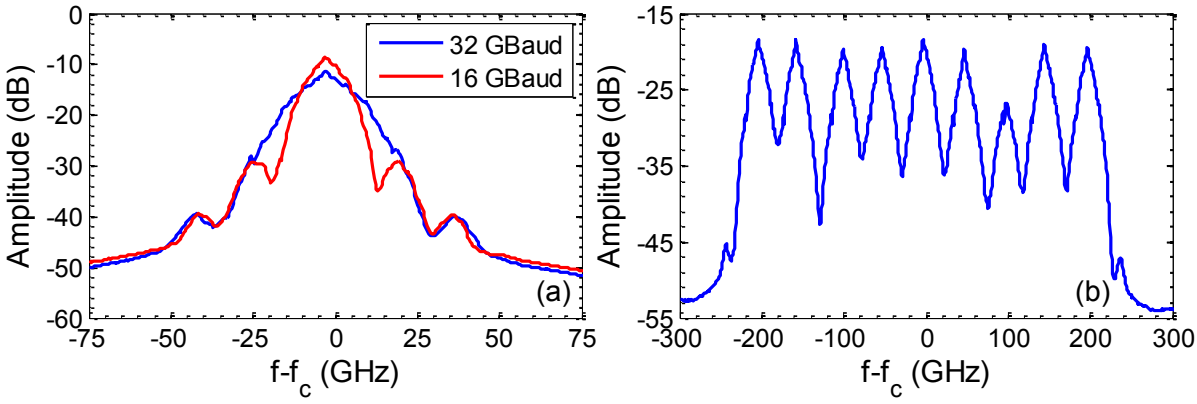


Figure 9.10. Back-to-back spectra of (a) the 32 Gbaud 16QAM signal at the output of the modulator compared to a 16 GBaud 16QAM signal and (b) the WDM spectrum just before transmission in the recirculating loop. These spectra (a) and (b) correspond to locations (a) and (b) marked in Fig. 9.9.

Prior to the loop transmission experiments we performed a single-channel analysis of the BER vs. OSNR performance of the 16QAM signal with both NRZ and RZ signaling formats, Fig. 9.11. The NRZ-PDM-16QAM baseline (blue squares) achieves a BER of $10^{-2}$ and a BER of $10^{-3}$ at ~19.5 and ~23.5 dB OSNR, respectively. This performance is 2 dB and 3.5 dB from the theoretical limit (black line). With RZ carving improves the receive sensitivity by ~0.8 dB across all BER values with up to 43.75 GHz filtering. When filtered at 37.5 GHz, the RZ-PDM-16QAM signal yields BER vs. OSNR performance identical to NRZ signaling, demonstrating the improved filtering tolerance that RZ signaling affords.

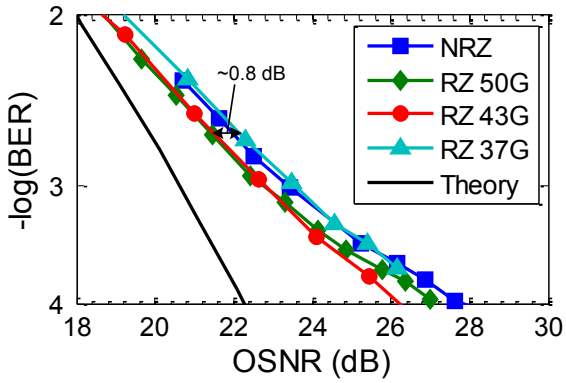


Figure 9.11. Back-to-back 32GBaud PDM-16QAM BER vs. OSNR performance comparison of NRZ and RZ signaling formats with three different WSS filter settings. Refer to Fig. 7.2 for the shapes of the WSS filters. RZ signaling tolerates up to a 37.5GHz filter with performance identical to NRZ signaling.

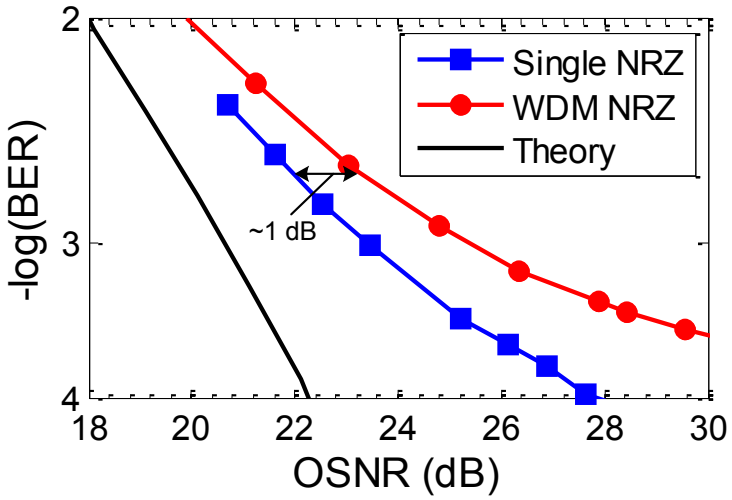


Figure 9.12. Back-to-back 32 GBaud PDM-16QAM BER vs. OSNR performance comparison of a single PDM-16QAM signal with the WDM setup in Fig. 9.9. We observe an ~1 dB implementation penalty.

After establishing the filtering tolerance of PDM-16QAM we characterized the implementation penalty of the experimental WDM network in Fig. 9.9 by measuring the BER vs. OSNR performance of the center 16QAM signal with the presence of the other WDM channel, Fig. 9.12. We observe an approximately 1 dB implementation penalty at BERs above $10^{-3}$ that decreases to about 0.5 dB near a BER of $10^{-2}$; the required OSNR for $10^{-2}$ is 20 dB. This penalty increases for larger OSNR values and lower BERs. Furthermore, the WDM network appears to induce a BER floor near $10^{-4}$. Per the methodology explained in §8.2, we fit the back-to-back 16QAM performance and extracted the fitting parameters to calibrate the nonlinear SNR computations.

At each launch power in the transmission experiments we computed the maximum achievable BER without adding ASE at the receiver, Fig. 9.13. MDF achieves BERs below $10^{-2}$ for launch powers between -4 and -2 dBm. When transmitted via SMF the PDM-16QAM channels demonstrate linear operation up to -2 dBm launch power after which the BERs begin to increase, crossing the $10^{-2}$ threshold around +3 dBm launch power. In LAF the PDM-16QAM channels operate linearly up to nearly +5 dBm launch power, achieving BER minimums of

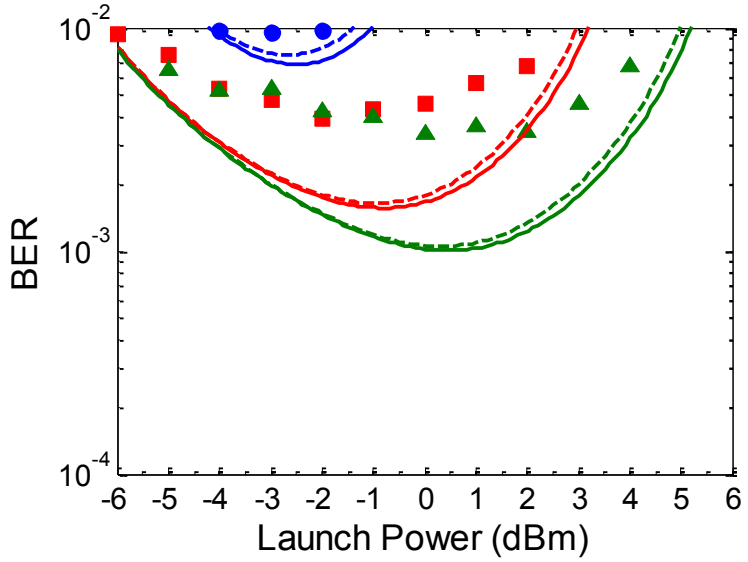


Figure 9.13. The BER of the center PDM-16QAM signal as a function of per-channel launch WDM launch power after one loop transmission (~270 km) in each of the three fiber types. The solid and dashed lines are theoretical margin calculations using the definition of nonlinear SNR in Eqns. (8.3-8.5) for incoherent and coherent noise accumulation, respectively.

~$3x10^{-3}$ between -1 and +1 dBm launch power. The calculated BER vs. launch power curves do not adhere as closely to experimental data as in the PDM-QPSK data (c.f. Fig. 8.3), despite the back-to-back calibration. The BER minimums, however, occur at the same launch powers as the experimental data.

When the 16QAM transmission results are recast in terms of OSNR penalty, Fig. 9.14, we observe similar exponential behavior to QPSK transmission penalties, Fig. 8.4. Furthermore, the actual amount of penalty (in dB) for 16QAM transmission is quite similar to penalties for QPSK transmission. Our calibrated results demonstrate the OSNR penalty converging to the expected 0 dB OSNR penalty that should occur for linear regime transmission. Because we compute the OSNR penalty with respect to the required OSNR for 10-2 from the back-to-back WDM case (Fig. 9.12, red circles) the penalty should not contain any implementation penalties due to crosstalk or filtering effects. However, and as discussed extensively in §6.2, any residual in-band crosstalk may give rise to enhanced transmission penalties not accounted for in back-to-

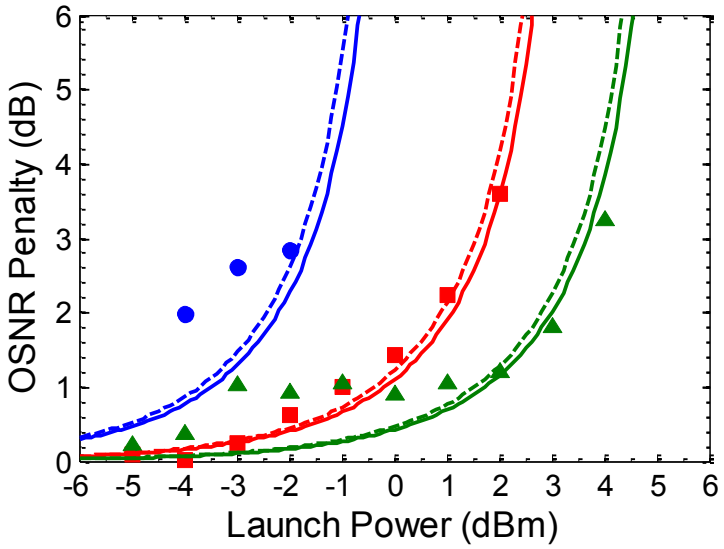


Figure 9.14. The OSNR penalty of the center PDM-16QAM signal as a function of per-channel launch WDM launch power after one loop transmission (~270 km) in each of the three fiber types. The solid and dashed lines are theoretical margin calculations using the definition of nonlinear SNR in Eqns. (8.3-8.5) for incoherent and coherent noise accumulation, respectively.

back measurements. We may also observe from Fig. 9.10 that an unfiltered 32GBaud 16QAM signal will induce linear crosstalk on neighboring channels if spaced at 50 GHz as they are in this experiment. Because of the laboratory setup limitations, this crosstalk is unavoidable. A commercial system with a separate transmitter for each 16QAM signal will necessarily have much better spectral control to avoid this penalty floor.

We also computed the link margin for the 16QAM transmission results per the definition described in §8.2, Fig. 9.15; *margin* is the difference between the maximum achievable OSNR and the OSNR which achieves a BER of $10^{-2}$. We observe a maximum margin of ~1 dB in MDF for -2 dBm launch power. Because our fiber spans for LAF and SMF have nearly identical loss we observe similar margins while in the linear transmission regime as marked by a 1 dB/dB margin slope. In SMF the margin slope decreases below 1 as the per-channel launch power increases above +0 dBm and the full transition into the nonlinear regime occurs after +1 dBm. In LAF this transition to the nonlinear regime occurs beyond +2 dBm launch power. As in the

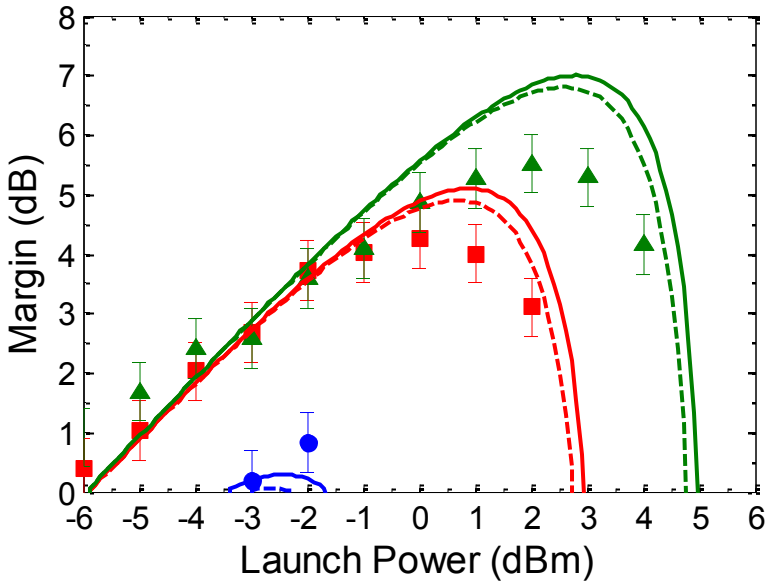


Figure 9.15. OSNR Margin at BER = $10^{-2}$ after ~270 km transmission for 32 GBaud PDM-16QAM as a function of per-channel launch power for MDF, SMF, and ULA fiber types. The solid and dashed lines are theoretical margin calculations using the definition of nonlinear SNR in Eqns. (8.3-8.5) for incoherent and coherent noise accumulation, respectively. Note that the maximum margin launch powers do not necessarily correspond to the launch powers that yield minimum BER from Fig. 9.13.

QPSK results the maximum margin does not occur at the minimum BER transmission launch power but at launch power where 1 dB of nonlinear interference penalty has accrued. That is, beyond the point where the linear increase in OSNR afforded by a higher launch power cannot overcome the nonlinear interference generated by the higher power.

LAF demonstrates a relative margin advantage of ~1.5 dB and ~4.5 dB over SMF and MDF, respectively. In our 32 Gbaud PDM-QPSK margin results, Fig. 8.6(b), we observe relative advantages for LAF of ~2 dB and 5 dB over SMF and MDF, respectively. These results compare favorably; the NLI computations of [36] indicate that the fiber-determined nonlinear transmission should retain the same relative difference despite changes in modulation format or baud rate.

Finally, we performed the same margin computations for 16QAM as described in Eqns. (8.4-8.7) for PDM-QPSK. These computations are the solid and dashed lines in Fig. 9.15. As in

the QPSK result, we observe that our data adheres closely to theoretical prediction. The data is within ±0.5 dB of the NLI calculations in the linear regime and within ~1 dB as the link transitioned into the nonlinear regime (near the margin peaks). Combined with the extensive QPSK experiments, this 16QAM lend credence to the GN model developed for approximating NLI accumulation for uncompensated transmission.

# CHAPTER 10

# CONCLUSION

State-of-the-art fiber-optic networks have begun the transition to coherent detection, PDM-QPSK, and 100 Gb/s transport. In conjunction with digital signal processing at the receiver, the paradigm of intensity modulation and direct detection has been broken. The combination of coherent detection and DSP is a revolutionary change for the network because it allows (1) phase-based modulation formats, (2) digital CD equalization, and (3) FEC.

Phase-based modulation formats enable the networks to achieve the spectral efficiency requirements demanded by current and next-generation computing devices. DSP has completely alleviated the need for dispersion management in the network; all CD compensation can be performed in silicon at the receiver, even without knowledge of the point of origin or distance traveled. CD and PMD management in IMDD networks placed hard limits on network flexibility and transport rates. But as has been shown throughout this dissertation, accrued dispersion plays an important role in *reducing* nonlinear transmission effects and *improving* transport margin (with the explicit understanding that compensation can be performed digitally). Finally, the introduction of FEC along with the digital receiver has also loosened constraints on the allowable raw BER detected by the receiver. BERs as high at $10^{-2}$ can be corrected to less than $10^{-12}$ with soft-FEC techniques. While first introduced into fiber-optic networks for IMDD networks, FEC is nevertheless a critical enabling technology for further advancements in modulation format from QPSK to 16QAM and beyond. Based on this methodology and set of assumptions the demodulation code developed for the Georgia Tech 100G Consortium was greatly improved and

expanded in capability. This work has added new algorithms for 16QAM carrier recovery, polarization demultiplexing, and carrier recovery (see §3 and §9) to the already-extensive GaTech algorithm suite for PDM-QPSK.

Understanding how nonlinear phenomena accrue to impair transmitted signals is an active and on-going current research topic in the community, especially in the highly-dispersive regime of networking with dispersion management. This dissertation work demonstrates experimentally for the first time that the "Gaussian Noise" model for highly dispersive transmission is applicable over a range of fiber types with PDM-QPSK channels (see §8). Heuristically, the GN model states that in the highly-dispersive regime the data signals appear noise-like and the nonlinear interactions that occur are statistically independent. And therefore by the Central Limit Theorem these nonlinear effects aggregate to a Gaussian distribution. That is, the nonlinear interference that accrues during transmission is not only statistically independent of other noise sources, but Gaussian-distributed. This remarkable result enables a computation of the total nonlinear noise which can then be added directly to the variance of the ASE noise due to inline amplifiers. And thus a theoretical "nonlinear SNR" can be computed for the maximum (total) link capacity at any given operating point.

There are several key understandings of the GN model. First, and as mentioned above, the statistical distribution of nonlinear interference is both statistically independent from other noise sources (ASE, specifically) and Gaussian-distributed. Second, (degenerate) FWM effects are the dominant nonlinear processes in the highly-dispersive regime; the variance of the nonlinear noise is proportional to the cube of the per-channel power and the square of the nonlinear coefficient. This result is likely inescapable because FWM effects are a third-order Kerr nonlinearity in silica fiber which generates a fourth frequency from the mixing products of

three beat terms, $f_g = f_i + f_j - f_k$. The magnitude of the generated signal is $\gamma^2 P_i P_j P_k$. Third, the total nonlinear interference accumulation of any single channel depends on the aggregate WDM signal and the total nonlinear interference increases monotonically with increasing WDM channel count. This result is a stark contrast to conventional wisdom that a test network with nine or eleven channels can adequately account for all nonlinear impairments of the full 80-channel C-band network.

Transmission with PDM-16QAM is the next logical step from PDM-QPSK for fiber-optic networks, offering twice the spectral efficiency and compatibility with existing 50-GHz ITU grid infrastructure. 16QAM can also be generated with the same I/Q modulator structures used for QPSK modulation and detected on the same coherent receivers with few bits of A/D resolution (~4). Additionally, DSP processing steps for CD equalization, timing recovery, equalization, and frequency offset estimation are identical to algorithms used for PDM-QPSK. Processing steps for polarization demultiplexing and carrier recovery require only minor changes with little, if any, increase in complexity. However, 16QAM SNR requirements are steep – experiments reported this dissertation reveal systems margins that allow ~1000 km transmission only for the most advanced, not-on-the-market fiber. Fiber plants based on SMF or MDF will require regeneration for any long-haul transmission with 16QAM. Because of the cost of regeneration compared to passive amplification it is likely that 16QAM will see deployment only on the highest-density routes with transmission limited to metro and regional distances.

### 10.1 Contributions of this Dissertation

Work in this dissertation has made the following contributions to the broader research community:

- Optimized regional and metro-distance dispersion maps for DQPSK and PDM-DQPSK [148, 149]
- Analysis of OQPSK for fiber-optic links [150, 151]
- Converged laboratory and numerical results to within 0.5 dB for better computational network simulations [137]
- Utilized the Nonlinear Threshold metric to craft engineering rules for both dispersion-managed and non-dispersion-managed hybrid optical links [90, 140, 152]
- Quantified crosstalk penalties in ROADM-enabled 100G networks [113, 153-155]
- Developed signal processing techniques for PDM-QPSK [60, 63]
- Demonstrated the network performance of 28 & 32 Gbaud PDM-QPSK [63, 90, 136, 140, 152, 156]
- Established the use of the "Gaussian Noise" model for nonlinear interference in the highly-dispersed transmission regime to predict PDM-QPSK and PDM-16QAM nonlinear performance [publications submitted]
- 16QAM processing algorithms in nonlinear transmission regimes [publications submitted]

The full list of publications resulting from all of the dissertation work currently comprises seven conference publications and one journal publications with secondary contributions to fourteen conference publications and six journal articles. Seven other conference contributions and three journal articles have also been submitted at the time of this writing and are awaiting decision.

### 10.2 Topics for Future Research

There remain numerous interesting studies available when moving forward from this effort. The addition of LAF to the GaTech Terabit Consortium testbed has expanded the impact

of the transmission link experiments reported in Chapters 8 and 9. In the last year, pure silica core fiber (PSCF) has been introduced that offer the next level of fiber channel performance. It is likely that PSCF will see near-future deployments and consequently the application of the margin prediction techniques developed herein to PSCF will be important. Beyond testing newer (and older) fiber there are several interesting research topics that stem directly from this work. These topics are margin prediction for heterogeneous networks, real-time electronics and transmit DSP, and "SuperReceivers."

### *10.2.1 Margin Prediction for Heterogeneous Networks*

The nonlinear interference analysis utilized for §8 and §9 provides a general set of equations for any network topology; the experiments tested homogeneous networks comprised of only one fiber type. However, most fiber-optic infrastructure in the ground of a mish-mash of old and new fibers, dispersion maps, span lengths, and amplifier types. An immediate extension of the experiments in this dissertation would be to determine the efficacy of the NLI equations for real-world heterogeneous networks. Both fortunately and unfortunately the test space is vast: almost any combination of fiber types represents a real-world network, but there are too many combinations to perform measurements on all of them. A critical part of this effort would be to determine what combination of dispersion maps, span lengths, and fiber types represents enough of the network "picture" to conclude that the theoretical analysis works and can thus be applied to the other network configurations not physically tested.

### *10.2.2 Real-Time Electronics and Transmit DSP*

Coherent receivers have enabled extensive DSP for digital demodulation and equalization in fiber-optic networks. Wireline and wireless network also employ extensive transmit DSP for pulse shaping and pre-equalization to continue optimizing channel capacity use. These techniques have not yet been introduced into fiber networks largely due to the lack of high-precision D/A converters that can operate at the >30 GS/s needed. Pre-distortion and signal shaping would allow fiber networks to overcome the limitations imposed by the nonlinear transfer function of the modulator, reduce filtering penalties that arise due to concatenated ROADMs, or avoid NLI accumulation. This is a topic of extremely active interest for extending network reach and reducing transport cost-per-bit by maximizing spectrum usage.

### *10.2.3 SuperReceivers*

The concept of the "SuperReceiver" is currently under active investigation at the Terabit consortium [135, 157-160]. In brief, SuperReceivers promise enable ultra-dense channel spacing by synchronously receiving groups of WDM signals. After synchronous detection, the SuperReceiver will utilize advanced DSP techniques to equalize the spectral overlap of neighboring channels utilizing data from knowledge of the adjacent channel. This concept may be an effective way to scale networks up to 400 Gb/s or 1 Tb/s without extremely complicated transmit or receive structures. However, these studies remain to be done experimentally.

# REFERENCES


[1] K. Roberts, "Key Technology Enablers of 100 Gbit/s in Carrier Networks," *Proc. of OFC*, NWA1, Mar 2011.

[2] T. J. Xia, et al., "Transmission of 107-Gb/s DQPSK over Verizon 504-km Commercial LambdaXtreme Transport System," *Proc. of OFC*, NMC2, Mar 2008.

[3] B. Zhang and S. Khatana, "From lab demo to field trial: Real-time coherent 127 Gb/s PM-QPSK transmission," *Phot. Global Conf.*, Dec 2010.

[4] H. Griesser, et al., "Nonlinear Tolerance of 112 Gb/s DP-QPSK in a Live Field Upgrade Trial over 848 km 10G DWDM Link," *Proc. of OFC*, NWA3, Mar 2011.

[5] J. Sakaguchi, et al., "19-core fiber transmission of 19x100x172-Gb/s SDM-WDM-PDM-QPSK signals at 305 Tb/s," *Proc. of OFC*, PDP5C.1, Mar 2012.

[6] A. Sano, et al., "102.3-Tb/s (224x548-Gb/s) C- and Extended L-band All-Raman Transmission over 240 km Using PDM-64QAM Single Carrier FDM with Digital Pilot Tone," *Proc. of OFC*, PDP5C.3, Mar 2012.

[7] J. Buck, *Fundamentals of Fiber Optics*, John Wiley & Sons, Inc, New Jersey, 2004.

[8] R.-J. Essiambre, et al., "Capacity Limits of Optical Fiber Networks," *Journ. Of Lightwave Technol.*, Vol. 28, No. 4, Feb 2010.

[9] R. Ramaswami and K. Sivarajan, *Optical Networks*, Academic Press, San Diego, 2002.

[10] L. G. Kazovsky, "Multichannel Coherent Optical Communications Systems," *Journ. Of Lightwave Technol.*, Vol. LT-5, No. 8, Aug 1987.

[11] G. P. Agrawl, *Fiber Optic Communication Systems*, Wiley-Interscience, 2002.

[12] G. P. Agrawl, *Nonlinear Fiber Optics*, Academic Press, Inc., San Diego, 1989.

[13] C.R.S. Fludger, et al., "Characterisation of an RZ-DQPSK transmitter using coherent detection," *Proc. Of ECOC*, pp.1-2, 16-20 Sept. 2007.

[14] T. Duthel, et al, "Impairment tolerance of 111Gbit/s POLMUX-RZ-DQPSK using a reduced complexity coherent receiver with a T-spaced equaliser," *Proc. Of ECOC*, pp.1-2, 16-20 Sept. 2007.

[15] D. van den Borne, at al., "Coherent Equalization versus Direct Detection for 111-Gb/s Ethernet Transport," *IEEE/LEOS Summer Topical Meetings*, pp.11-12, 23-25 July 2007.

[16] C. R. S. Fludger, et al., "Coherent Equalization and POLMUX-RZ-DQPSK for Robust 100-GE Transmission," *Journ. Of Lightwave Technol.*, Vol. 26, No. 1, Jan 2008.

[17] X. Liu, et al., "Efficient digital coherent detection of a 1.2 Tb/s 24-carrier no-guard-interval CO-OFDM signal by simultaneously detection multiple carriers per sampling," *Proc. of OFC*, 2010.

[18] S. Chandrasekhar, et al., "Transmission of 1.2 Tb/s 24-carrier no-guard-interval coherent OFDM super-channel over 7200 km of ultra-large-area fiber," *Proc. of ECOC*, 2009.

[19] Y. Ma, et al., "1-Tb/s single-channel coherent optical OFDM transmission with orthogonal-band multiplexing and subwavelength bandwidth access," *Journ. Of Lightwave Technol.*, Vol. 28, No. 4, Feb 2010.

[20] S. K. Ibrahim, et al., "Toward a Practical Implementation of Coherent WDM: Analytical, Numerical, and Experimental Studies," *IEEE Photonics Journal*, Vol. 2, No. 5, Oct. 2010.

[21] F. Tian, et al., "Generation of 50 Stable Frequency-Locked Optical Carriers for Tb/s Multicarrier Optical Transmission Using a Recirculating Frequency Shifter," *Journ. Of Lightwave Technol.*, Vol. 29, No. 8, Apr 2011.

[22] D. Peckham and R. Lingle Jr., "New Fibers for Terabit Transmission Systems," IEEE *Phot. Soc. Summer Topicals*, TuC2.4, July 2011.

[23] ITU-T, "Series G: Transmission Systems and Media, Digital Systems and Network," http://www.iet.unipi.it/m.luise/HTML/AdT/ITU_G652.pdf , accessed 19 Aug 2012.

[24] X. Chen, et al., "Reception of Dual-LP11-Mode CO-OFDM Signals through Few-mode Compatible Optical Add/Drop Multiplexer," *Proc. of OFC*, PDP4B.4, March 2012.

[25] R. Ryf, et al., "Low-Loss Mode Coupler for Mode-Multiplexed transmission in Few-Mode Fiber," *Proc. of OFC*, PDP5B.5, March 2012.

[26] L. Gruner-Nielsen, et al., "Few Mode Transmission Fiber with low DGD, low Mode Coupling and low Loss," *Proc. of OFC*, PDP5A.1, March 2012.

[27] R. Ryf, et al., "Space-Division Multiplexed Transmission over 4200 km 3-Core Microstructured Fiber," *Proc. of OFC*, PDP5C.2, March 2012.

[28] N. K. Fontaine, "Space-division multiplexing and all-optical MIMO demultiplexing using a photonic integrated circuit," *Proc. of OFC*, PDPB.1, March 2012.

[29] Lightwave Online, "Huawei unveils programmable 2-Tbps WDM Prototype," 19 July 2012, http://www.lightwaveonline.com/articles/2012/07/huawei-unveils-programmable-2-tbps-wdm-prototype.html.

[30] Lightwave Online, "ZTE displays 400-GBps and 1-Tbps DWDM prototype," 18 June 2012, http://www.lightwaveonline.com/articles/2012/06/zte-displays-400-gbps-and-1-tbps-dwdm-prototype.html.

[31] Lightwave Online, "Sprint upgrades network, sets 400G trial with Ciena," 14 June 2012, http://www.lightwaveonline.com/articles/2012/06/sprint-upgrades-network-sets-400g-trial-with-ciena.html.

[32] K. J. Blow and N. J. Doran, "Nonlinear effects in optical fibres and fibre devices," *IEE Proceedings*, Vol. 134, Pt. J, No. 3, June 1987.

[33] R. W. Tkach, et al., "Four-Photon Mixing and High-Speed WDM Systems," *Journ. Of Lightwave Technol.*, Vol. 13, No. 5, May 1995.

[34] X. Chen and W. Shieh, "Closed-form expression for nonlinear transmission performance of densely spaced coherent optical OFDM," *Optics Express*, Vol. 18, No. 18, 2010.

[35] C. R. Menyuk and B. S. Marks, "Interaction of Polarization Mode Dispersion and Nonlinearity in Optical Fiber Transmission Systems," *Journ. Of Lightwave Technol*., Vol. 24, No. 7, July 2006.

[36] A. Carena, et al., "Modeling the Impact of Nonlinear Propagation Effects in Uncompensated Optical Coherent Transmission Links," *Journ. Of Lightwave Technol.*, Vol.30. No.10, 2012.

[37] RSoft Design Group, OptSim™ Product Overview, http://www.rsoftdesign.com/products.php?sub=System+and+Network&itm=OptSim , accessed 23 August 2012.

[38] VPI Photonics Design Automation, VPItransmissionMaker Optical Systems, http://www.vpiphotonics.com/TMOpticalSystems.php , accessed 23 August 2012.

[39] ITU-T, "Series G: Transmission Systems and Media, Digital Systems and Network," http://www.itu.int/rec/T-REC-G.694.1-201202-I/en , accessed 19 Aug 2012.

[40] Finisar, "WSS ROADMs," http://www.finisar.com/products/wss-roadms , accessed 19 August 2012.

[41] Nistica, "Full Fledge 25", http://www.nistica.com/fledge25.html , accessed 19 August 2012.

[42] M. Amersfoort, "Arrayed Waveguide Grating," Application Note A1998003, http://web.archive.org/web/20070927081252/http://www.c2v.nl/products/software/support/files/A1998003B.pdf , accessed 19 August 2012.

[43] M. Shibutani, et al., "Polarization Diversity Coherent Optical Receiver with a Balanced Receiver Configuration," *Proc. Of ECOC* 1988, pp. 151-154.

[44] M. Shibutani and S. Yamazaki, "A study on an active square-law combining method for a polarization-diversity coherent optical receiver," *IEEE Phot. Technol. Letters*, vol. 1, no. 7, 1989.

[45] Y. Mori, et al., "Unrepeated 200-km transmission of 40-Gbit/s 16-QAM signals using digital coherent optical receiver," *Proc. Of OECC/ACOFT* 2008.

[46] M. Yoshida, et al., "Real-time FPGA-based coherent optical receiver for 1 Gsymbol/s, 64 QAM transmission," *Proc. Of OFC* 2011, OTuN3.

[47] M. Liu, et al., "A Widely-tunable Integrated Coherent Optical Receiver Using a Phase-Locked Loop," *Proc. Of PHO* 2011, ThL4.

[48] E. Ip and J. M. Kahn, "Compensation of Dispersion and Nonlinear Impairments Using Digital Backpropagation," *Journ. Of Lightwave Technol*., Vol. 26, No. 20, Oct 2008

[49] www.appliedmicro.com/MyAMCC/retrieveDocument/FPD/white_papers/Pemaquid_White_Paper_2008_011408.pdf

[50] T. Mizuochi, "Recent Progress in Forward Error Correction and Its Interplay with Transmission Impairments," *IEEE Journ. of Sel. Top. In Quantum Elec*., Vol. 12, No. 4, 2006

[51] K. Onohara, et al., "Soft-Decision-Based Forward Error Correction for 100 Gb/s Transport Systems," *IEEE Journ. of Sel. Top. In Quantum Elec*., Vol. 16, No. 5, 2010.

[52] G. Bosco, et al., "On the Performance of Nyquist-WDM Terabit Superchanels Based on PM-BPSK, PM-QPSK, PM-8QAM, or PM-16QAM Subcarriers," *Journ. Of Lightwave Technol.*, Vol. 29, No. 1, Jan 2011.

[53] J. G. Proakis, *Digital Communications,* McGraw-Hill, 4th Ed., 2000.

[54] www.oiforum.com/public/documents/OIF-FD-100G-DWDM-01.0.pdf

[55] www.ciena.com/news/news_nyse.htm

[56] M. Kuschnerov, et al., "Adaptive Chromatic Dispersion Equalization for Non-Dispersion Managed Coherent Systems," *Proc. Of OFC*, OMT1, 2009.

[57] Godard, D. N., "Self-recovering equalization and carrier tracking in two-dimensional data communication systems," *IEEE. Trans. Commun*. COM-28(11), 1867-1875 (1980).

[58] Tugnait, J. K., "Blind equalization and channel estimation for multiple-input multiple-output communication systems," *IEEE Conf. on Acoustics, Speech, and Signal Processing*, Vol. 5, pp. 2443-2446, 1996.

[59] R. Johnson, et al., "Blind Equalization Using the Constant Modulus Criterion: A Review," *Proceedings of the IEEE*, Vol. 86, October 1998, pp. 1927–1950.

[60] T. F. Detwiler, et al., "Asynchronously sampled blind source separation for coherent optical links," *Proc. Of SPIE*, v. 7960, p. 79600D, 2011.

[61] M. Oerder and H. Myer, "Digital filter and square timing recovery", *IEEE Trans. Commun*., vol. COM-36, no. 5, pp. 605-612, May 1988.

[62] A. J. Viterbi and A. M. Viterbi, "Nonlinear estimation of PSK-Modulated carrier phase with application to burst digital transmission," *IEEE Trans. Inf. Theory*, vol. IT-29, no. 4, Jul. 1983.

[63] A. Stark, et al., "Performance of 32-Gbaud PDM-QPSK in nonlinear transport regimes with different phase recovery methods," *Proc. Of SPIE*, v. 8284, p. 82840B, 2012.

[64] M. Taylor, "Phase Estimation Methods for Optical Coherent Detection Using Digital Signal Processing," *Journ. Of Lightwave Technol*., Vol. 27, No. 7, April 2009.

[65] J. G. Proakis and D. G. Manolakis, *Digital Signal Processing: Principles, Algorithms, and Applications*, Pearson/Prentice Hall, 4th Ed., 2007.

[66] S. Amari et.al., "Multichannel Blind Deconvolution and Equalization using Natural Gradient", *Signal Processing Advances in Wireless Communications*, 1997 First IEEE Signal Processing Workshop on , vol., no., pp.101-104, 16-18 Apr 1997.

[67] G. Picchi and G. Prati, "Blind Equalization and Carrier Recovery Using a "Stop-and-Go" Decision-Directed Algorithm," *IEEE Trans. On Comm*., Col. COM-35, No. 9, Sept. 1987.

[68] I. Fatadin, et al., "Blind Equalization and Carrier Phase Recovery in a 16-QAM Optical Coherent System," *Journ. Of Lightwave Technol*., Vol. 27, No. 15, August 2009.

[69] M. Mishali and Y. Eldar, "Sub-Nyquist Sampling," *IEEE Signal Processing Magazine*, pp. 98-123, November 2011.

[70] S. Savory, "Digital Coherent Optical Receivers: Algorithms and Subsystems," *IEEE J. Sel. Top. Quant. Electron*., Vol. 16, No. 5, 2010.

[71] Z. Tao, et al., "Improvements to Digital Carrier Phase Recovery Algorithm for High-Performance Optical Coherent Receivers," *IEEE J. Sel. Top. Quant. Electron*., Vol. 16, No. 5, 2010.

[72] P. J. Winzer and R. Essiambre, "Advanced Optical Modulation Formats," *Proc. IEEE*, Vol. 94, No. 5, 2006.

[73] D. Ly-Gagnon, et al., “Coherent detection of optical quadrature phase-shift keying signals with carrier phase estimation,” *Journ. Of Lightwave Technol*., Vol. 24, No. 1, Jan. 2006.

[74] C. Furst et. al., “Analysis of Crosstalk in Mixed 43 Gb/s RZ-DQPSK and 10.7 Gb/s DWDM Systems at 50 GHz Channel Spacing,” *Proc. Of OFC*, OThS2, 2007.

[75] S. Chandrasekhar et al., "Impact of Channel Plan and Dispersion Map on Hybrid DWDM Transmission of 42.7-Gb/s DQPSK and 10.7-Gb/s OOK on 50-GHz Grid*," IEEE Phot. Technol. Letters*, vol. 19, pp. 1801-1803, 2007.

[76] X. Xian et al., "XPM penalty mitigation for a 42.7-Gb/s DQPSK channel co-propagating with 10.7-Gb/s OOK channels using SSMF and dispersion map," *LEOS*, WH4, 2008.

[77] L. D. Coelho et al., "Global optimization of RZ-DPSK and RZ-DQPSK systems at various data rates," *Proc. Of OFC*, JThA39, 2009.

[78] K. Nakamura et al., “Dispersion map suitable for hybrid 10 Gb/s NRZ and 40 Gb/s RZ-DQPSK transmission over 50 GHz-spaced network with low dispersion fibre,” *Proc. Of ECOC*, pp. 2 , 2007.

[79] T. Jesupret, et al., “Digital Demodulator Synchronization Performance Analysis,” *ESA Final Report*, June 1991.

[80] M. Moeneclaey and G. Ascheid, *Proc. 2nd Int. Wkshp DSP/Space Comm*. 1990.

[81] C. M. DeCusatis, “Fiber optic infrastructure and dispersion compensation for storage area networks,” *IEEE Comm. Mag*., Vol. 43, no. 3, 2005.

[82] A. Blum, “Mapping the Internet: Undersea Cables,” *Forbes*, http://tech.fortune.cnn.com/2012/07/16/chartist-undersea-internet-cables/, accessed 12 Nov 2012.

[83] S. Akhtar, “Comcast Optical Network: A Truly Converged Infrastructure,” *Proc. Of OFC*, NThC1, 2011.

[84] G. Gavioli, et al., “NRZ-PM-QPSK 16 x 100 Gb/s Transmission Over Installed Fiber With Different Dispersion Maps,” *IEEE Phot. Technol. Letters*, Vol. 22, No. 6, 2010

[85] A. Farbert, et al., “Optimized dispersion management scheme for long-haul optical communication systems,” *Electronics Letters*, Vol. 35, No. 21, 1999.

[86] J.-P. Elbers, et al., “Reduced model to describe SPM-limited Fiber Transmission in dispersion-managed lightwave systems,” *IEEE J. Sel. Top. Quant. Electron*., vol. 6, no. 2, pp. 276-281, Mar./Apr. 2000.

[87] C. Furst, et al., “Limitations of dispersion-managed DWDM systems due to cross-phase modulation,” *LEOS* 2000. MB3.

[88] J. C. Antona, et al., “Nonlinear cumulated phase as a criterion to assess performance of terrestrial WDM systems,” *Proc. Of OFC*, WX5, 2002.

[89] A. Carena, et al., "A time-domain optical transmission system simulation package accounting for nonlinear and polarization-related effects in fiber," *IEEE Journal on Selected Areas in Communications*, vol. 15, no. 4, pp. 751-765, May 1997.

[90] Andrew Stark, et al., “Scaling 100G QPSK links for reliable network development,” *Proc. Of SPIE* 2011, 7959-11.

[91] D. Grosz, et al., “All-Raman Ultralong-Haul Single-Wideband DWDM Transmission Systems With OADM Capability,” *Journ. Of Lightwave Technol*., Vol. 22, No. 2, Feb. 2004.

[92] S. Tibuleac and M. Filer, “Trends in next-generation ROADM network,” Proc. Of ECOC 2011, Th.12.A.1.

[93] K. Grobe, "Applications of ROADMs and Control Planes in Metro and Regional Networks," *Proc. Of OFC* 2007, NTuC1.

[94] M. Filer and S. Tibuleac, "Generalized weighted crosstalk for DWDM systems with cascaded wavelength-selective switches," *Optics Express*, vol. 20, no. 16, July 2012.

[95] S. Tibuleac and M. Filer, "Transmission impairments in DWDM Networks with reconfigurable optical add-drop multiplexers," *Journ. Of Lightwave Technol.*, vol. 28, no. 4, pp. 557-568, 2010.

[96] N. Kataoka et al., "Field trial of 640-Gbit/s-throughput, granularity-flexible optical network using packet-selective ROADM prototype," *Journ. Of Lightwave Technol.*, vol. 27, no. 7, pp. 825-831, Apr., 2009.

[97] H. Zhu and B. Mukherjee, "Online connection provisioning in metro optical WDM networks using reconfigurable OADMs," *Journ. Of Lightwave Technol.*, vol. 23, no. 10, pp. 2893-2901, Oct., 2005.

[98] T. A. Strasser and J. L. Wagener, "Wavelength-selective switches for ROADM applications*," IEEE J. Selec. Topics in Quant. Elec.*, vol. 16, no. 5, pp. 1150-1157, Sept.-Oct. 2010.

[99] B. Collings et al, "Dependence of the transmission impairment on the WSS port isolation spectral profile in 50GHz ROADM networks with 43Gb/s NRZ-ADPSK signals," *Proc. Of OFC/NFOEC*, 2009, paper OThJ3.

[100] T. Zami et al., "Crosstalk analysis applied to wavelength selective switches," *Proc. OFC/NFOEC*, 2006, paper OFP4.

[101] S. Yamamoto et al., “Influence of intrachannel crosstalk with frequency dependence on signal degradation in optical switch network,” *Journ. Of Lightwave Technol*., vol. 27, no. 24, pp. 5716-5722, Dec., 2009.

[102] H. Bissessur and C. Bastide, “Experimental assessment of frequency-dependent crosstalk penalty with different 43 Gb/s modulation formats,” *Proc. Of ECOC*, 2007, paper P083

[103] A. Bononi, N. Rossi, and P. Serena, "Transmission limitations due to fiber nonlinearity," *Proc. Of OFC/NFOEC*, 2011, paper OWO7.

[104] B. Xu and M. Brandt-Pearce, “Analysis of noise amplification by a CW pump signal due to fiber nonlinearity,” *IEEE Photon. Technol. Lett*., vol. 16, no. 4, pp. 1062–1064, Apr. 2004.

[105] A. Carena, at al., “New analytical results on fiber parametric gain and its effects on ASE noise,” *IEEE Photon. Technol. Lett*., vol. 9, pp. 535–537, Apr. 1997.

[106] G. Gavioli, et al., “Ultra-Narrow-Spacing 10-Channel 1.12 Tb/s D-QDM Long-Haul Transmission Over Uncompensated SMF and NZDSF,” *IEEE Photon. Technol. Lett*., vol. 22, no. 19, Oct. 2010.

[107] S. Chandrasekhar and X. Liu, “Experimental investigation on the performance of closely spaced multi-carrier PDM-QPSK with digital coherent detection,” *Optics Express*, Vol. 17, no. 24, Aug 2009.

[108] Q. Yang, et al., “1-Tb/s Large Girth LDPC-Coded Coherent Optical OFDM Transmission over 1040-km Standard Single-Mode Fiber,” *Proc. of OFC/NFOEC* 2011, JThA35.

[109] Z. Wang, et al., “Performance Investigation of Polarization-Multiplexed 16-QAM using All-Optical OFDM Transmission and Digital Coherent Detection,” *Proc. Of OFC/NFOEC* 2011, OMS5.

[110] J. Renaudier, et al., "Nonlinear tolerance of ultra-densely spaced 100Gb/s coherent PDM-QPSK channels," *Proc. Of ECOC* 2010, Mo.2.C.3.

[111] L. E Nelson, et al., "100Gb/s dual-carrier DP-QPSK performance after WDM transmission including 50GHz Wavelength Selective Switches," *Proc. Of OFC/NFOEC* 2011, NWA2.

[112] K. Roberts, et al., "Performance of Dual-Polarization QPSK for Optical Transport Systems," *Journ. Of Lightwave Technol.*, Vol. 27, No. 16, pp. 3546-3559, 2009.

[113] Y.-T. Hsueh et al, "In-band Crosstalk Transmission Penalties on 112-Gb/s PDM-QPSK Optical Links," *IEEE Photon. Technol. Lett.*, Vol. 23, no. 11, pp. 745-747 (2011).

[114] L. E. Nelson, et al., "Detection of a Single 40 Gb/s Polarization-Multiplexed QPSk Channel With a Real-Time Intradyne Receiver in the Presence of Multiple Coincident WDm Channels," *Journ. Of Lightwave Technol.*, Vol. 28, No. 20, (2010).

[115] C. Xie, et al., "Colorless coherent receiver using 3x3 coupler hybrids and single-ended detection," *Proc. Of ECOC*, Th.13.B.2 (2011).

[116] Inphi Press Release, http://www.inphi.com/news-events/press-releases-and-media-alerts/inphi-delivers-industryrsquos-first-tia-that-enables-100g-reconfigurable-colorless-networks.php.

[117] A. Carena, et al, "Coherent polarization-multiplexed formats: receiver requirements and mitigations of fiber non-linear effects," Proc. Of ECOC, 2010.

[118] S. K. Korotky, "Traffic trends: Drivers and measures of cost-effective and energy-efficient technologies and architectures for backbone optical networks," *Proc. Of OFC* 2012, OM2G.1.

[119] R. W. Tkach, "Scaling optical communications for the next decade and beyond," *Bell Labs Tech. Journ.,* vol. 14, no. 4, 2010.

[120] P. Winzer, "High-Spectral-Efficiency Optical Modulation Formats," *Journ. Of Lightwave Technol.*, Vol., No. , (2012)

[121] D. van den Borne, et al., "POLMUX-QPSK modulation and coherent detection: The challenge for long-haul 100G transmission," *Proc. Of ECOC* 2009, Vienna, Austria, Sep. 2009, paper 3.4.1.

[122] V. Curri, et al., "Dispersion compensation and mitigation of non-linear effects in 111 Gb/s WDM coherent PM-QPSK systems," *IEEE Photon. Technol. Lett*., Vol. 20, No. 7, pp1473-1475, 2008.

[123] A. Carena, et al., "Statistical Characterization of PM-QPSK Signals after Propagation in Uncompensated Fiber Links," in *Proc. Of ECOC* 2010, Torino, Italy, Sep. 2010, paper 4.07.

[124] P. Poggiolini, et al., "Analytical Modeling of Nonlinear Propagation in Uncompensated Optical Transmission Links," *Photon. Technol. Letters*, Vol. 23, No. 11, 2011.

[125] G. Bosco, et al., "Experimental Investigation of Nonlinear Interference Accumulation in Uncompensated Links," *Photon. Technol. Letters*, Vol. 24, No. 14, 2012.

[126] A. Mecozzi, et al., "Nonlinear Shannon Limit in Pseudolinear Coherent Systems," *Journ. Of Lightwave Technol*., Vol.30. No.12, 2012.

[127] P. Mitra and J. Stark, "Nonlinear limits to the information capacity of optical fibre communications," *Nature*, Vol. 411, pp.1027- 1030, 2001.

[128] A. Ellis, et al., "Approaching the Non-Linear Shannon Limit," *Journ. Of Lightwave Technol*., Vol. 28. No. 4, 2010.

[129] X. Chen and W. Shieh, "Closed-form expression for nonlinear transmission performance of densely spaced coherent optical OFDM," *Optics Express*, Vol. 18, No. 18, 2010.

[130] J. Tang, "A Comparison Study of the Nonlinear Shannon Channel Capacity of Various Nonlinear Optical Fibers," *Journ. Of Lightwave Technol*., Vol. 24. No. 5, 2006.

[131] F. Vacondio, et al., "Experimental characterization of Gaussian-distributed nonlinear distortions," *Proc. Of ECOC* 2011, We.7.8.1.

[132] P. Poggiolini, et al., "Analytical Modeling of Nonlinear Propagation in Uncompensated Optical Transmission Links," *Photon. Technol. Letters*, Vol. 23, No. 11, 2011.

[133] G. Bosco, et al., "Performance prediction for WDM PM-QPSK transmission over uncompensated links," *Proc. Of OFC* 2011, OThO7.

[134] R. Tkach, et al., "Four-Photon Mixing and High-Speed WDM Systems," *Journ. Of Lightwave Technol*., Vol.13. No. 5, 1995.

[135] J. Pan, et al., "Inter-Channel Crosstalk Cancellation for Nyquist-WDM Superchannel Applications," *Journ. Of Lightwave Technol*., Vol.. No., 2012.

[136] Andrew Stark, et al., "Filter Bandwidth and Subcarrier Spacing Tolerance of Single-carrier 32 Gbaud PDM-QPSK," *IEEE Photonics Society Summer Topicals*, vol., no., pp., 18-20 July 2011, Montreal, Canada.

[137] S. Searcy, et al., "Developing accurate simulations for high-speed fiber links," *Proc. Of SPIE*, v. 7960, p. 79600A, 2011.

[138] M. S. Alfiad, et al, "On the Tolerance of 111-Gb/s POLMUX-RZ-DQPSK to Nonlinear Transmission Effects", *Journ. Of Lightwave Technol*., Vol.29. No. 2, 2011.

[139] M. S. Alfiaad, et al., "A Comparison of Electrical and optical Dispersion Compensation for 111-Gb/s POLMUX-RZ-DQPSK," *Journ. Of Lightwave Technol*., Vol.27. No. 16, 2009.

[140] A. Stark, et al., "Scaling 112 Gb/s Optical Networks With the Nonlinear Threshold Metric," *Journ. Of Lightwave Technol*., Vol. 30. No. 9, 2012

[141] P. J. Winzer, et al., "Spectrally Efficient Long-Haul Optical Networking Using 112-Gb/s Polarization-Multiplexed 16-QAM," *Journ. Of Lightwave Technol.*, Vol. 28, No. 4, Feb 2010.

[142] A. H. Gnauck, et al., "Spectrally Efficient Long-Haul WDM Transmission Using 224-Gb/s Polarization-Multiplexed 16-QAM," *Journ. Of Lightwave Technol.*, Vol. 29, No. 4, Feb 2011.

[143] Y.-K. Huang, et al., "Transmission of Spectral Efficient Super-Channels using All-Optical OFDM and Digital Coherent Receiver Technologies," *Journ. Of Lightwave Technol.*, Vol. 29, No. 24, Dec 2011.

[144] T. Pfau, et al., "Optimization of Quadrature Amplitude Modulation Constellations for Phase Noise Impaired Channels," *Proc. of ECOC*, 2011.

[145] E. Ip and J. Kahn, "Feedforward Carrier Recovery for Coherent Optical Communications," *Journ. Lightwave Technol.*, Vol. 25, No.9, 2007.

[146] I. Fatadin, et al., "Blind Equalization and Carrier Phase Recovery in a 16-QAM Optical Coherent System," *Journ. Lightwave Technol.*, Vol. 27, No. 15, 2009.

[147] T. Pfau, et al., "Hardware-Efficient Coherent Digital Receiver Concept With Feedforward Carrier Recovery for *M*-QAM Constellations," *Journ. Lightwave Technol.*, Vol. 27, No. 8, 2009.

[148] Andrew Stark, et al., "DQPSK for metro networks", *Proc. SPIE* 7621, 76210L (2010).

[149] Andrew Stark, et al., "Dispersion map optimization of single and Dual-Pol QPSK in the presence of aggressor channels," *Photonics Society Summer Topical Meeting Series, 2010 IEEE* , vol., no., pp.40-41, 19-21 July 2010.

[150] Detwiler, T.F. et al., "Offset QPSK for 112 Gb/s coherent optical links," Photonics *Society Summer Topical Meeting Series, 2010 IEEE* , vol., no., pp.48-49, 19-21 July 2010.

[151] Detwiler, T.F, et al., "Offset QPSK receiver implementation in 112 Gb/s coherent optical networks," *Proc. Of ECOC 2010*, 19-23 Sept. 2010.

[152] Andrew Stark, et al., "Scaling 112 Gb/s PDM-QPSK hybrid optical networks," *Proc. Of OFC/NFOEC* 2011, NWA4.

[153] Yu-Ting Hsueh, et al., "Crosstalk-Induced OSNR Penalty Prediction on 112 Gb/s PolMux-QPSK System," *CLEO* 2011, CThH6.

[154] Yu-Ting Hsueh, et al., "Nonlinearity Impact on Crosstalk Effects for a 112 Gb/s PDM-QPSK System," *Proc. Of OFC* 2012.

[155] Yu-Ting Hsueh, et al., "Passband Narrowing and Crosstalk Impairments in ROADM-Enabled 100G DWDM Networks," *Journ. Of Lightwave Technol.,* Vol., No., 2012.

[156] Andrew Stark, et al., "Fiber Performance Comparison in all-EDFA 112 Gb/s PDM-QPSK Systems," *Proc. Of OFC* 2012, JW2A.50.

[157] Cheng Liu, et al., "Joint Digital Signal Processing for Superchannel Coherent Optical Systems: Joint CD Compensation for Joint ICI Cancellation," *Proc. Of ECOC* 2012, Th.1.A.4.

[158] Cheng Liu, et al., "Joint ICI Cancellation based on Adaptive Cross-Channel Linear Equalizer for Coherent Optical Superchannel Systems," *Proc. Of SPPCom* 2012, SpTu3A.2.

[159] Jie Pan, et al., "Inter-Channel Crosstalk Cancellation by MAP Detection for Nyquist-WDM Superchannel," *Proc. Of SPPCom* 2012, SpTu3A.3.

[160] Cheng Liu, et al., "Super receiver Design for Superchannel Coherent Optical Systems," Proc. Of SPIE, v 8284, p 828405 (8 pp.), 2012